A Vanessa

Contents

List of Figures

List of Tables

Introduction

A new era in the field of particle physics started on March 30th 2010, when proton beams at the Large Hadron Collider (LHC) at CERN were collided at collision energies of 7 TeV for the first time.

Building and operating such a unique and advanced machine is an impressive success and display of the technological progress itself. Furthermore, the collisions provide access to an unexplored energy regime and are studied at the two multi-purpose detectors ATLAS and CMS and the more specific experimental setups LHCb and ALICE. In the world of particle physics, higher energies correspond to smaller scales.

The hunt for the fundamental constituents of matter and their interactions is an ancient question, but answering this question only gained speed since the middle of the last century, when technological progress first allowed to actually look for these particles in high energy particle collisions. Currently, the Standard Model of Particle Physics (SM) serves as the most precise description of point-like particles - quarks and leptons - and their interactions through gauge bosons. But as successful as the Standard Model has been so far, as limited is it when reaching higher energies. The last missing piece of the Standard Model, the Higgs boson as manifestation of the mass generating mechanism, has probably been found in the last months.

Several theoretical ideas exist to either extend or replace the Standard Model and solve some or all of its problems, and new particles are expected to unveil the identity of such theories. However, no scent for new physics beyond the Standard Model has been found so far in the data taken and analyzed by the LHC experiments. In light of this, a deep and precise understanding of the SM is crucial to understand and calibrate the detector performance, and finally to spot any tiny deviation hinting at new phisics.

In this context, this analysis focus on the heaviest quark on the SM: the top quark. The top quark is also the last quark discovered, in 1995 at the Tevatron.

Precision measurements of the total and differential cross sections for the production of $t\bar{t}$ pairs will be presented, based on the large amount of data taken with the ATLAS detector in the year 2011.

The content of the thesis is as follows: in the first chapter we will describe the LHC and the ATLAS detector. In the second chapter we will focus on the properties of the top quark and in particular on the Standard Model predictions for the production of t tbar quark pairs in the final state. In the third and last chapter we will describe in detail our analysis and present the measurements of the total and single differential cross sections that will be compared to the theoretical predictions.

Chapter 1

LHC and ATLAS

1.1 The Large Hadron Collider

The Large Hadron Collider (LHC) [1] is a two-ring superconducting hadron synchrotron located at CERN, inside the 27 km tunnel that was constructed in 1989 for the Large Electron-Positron collider (LEP). The LHC is the largest and most complex scientific undertaking ever attempted. Its results will determine the future of the full discipline of high energy physics. This machine is designed to accelerate particles to the highest center-of-mass energy ever reached by humans tools: 14 TeV.

The high luminosity and increased cross sections at the LHC will allow precise tests of the strong and electroweak sectors of the Standard Model to be performed at the TeV scale. The discovery of the Higgs boson and the obsevation of signal of physics beyond the Standard Model are among the most important goals to be achieved with this machine.

1.1.1 Synchrotrons as particle accelerators

Ideated by Sir Marcus Oliphant, the synchrotron is a particular type of cyclic particle accelerator in which the magnetic field (used to bent the particles) and the electric field (used to accelerate the particles) are carefully synchronized with the travelling particle beam. The goal is to maintain particles in the same circular orbit, while the electric field gives energy at the particles turn after turn.

The accelerating electric field is given by a standing wave in a cavity resonator, with a frequency proportional to the revolution frequency of particles around the ring. For this reason, it must increase following the speed of particles, approaching a constant value when the speed saturate. The ratio between the electromagnetic frequency of cavity and revolution frequency of particles is named *harmonic number*, and it tell us how many locations in the ring (*buckets*) can be filled with particles to be accelerated.

To maintain each particle of the beam in the same orbit use is made of dipole magnets, that create an uniform magnetic field orthogonal to the particle trajectory, so that it can turn thanks to the Lorentz force, a force which depends on the particle velocity and the magnetic field where the particle is moving. When the particle is acquiring energy, thanks to the cavity resonator, its momentum will grow but its velocity will saturate approaching to c, the velocity of light. So, to achieve a stable orbit one must rise the dipole magnetic field strength during acceleration.

Modern synchrotrons, like the LHC, are composed by two coplanar rings: in one of them particles circulate clockwise, in the other anti-clockwise. The two rings intersect themselves in a number of points, and there the beams present in the ring will collide to generate the events that we can study.

Many other devices are essential for the correct operation of a synchrotron, like magnetic

quadrupoles, useful to focusing particles and limit the physical aperture of the vacuum chamber, or other magnetic devices (sextupoles, octupoles, etc.), useful to prevent beam instabilities. In particular, at the interaction points we must have the smallest transverse section of the beams and so additional devices are necessary.

Circulating beams, however, cannot stay in the rings for much time. Turn after turn, some of the particles contained in the beams are lost due to the interactions created for the experiments, some other will be lost because of the natural instability of circulating beams or by interactions with beam's measurement devices. Typically, the number of particles in the beams has an exponential fall with time, so the exponential parameter give us a reference time, called lifetime of the beam (37 hours in LHC). When a beam is too much poor in particles, it must be damped, and a new beam will be injected in the ring. Moreover, sometimes happens that one beam becomes too much unstable and it can potentially cause breakdowns in the accelerator devices, so it must be damped. This work is done by kicker magnets, which take out the beam and direct it to a special area where the particles are absorbed.

1.1.2 Acceleration system

The existing machines at CERN will be used to accelerate protons, in various steps, up to the nominal beam energy (Fig. 1.1): first the protons are obtained by ionizing hydrogen, then they are accelerated up to 50 MeV in the proton linac, which passes particles to the Proton Synchrotron Booster (PSB), where they reach 1.4 GeV. The Proton Synchrotron (PS) is the next stage, and it accelerate the protons up to 25 GeV. Finally, the SPS (Super Proton Synchrotron) is used to inject into the LHC 450 GeV protons. The maximum beam energy is limited by the peak dipole field (8.33 T).

The design luminosity of $10^{34} cm^{-2} s^{-1}$ is expected to be reached a few years after the first collisions.

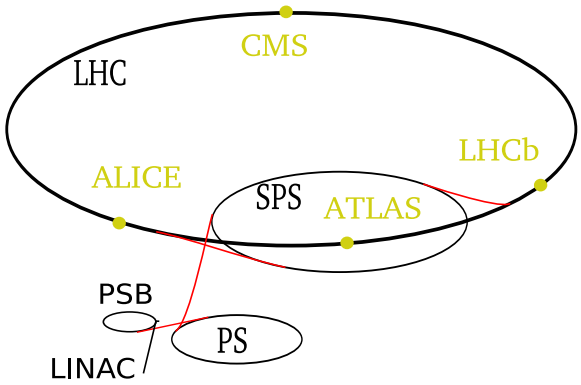

Figure 1.1: LHC The injection system of the LHC

Magnetic systems

The high beam intensity required for a luminosity of $L = 10^{34} cm^{-2} s^{-1}$ excludes the use of anti-protons, and hence excludes the particle-antiparticle collider configuration of a common vacuum and magnet system for both circulating beams, as used for example at the Tevatron. Separate magnetic fields are required. The LHC relies on superconducting magnets that are at the edge of present technology. Superconduction is a quantum-mechanical phenomenon who greatly reduces the resistivity of metals at low temperature (few Kelvin), so very high currents can circulate in the wires without generating heat due to the Joule effect. Another characteristic of superconducting

magnets with respect to traditional magnets is the absence of the iron to carry the magnetic flux: in superconducting magnets we have only the windings, and they are adjacent to the beam pipe. Particular attention has to be taken in considering the thermal contractions between the operational state (1.9 K) and the non-operative state, at room temperature (300 K).

Because of the need to keep costs down, almost all of the LHC superconducting magnets are housed in one "two-in-one" design, which accommodates the windings for the two beam channels in a common "cold mass" and cryostat, with magnetic flux circulating in the opposite sense through the two channels.

The main magnetic system is composed by 1232 dipoles (a section is shown in Fig. 1.2) that are 16.5 m longs devices curved to match the trajectory of particles, cooled at 1.9 K by superfluid Helium, with a circulating current up to 15000 A in their copper-clad Niobium-Titanium cables, useful to reach the targeted steering magnetic field up to 8.36 T.

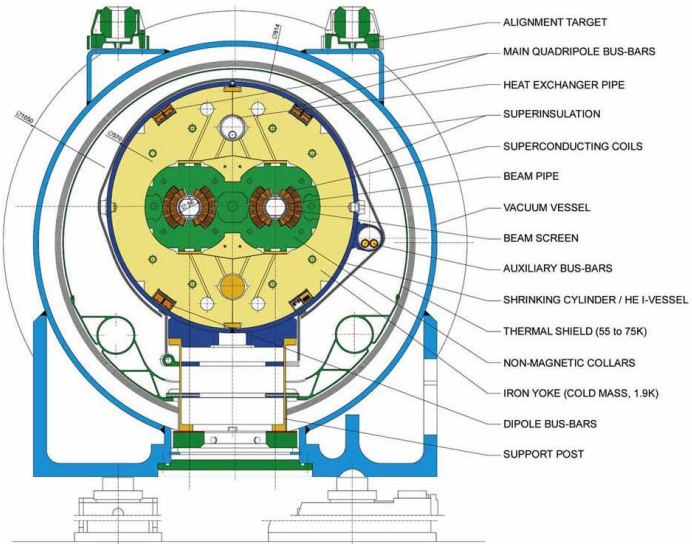

Figure 1.2: Section of a cryodipole system.

Other magnets assembled along the rings extension are needed for the correct working of the machine. Particle focusing is done by 400 superconducting quadrupoles operating at 1.9 K, and the peak of 6.85 T is generated with 11870 A current. Other 9 different types of quadrupoles are used for tuning, matching with SPS ring and in the interaction points. In addition there are other multipoles magnetic systems, to reach a number of 4000 magnets built and assembled along the 27 km long circumference of the LHC.

RF systems

Particles acceleration is provided by a 16 MV accelerating field, produced by two independent RF systems operating at 400 MHz, each composed by eight single-cell superconducting cavities cooled at 4.5 K and configured to give 2 MV of accelerating voltage. Because of similarity with RF-system of the LEP (operated at 352 MHz), cavities are built using the same technology of niobium sputtering on copper. In particular, niobium sputtered cavities are insensitive to the Earth's magnetic field and special magnetic shielding, as needed for solid niobium cavities, is not required.

Four cavities, each equipped with their helium tank, tuner, high-order modes (HOM) couplers and power coupler, are grouped together in a single cryomodule (Fig. 1.3). The concept of the cryomodule is itself modular: all cavities are identical and can be installed in any position, so if a problem arises with a cavity, it can "easily" be replaced.

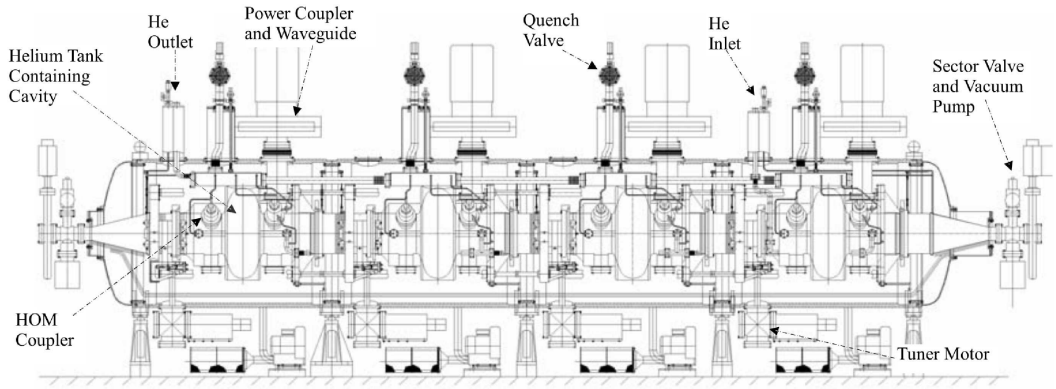

Figure 1.3: LHC main RF system: one of the two cryomodules.

Vacuum and cooling

Vacuum is essential for a particle accelerator to work: without vacuum, the entire beam will be lost in less than a round. Moreover, it's useful for the thermal insulation of the cryogenic apparatus. In the LHC we have tree differents vacuum systems: one for the beam pipe, the other for the cryomagnets and the last for the liquid helium distribution. Of course, the requirements for the beam pipe is much more stringent, driven by the required lifetime and background at the experiments. Quoting pressures as gas densities normalized to hydrogen, the requirements for a 100 hours beam lifetime is to $10^{15} H_2 m^{-3}$, which goes down to $10^{13} H_2 m^{-3}$ in the interaction regions.

Cooling for cryogenic systems is performed by eight refrigerators plants, four of which refurbished from LEP. Each one provide cooling to 1/8 of circumference along a compound cryogenic distribution line (QRL) running along the cryo-magnet strings in the tunnel. In view of the high thermodynamic cost of refrigeration at 1.8 K, the thermal design aims at intercepting the main heat influx at higher temperatures; hence the multiple-staged temperature levels in the system, all provided by different helium thermodynamic states (Fig. 1.4)

1.1.3 Performance goals

The design luminosity for the pp collisions in the two high-luminosity experiments (ATLAS and CMS) will be reached with 2835 bunches crossing at 25 ns intervals, i.e. ten RF periods, corresponding to a spatial separation of 7.5 cm.

The beam luminosity depends only on the beam parameters and can be written for a Gaussian beam distribution as:

$$l = \frac{N_b^2 n_b f_{rev} \gamma_r}{4\pi \epsilon_n \beta^*} F, \tag{1.1}$$

where N_b is the number of particles per bunch, n_b the number of bunches per beam, f_{rev} the revolution frequency, γ_r the relativistic gamma factor, ϵ_n the normalized transverse beam emittance, β^* the beta function[1] at the collision point, and F the geometric luminosity reduction factor due to the crossing angle at the interaction point.

The number of protons per bunch will be $N_b = 1.1 \cdot 10^{11}$ and does not mantain constant over a phisics run, because of losses due mainly to beam instabilities. So, the luminosity in the LHC decreases following the number of particles. Defining the time required to reach $1/e$ of initial luminosity as the lifetime of the beam, and considering all the major processes for particle loosing, one estimates a lifetime of 14.9 hours.

[1] a function which describe the oscillations of the particles in the phase-space

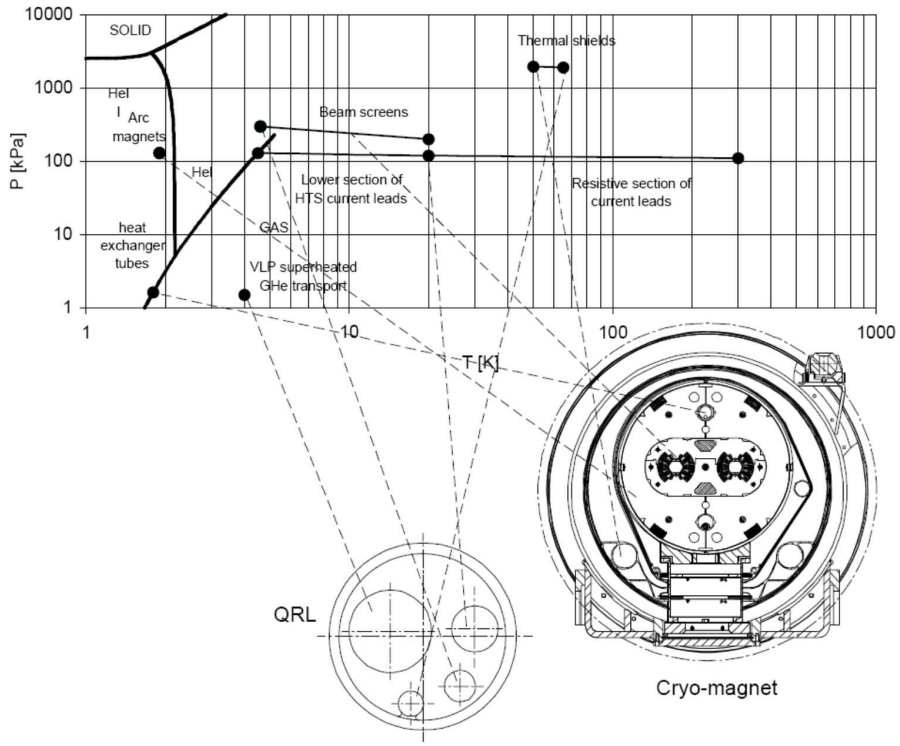

Figure 1.4: Thermodynamic states of helium in the cryogenic system.

At the LHC energies, the total inelastic non diffractive pp cross section is about 60 mb, and the number of inelastic scatterings per bunch crossing follows a Poisson distribution with an average of 19. This is called "pile-up" and because of this, thousands of particles will be produced in the observable region of space every 25 ns. Since the rate of interesting collisions with high transverse energy radiation is typically much lower than one in 19 (the cross section for $t\bar{t}$ pairs production production is 850 pb, the inclusive Higgs production is well below 1 nb for any Higgs mass), it is unlikely there will be more than one interesting event per bunch crossing. Nevertheless, extra activity recorded in one event can affect various aspects of detector measurements such as the calibration of the calorimeter.

The main parameters of the LHC for pp and heavy ion collisions are shown in Table 1.1). Along the perimeter of the LHC, five experiments have been built[1]: two general purpose experiments (ATLAS and CMS), one experiment dedicated to the study of heavy ion collisions (ALICE), and LHCb, dedicated to the study of B mesons decays. There is also another experiment, TOTEM, for the detection of protons from elastic scattering at small angles.

1.1.4 Performance

The LHC started operations in 2008, but a technical problem after ten days caused major damage to the machine. Only a year later, in November 2009, the first proton collisions were recorded, at the injection energy of 450 GeV. From then on, the beam energy has been ramped up gradually to 1.18 TeV, then 3.5 TeV in 2010 and 4 TeV in 2012. Since then, the LHC has been running steadily at these conditions, corresponding to a center of mass energy of 8 TeV, delivering over 20 fb-1 of data to the detectors. The total integrated luminosity in the year 2011 used in the present analysis amounts to almost 5 fb^{-1}. The total integrated luminosity per year of running is depicted in Fig. 1.5.

To reach this high luminosity we have only two ways: increasing the simultaneous interactions which can occour every bunch crossing, or filling more RF buckets.

LHC's engineers cover both ways: in Fig. 1.6 we can see how many primary vertex are

Parameters	p-p
Beam energy (TeV)	7.0
Center of mass energy (TeV)	14.0
Injection energy (GeV)	450
Bunch spacing (ns)	25
Particles per bunch	$1.1 \cdot 10^{11}$
R.M.S. bunch length (ns)	1.06
Numbers of bunches	2808
Initial luminosity ($cm^{-2}s^{-1}$)	10^{33}
Luminosity ($cm^{-2}s^{-1}$)	10^{34}
Luminosity lifetime (h)	10
Dipole Field (T)	8.3

Table 1.1: Main parameters of LHC

reconstructed by ATLAS detector, which means how many protons' interactions can occour every bunch crossing, while Fig. 1.7 shows how many bunches has been filled during the data taking runs.

1.2 The ATLAS Detector

The ATLAS (A Toroidal LHC ApparatuS) detector is an omni purpose detector, designed to explore the full physics program of the LHC, installed at Point 1 of LHC, 90 meters under ground at the base of the French Jura mountains.

ATLAS is composed of a large number of sub-detectors that will provide several type of measurements on the decay products of the interactions between the beams.

The assembly of sub-detectors is standard: moving radially outward the interaction region, we have a tracking system to measure the directions and momenta of all charged particles emerging from the interaction point; a calorimeter system to absorb and measure the energy of electrons, photons (EM calorimeter) and hadrons (hadronic calorimeter); an outer layer of muon detectors dedicated to the measurement of high-energy muons.

1.2.1 Overview

Fig. 1.9 gives an overall schematic view of the detector. The two independent magnetic systems (the solenoidal in the inner detector and the toroidal one in the muon spectrometer) are obtained with a thin superconducting solenoid surrounding the inner detector and with 8 independent coils arranged with an eightfold symmetry outside the calorimeters, respectively. The central solenoid envelopes the Inner Detector and provides a 2 Tesla field oriented along the beam axis. The inner detector makes use of three different technologies, at different distances from the interaction point. Three inner layers of pixels allow good secondary vertex identification and, together with the four layers of silicon micro-strips, good momentum measurements. The tracking is then completed by continuous strawtubes detectors with transition radiation detection capability in the outer part.

The calorimetry uses radiation hard liquid argon (LAr) technology for the EM barrel and EM endcap, for the Hadronic endcap (HEC) and for the Forward (FCAL) calorimeters. In the barrel region the cryostat is shared with the superconducting solenoid, while the EM endcap, the HEC and the FCAL share the same cryostat in the forward region. In the barrel region the longitudinal hermeticity is provided by the Tile calorimeter (TileCal). Scintillating tiles are used as active material, while the passive material is iron. The TileCal is subdivided in a barrel

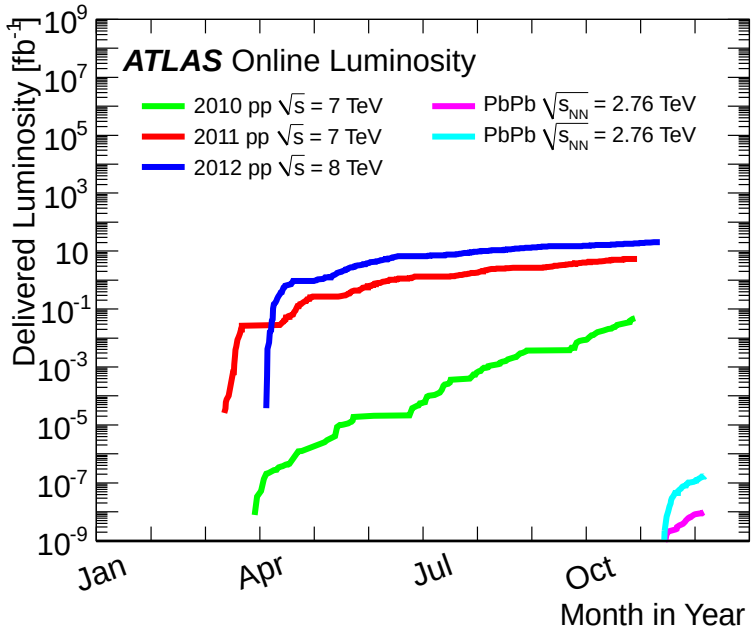

Figure 1.5: Cumulative luminosity versus day delivered to ATLAS during stable beams and for p-p and Pb-Pb collisions. This is shown for 2010 (green for p-p, magenta for Pb-Pb), 2011 (red for p-p, turquoise for Pb-Pb) and 2012 (blue) running. The online luminosity is shown.

($|\eta| < 1$) and an extended barrel ($1 < |\eta| < 1.7$) region. The gap between the two is covered by the Inter-TileCal and the Intermediate Gap Scintillators, which allow the recover part of the energy lost in the gap.

Outside the calorimeters there is the muon spectrometer. The magnetic field is provided by the 25 m long coils in the central region. The coverage at small angles is completed by two endcap toroids. The magnetic field bends the particles inside the open structure that constitutes the support for the muon chambers. The multiple scattering is therefore minimized. This allows a very good measurement of the muon momentum with three stations of high precision tracking chambers. The muon detector includes fast response trigger chambers, which operate in coincidence to provide a fast trigger decision on the muon P_T .

The total radius of the ATLAS experiment, from the interaction point to the last muon chamber, is about 11 m. The total longitudinal size is about 46 m, the overall weight is about 7 KTons. Almost 90% of the total ATLAS volume is occupied by the toroids and by the muon spectrometer.

The coordinate system of the detector is centered in the interaction point. The beam direction defines the z-axis and the x-y plane is the plane transverse to it. The positive x-axis is pointing towards the centre of the LHC ring and the positive y-axis towards the sky. Azimuthal angle ϕ is measured from the x-axis. The polar axis θ is measured from the positive z direction though pseudo-rapidity, η is generally used instead, where $\eta = -ln(tan(\frac{\theta}{2}))$.

1.2.2 The magnetic system

As already mentioned, two differents magnetic fields are present within the volume of the detector (Fig. 1.10): the central one, provided by the solenoid, and the outer one, produced by the toroids [2].

The central superconducting solenoid provides a central magnetic field of 2 T, while the peak value (at the superconductor face) is 2.6 T. In order to obtain the desired calorimetric performances, in particular for photon and electron energy measurements, a careful design to

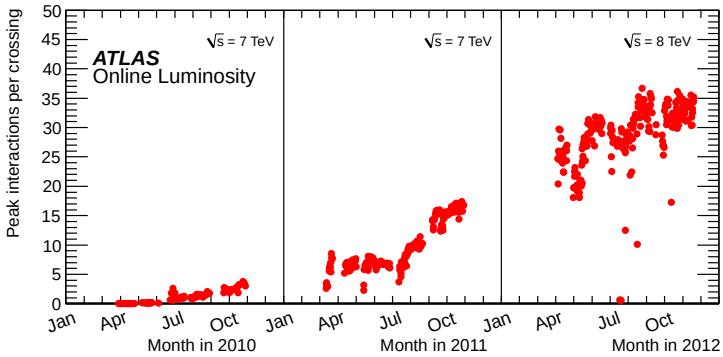

Figure 1.6: The maximum mean number of events per beam crossing versus day during the p-p runs of 2010, 2011 and 2012. This version shows the average value for all bunch crossings in a lumi-block. The online luminosity measurement is used for this calculation as for the luminosity plots. Only the maximum value during stable beam periods is shown.

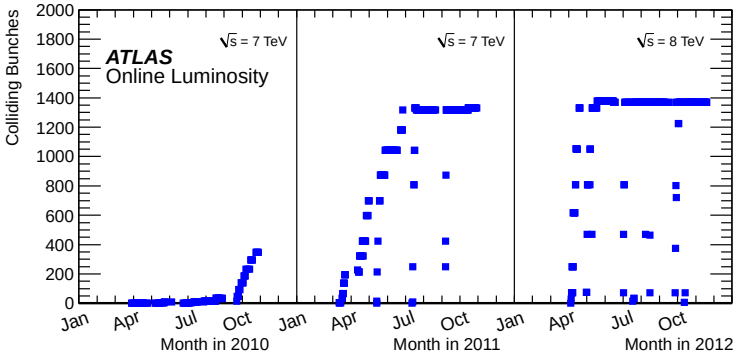

Figure 1.7: The number of colliding bunches in ATLAS versus time during the p-p runs of 2010, 2011 and 2012.

minimize the amount of dead material in front of the calorimeters has been done: the solenoid is placed inside the same vacuum vessel of the LAr calorimeter. The amount of dead material due to the solenoid and the cryostat wall is about one radiation length.

The magnetic field for the muon spectrometer in the barrel region is provided by a system of 8 coils assembled radially with an eight fold symmetry. The magnetic field in the forward region is obtained with the end-cap coils system, which is rotated by $22,5°$ with respect to the barrel coils to provide radial overlap and to optimize the bending power in the interface regions of the two coil systems. The peak magnetic field obtainable in the barrel region is about 4 T. The coils of the barrel are 25 m long and their height is 4.5 m. One cryostat is present for each coil. In the end-cap region there is only one cryostat within which the coils (5 m long and 4.5 m tall) are housed.

1.2.3 Inner detector

The strategy used for the ATLAS tracker [3] is to combine few high precision measurements close to the interaction point with a large number of lower precision measurements in the outer radius. Three different sub-detectors are designed to achieve this: a high resolution pixel detector, a microstrip semiconductor tracker (SCT), and a transition radiation tracker (TRT). The inner detector is embedded in the 2 T magnetic field provided by the central solenoid. The structure of the inner detector is shown in Fig. 1.11. Within a radius of 56 cm from the interaction point, pixel and silicon micro-strip technologies offer a fine-granularity, thus a high precision of the measurement. A track typically hits three layers of pixels (which measure both R - ϕ and z

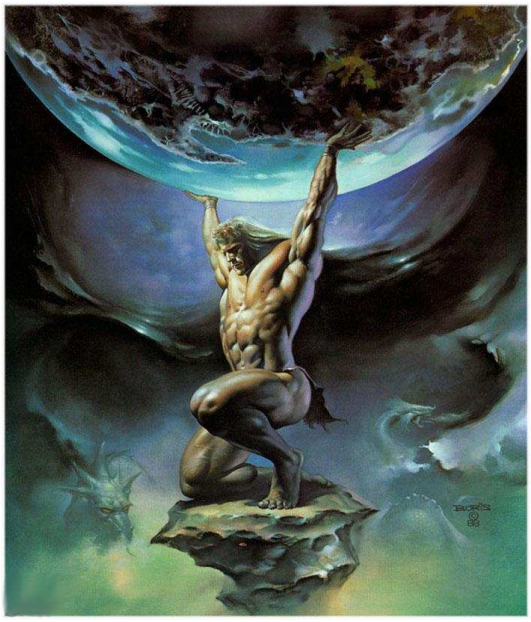

Figure 1.8: Boris Vallejo's Atlas

coordinate) and 8 layers of strips (SCT), for a total of 7 tracking points. Two SCT layers form one stereo strip (the angle between them is 40 mrad), allowing the measurement of the three coordinates. In the barrel region (which covers up to $\mid \eta \mid = 1$ for a total length of 160 cm), the pixels and SCT are arranged in concentric cylinders around the beam axis, while in the end-cap (up to $\mid \eta \mid = 2.5$) they are arranged in disks perpendicular to the beam axis.

A large number of tracking points (36) is provided by the TRT that also can give e/π separation identifying the transition radiation emitted by electrons travelling at high speed. It consists of straw tubes arranged parallel to the beam axis in the barrel region and in wheels around the beam axis in the end-cap. The reduced resolution with respect of the silicon detectors is compensated by the higher radius and by the number of points measured. Therefore, the relative precisions of the measurements of the TRT and pixels/SCT are comparable. The TRT detector is intrinsically radiation hard. The outer radius of the inner detector cavity is 115 cm, while the total length is 7 m. The layout provides full tracking coverage within $\mid \eta \mid < 2.5$, including impact parameter measurement and vertexing for heavy flavors and τ tagging. The expected precision for the detector is

$$\sigma_{R-\phi}(\mu m) = 13 \oplus \frac{62}{P_T\sqrt{sin\theta}}, \tag{1.2}$$

$$\sigma_z(\mu m) = 39 \oplus \frac{90}{P_T\sqrt{sin\theta}}. \tag{1.3}$$

While the radiation impact is low on the TRT detector, it is not in particular for the pixels, which are more exposed to the radiation since they are closer to the interaction point. The intrinsic radiation weakness of the silicon would probably impose their substitution after a few years of operation, depending on the luminosity profile.

1.2.4 Calorimeters

ATLAS calorimetric systems differ in technology and materials depending on the pseudorapidity region (Fig. 1.12). We can count three types of calorimeters: An electromagnetic (EM) calorime-

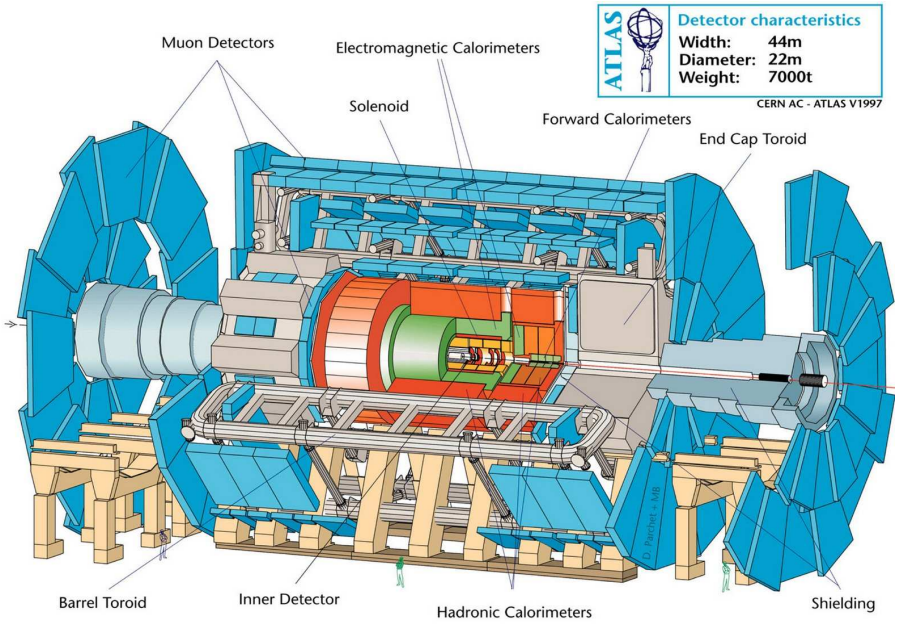

Figure 1.9: The Atlas detector

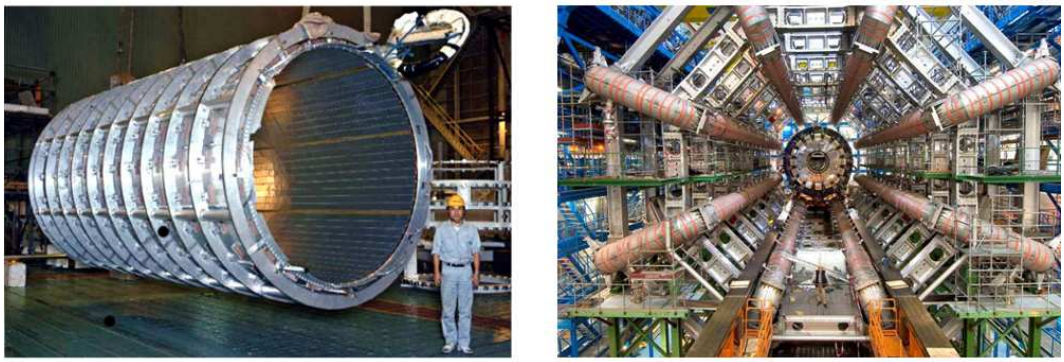

Figure 1.10: The magnetic system: (left) central solenoid and (right) outer toroids

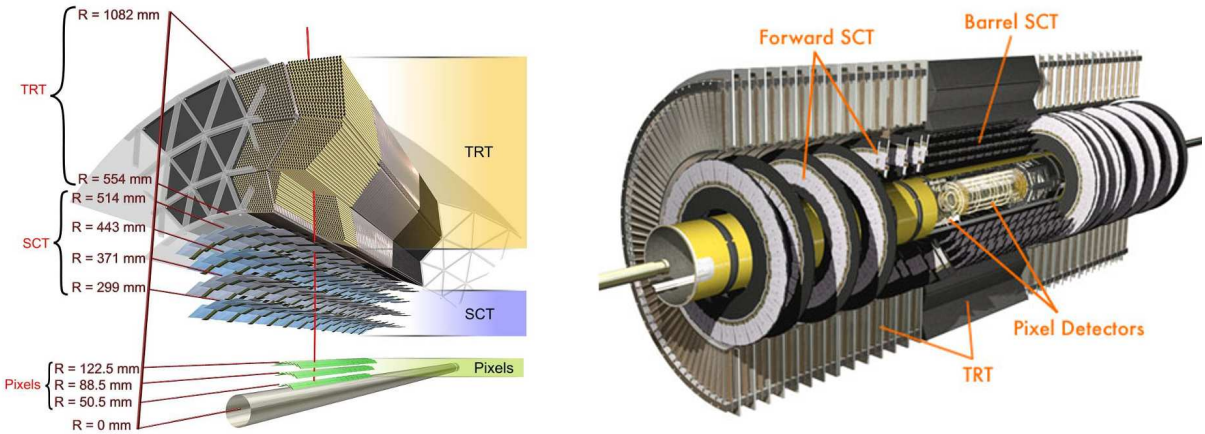

Figure 1.11: The inner detector

ter covering the region $|\eta| < 3.2$, hadronic calorimeters in the barrel ($|\eta| < 1.7$), and in the endcaps ($1.3 < |\eta| < 3.2$), and forward calorimeters covering the region $3.1 < |\eta| < 4.9$.

The electromagnetic calorimeter consists of liquid Argon (LAr) as active material with an accordion-like structure of Kapton electrodes and lead as absorber. The calorimeter is divided into several samples of $\Delta\eta \times \Delta\phi$ size varying from 0.003 x 0.1 to 0.1 x 0.1, depending on the pseudorapidity range. The EM has about 190 000 readout channels and is $24X_0$ thick. On the inner side of the EM, a presampler, consisting of a LAr layer of 1.1 cm(0.5 cm) thickness in the barrel (endcaps), is installed. The design goal for the EM energy resolution is

$$\frac{\sigma(E)}{E} = \frac{0.1}{\sqrt{E}} \oplus \frac{0.3}{E} \oplus 0.01 \tag{1.4}$$

Three structures constitues the hadronic calorimeter: the tile calorimeter, the liquid-argon end-cap calorimeter (HEC) and the liquid-argon forward calorimeter (FCal).

The tile calorimeter, located in the region $| \; eta \; | < 1.7$, use steel as absorber and scintillator as the active medium. It is subdivided into a central barrel ($| \; \eta \; | < 1.0$) and two extended barrels ($0.8 < | \; \eta \; | < 1.7$).

The HEC is a copper-liquid argon calorimeter which cover the range $1.5 < | \; \eta \; | < 3.2$. The very forward region ($3.1 < | \; \eta \; | < 4.9$) is covered by the FCal, which use copper or tungsten as passive material.

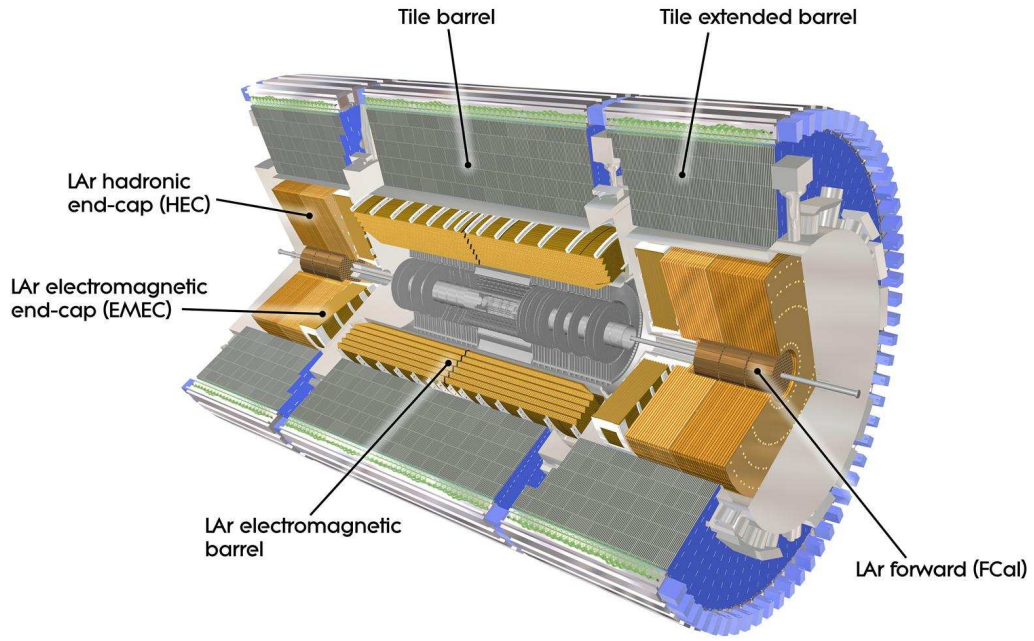

Figure 1.12: Atlas's calorimeters

The energy resolution is

$$\frac{\sigma(E)}{E} = \frac{0.5}{\sqrt{E}} \oplus 0.03. \tag{1.5}$$

1.2.5 Muon Spectrometer

One of the most important features of the muon spectrometer [4] is the possibility of a precise standalone measurement of the muon momentum. The magnetic field provided by the superconducting air-core toroid magnets deflects the muon trajectories that are measured by high precision tracking chambers. The magnetic field in the $| \; \eta \; | < 1.0$ range is provided by the barrel toroids, while the region $1.4 < | \; \eta \; | < 2.7$ is covered by the end-cap. In the so called transition

region ($1.0 <| \eta |< 1.4$) the combined contributions of both the barrel and end-cap provide the magnetic field coverage. The magnetic field is mostly orthogonal to the muon trajectory in the covered pseudorapidity range, while the effect of multiple scattering is minimized. In the barrel region, the muon chambers are arranged in three cylindrical layers (stations), while in the end-cap they form three vertical walls. The transition region is instrumented with one extra station.

The azimuthal layout follows the magnet structure: there are 16 sectors. The so called Large sectors lie between the coils, and they overlap with the Small sectors, placed in correspondence with the coils themselves.

The choice of the different chambers technology has been driven by the particle fluxes foreseen in the different regions of the detector. Criteria of rate capability, granularity, aging properties and radiation hardness have been considered. Table 1.2 summarizes the chamber technologies used in the various pseudorapidity regions.

The measurement of the muon's trajectory is provided (in most of the η region) by the Monitored Drift Tubes (MDT), while at large pseudorapidity, the higher granularity Cathode Strip Chambers (CSC) are used.

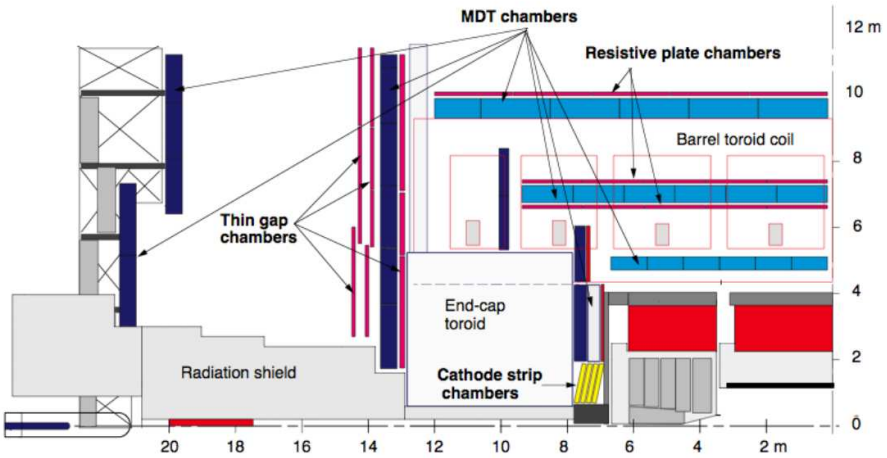

Figure 1.13: Side view of the placement of muon chambers.

The MDTs consist of 3 cm-diameter aluminium tubes, filled with a 93% : 7% mixture of Argon and CO_2, and a 50 μm sense wire in the centre. The MDTs cover most of the η range. The CSCs are multiwire proportional chambers of high granularity, filled with a 30% : 50% : 20% gas mixture of Argon, CO_2, and CF_4. The CSCs cover the region $2 <| \eta |< 2.7$ (see Fig. 1.13).

The requirements on the momentum resolution ($\frac{\Delta P_T}{P_T} \simeq 10\%$ at 1 TeV/c) call for an accuracy of the relative positioning of chambers traversed by a muon track that matches the intrinsic resolution and the mechanical tolerances of the precision chambers. The knowledge of the chamber positioning with an accuracy of 30 μm is required within a projective tower. The accuracy required for the relative positioning of different towers to obtain adequate mass resolutions for multimuon final states is in the millimeter range. This accuracy can be achieved by the initial positioning and survey of chambers at the installation time. The relative alignment of muon spectrometer, calorimeters and ID will rely on the measurement of the high-momentum muon trajectories. The MDT chambers are equipped with a in-plane alignment system aiming at a measurement of the tube position displacements, with respect to their nominal positions at the assembly phase, with a precision better than 10 μm. To achieve this the spectrometer is equipped with a RASNIK system: a laser, mounted at one side of a chamber, projects a pattern to a CCD camera positioned at the other end of the camera. From the displacement of the pattern-figure respect to what is expected, corrections for chambers deformation can be computed.

The chambers for the LVL1 muon trigger system covers the region $|\eta| < 2.4$. Resistive Plate Chambers (RPC) are used in the barrel region, while the Thin Gap Chambers (TGC) are used in the end-cap. Their first task is to identify without any ambiguity the bunch crossing of the triggered event. This requires a high time resolution, designed to be 2 ns for RPCs and 5 ns for TGCs. Next, they have to provide a well defined p_T cutoff for the LVL1 choice. This is obtained considering a window of a size defined by the LVL1 p_T threshold considered on the second RPC (or TGC) station once a super-hit has been obtained in the first station. Finally, the trigger chambers measure the non-bending coordinate (ϕ), in a plane orthogonal to that measured by the precision chambers, with a typical precision of 5-10 mm.

Region		station I	station E	station M	station O
Barrel	$\|\eta\| < 1$	MDT		MDT RPC	MDT RPC
End-Caps	$1 < \|\eta\| < 1.4$	MDT TGC	MDT		
	$1.4 < \|\eta\| < 2$	MDT TGC		MDT TGC	
	$2 < \|\eta\| < 2.4$	CSC			MDT
	$2.4 < \|\eta\| < 2.7$	CSC		MDT TGC	

	TRIGGER	CHAMBERS	PRECISION	CHAMBERS
Technologies used	RPC	TGC	MDT	CSC
Number of channels	354K	440K	372K	67K
Area (m^2)	3650	2900	5500	27
Time resolution	$< 5ns$	$< 7ns$	$500ns$	$< 7ns$
Spatial resolution	5-10 mm		$80\mu m$	$60\mu m$

Table 1.2: Design parameters of the muon spectrometer

1.2.6 Trigger, Data acquisition and Control systems

The ATLAS trigger and data acquisition systems (TDAQ) and the detector control system (DCS) are responsible for the data-flow from the detectors' front-end electronics modules to data storage at the CERN computing center, for the selection of events and for the control and monitoring of the apparatus [5]. A schematic diagram is presented in Fig. 1.14 and can be broken into four principal systems, namely:

1. The Data Flow System - responsible for receiving the detector data, serving data to the trigger system, and transporting the data for selected events to mass storage;

2. The Trigger System - subdivided into three layers. A first purely hardware level (LVL1) and two software levels (collectively called High Level Trigger, HLT);

3. The Online System - responsible for all aspects of experiment and TDAQ operation and control during data-taking, and during testing and calibration runs;

4. The DCS - responsible for the coherent and safe operation of the ATLAS detector, as well as the interface with external systems and services including the LHC itself.

The Online system is implicitly understood to be connected to all elements in Fig. 1.14, and the DCS to all hardware elements which need to be monitored and controlled.

In the right-half of figure Fig. 1.14 the data flow system is represented in the different components. The signals coming from the detectors (upper part), read by the input-output systems are managed by the back-end electronics boards: the so called Read Out Drivers (ROD). They are detector-specific and they have the responsibility of the reading of the data from the front-end

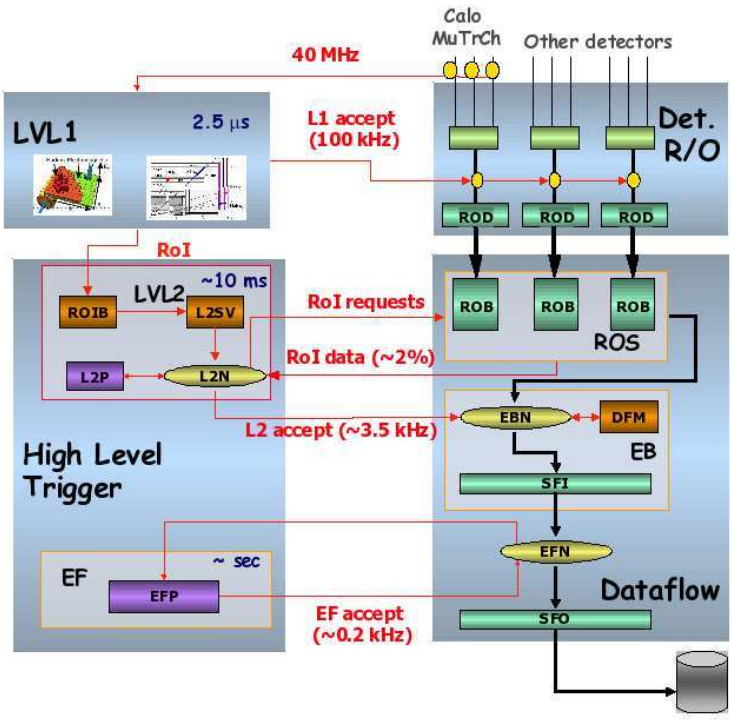

Figure 1.14: Trigger and Data flow

electronics when a Level 1 trigger request is propagated to the system. The RODs, equipped with DSPs, have also the responsibility to make the first pre-formatting of the data to the ATLAS TDAQ final format and, in some cases, like for the calorimeters, apply some simple algorithms and performing calculations. From this point on, the components of the Data Flow are no more detector specific.

The data are then moved to the ROSes (Read Out System), normal PCs equipped with one or more buffer cards, the Read Out Buffers (ROBs). Here they will be further formatted and moved, after request, to the Event Building Network (EBN), passed to the last stage of trigger, and in case of acceptance, stored to a set of local disk pools (SFO: Sub Farm Output). The numbers of the TDAQ system are reported in Table 1.3 where the numbers of RODs, ROSes and CPUs are reported for the different subsystems.

Detector	RODs	ROSes
Pixel	120	11
SCT	92	8
TRT	192	20
LAr (EM barrel + EMEC + HEC + FCAL)	192	33
TileCal	32	8
Muon System (MDT + CSC + RPC + TGC)	296	26
LVL1	24	5

	PCs
LVL2 Processors	∼ 500
EF Processors	∼ 1600
DataFlow and Control Machines	∼ 300

Table 1.3: Size of different detectors TDAQ components: number or RODs and ROSes and, for the HLT and for the DataFlow system, the number of needed PCs.

Starting from an initial bunch-crossing rate of 40 MHz, the rate of selected events must be reduced to about 100 Hz for permanent storage. The event rate is determined by the total pp cross section, and is about 10^9 evt/sec at the nominal luminosity. Hence an overall rejection factor of 10^7 against minimum bias events is required. This strong requirement must match the need of an excellent efficiency for the rare physics processes of interest. Therefore the principal requirement of the Level 1 (LVL1) trigger is that it identifies unambiguously the interesting physics events, while strongly reducing the overall rate. The LVL1 trigger makes an initial selection based on a reduced granularity information from a subset of detectors. Objects searched by the calorimeter trigger are high p_T electrons and photons, jets, and τs decaying into hadrons, as well as large missing and total transverse energies. High and low transverse momentum muons are identified using only the muon trigger chambers. The calorimeter selections are based on a reduced-granularity information from all the calorimeters. In the case of the electron/photon and hadron/τ triggers, energy isolation cuts can be applied. The missing and total scalar transverse energies used in the LVL1 trigger are calculated by summing over trigger towers. In addition, a trigger on the scalar sum of jet transverse energies is also available. No tracking information is used at LVL1 due to timing restrictions and the inherent complex nature of the information from the inner detector. The LVL1 trigger decision is based on a logical combinations of these objects. Most of the physics requirements of ATLAS can be met by using, at the LVL1 trigger level, fairly simple selection criteria of a rather inclusive nature. However, the trigger implementation is flexible and it can be programmed to select events using more complicated signatures. The maximum rate at which the ATLAS front-end systems can accept LVL1 triggers is limited to 75 kHz (upgradeable to 100 kHz). The target rates estimated in trigger performance studies, using trigger menus that meet the needs of the ATLAS physics program, are about a factor of two below this limit.

An essential requirement on the LVL1 trigger is that it should uniquely identify the bunch-crossing of interest. Given the short (25 ns) bunch-crossing interval, this is a non-trivial task. In the case of the muon trigger, the physical size of the muon spectrometer implies times-of-flight comparable to the bunch-crossing period. For the calorimeter trigger, a serious challenge is that the pulse shape of the calorimeter signals extends over many bunch crossings.

During this time, information for all detector channels are stored in pipeline memories. The LVL1 latency, measured from the time of the pp collision until the trigger decision is available to the front-end electronics, is required to be less than 2.5 μs. In order to achieve this, the LVL1 trigger is implemented as a system of purpose-built hardware processors.

Another important functionality of the LVL1 system is the identification of the Regions Of Interest (ROIs) representing the position of the triggering objects in the (η, ϕ) space. This is one of the main peculiarities of ATLAS triggering system. This information is used to greatly reduce the needed computation time at the LVL2 triggering system and the size of data to be transferred in the system.

The LVL2 runs offline-like algorithms, optimized for the on-line use, using the full granularity information from the inner detector as well as from the muon detectors and calorimetry. However it is structured to process the data belonging only to a spatial window around the ROIs identified by the LVL1 trigger. Simulations showed that this corresponds to roughly 2-5% of the overall ATLAS data size. LVL2 has a maximum latency time of 10 ms, after this time the event is selected (and hence moved to the Event Filter system for further processing) or discarded and removed from the Data Flow chain (up to this moment the event fragments have been buffered in the ROBs. The final LVL2 rate is expected to be about 1-2 KHz.

After LVL2, the last stage of the on-line selection is performed by the Event Filter. It will employ offline algorithms and methods, slightly adapted to the on-line environment, and use the most up to date available calibration and alignment information and the magnetic field map. Complete event reconstruction is performed by the Event Filter, which will make the final

selection of physics events to be written to mass storage for subsequent offline analysis. The time available for a decision at the event filter is 1 s. The output rate from LVL2 should be reduced by an order of magnitude, giving about 100 Hz. The final event size is expected to be 1 MBytes corresponding to an output data rate of about 100 MByte/s resulting in 10^{15} bytes of data per year.

1.2.7 Computing

The complexity and size of the ATLAS experiment imposes the use of new paradigms also in what the processing of the data is concerned once they are made available on mass storage. The events rate of 100 Hz, the size of the events (approximately 1 MB per event), the number of physicists involved in the analysis requires that the data distribution, processing and analysis is carried out according to a multi-tier schema, that is well suited to distribute the computing and storage loads among the different participating institutes. Even if similar strategies have been used in the past it is the first time that this kind of distributed analysis are performed on a ATLAS-size scale requiring the development of completely new tools extremely performing [6].

At the output of the event filter the raw data are transferred to the CERN's computing center, known as Tier-0, that is the first layer of the ATLAS analysis system. Here a complete copy of the raw data is stored and a first-pass reconstruction is applied producing ESD (Event Summary Data) and AOD (Analysis Object Data). The ESD data-format contains the reconstructed quantities measured by the detector (energy in the calorimetric cells, clusters information, tracks) as well as the reconstructed physics objects (electrons and gammas, jets, taus, muons). The small-sized data in AOD format are well suited for distribution to the physics groups, to reduce their size only the physics objects are recorded. Each event can be characterized by few quantities, like, for example, the number of jets in the event, P_T of the leading jet, lepton multiplicity and so on, this information is produced by Tier-0 and stored in the TAGs and allows for a very fast filtering of the datasets. Tier-0 has also the responsibility to run calibration and alignment algorithms that will be refined in future steps. Distribution of data to the community is done copying raw data, ESDs, AODs and TAGs to the Tier-1s. Tier-1s are big regional computer centers spread around the world (at the moment ATLAS foresees 10 of this centers). A copy of the raw data is divided among all the Tier-1s (each one having on average 10% of the entire raw data) while a complete copy of the ESDs, AODs and TAGs is distributed to each Tier-1. Tier-1s have also the responsibility to reprocess raw data performing more accurate reconstructions, updated version of ESDs, AODs and TAGs are therefore constantly produced and spread among the different computer centers.

Most of the physics analysis is performed at the Tier-2s center, an average of 5 Tier-2s are directly connected to one Tier-1 and typically receive a copy of one third of the most updated ESD and AOD data and a complete copy of the TAGs, they have the entire responsibility for the official Monte Carlo production (the simulated data are stored in the more reliable Tier-1s), the physics groups analysis and the development and refinement of calibration and reconstruction algorithms are also performed at the Tier-2 centers. The physics analysis will be performed mainly on the AOD data set (with the help of TAGs for pre-selections) or on even more compact derived formats like ntuples.

The multi-tier paradigm is deployed using grid technology and middle-ware that completely hides to the physicists the complex multi-tier structure [7].

1.2.8 Atlas performances

All the systems work properly in ATLAS. In Table 1.4 we can see the overall efficiency for the year 2011 of the various subdetectors, while in Fig. 1.15 is shown the integrated luminosity recorded by ATLAS and the data taking efficiency during the 2011. In this last plot by efficiency we mean

the ratio between the luminosity given by the LHC starting when the "stable beams" has been declared until the LHC requests ATLAS to turn the sensitive detector off to allow a beam dump or beam studies, and the luminosity recorded by ATLAS. The empty bins are due to days in which no stable beams were delivered by the LHC. The inefficiency accounts for the turn-on of the high voltage of the Pixel, SCT and some of the muon detectors and any inefficiencies due to deadtime or due to individual problems with a given subdetector that prevent the ATLAS data taking to proceed.

Subdetector	number of channels	efficiency
Pixels	80 M	95.0%
SCT Silicon Strips	6.3 M	99.3%
TRT Transition Radiation Tracker	350 k	97.5%
LAr EM Calorimeter	170 k	99.9%
Tile calorimeter	9800	98.3%
Hadronic endcap LAr calorimeter	5600	99.6%
Forward LAr calorimeter	3500	99.8%
MDT Muon Drift Tubes	350 k	99.7%
CSC Cathode Strip Chambers	31 k	96.0%
RPC Barrel Muon Chambers	370 k	97.1%
TGC Endcap Muon Chambers	320 k	98.2%

Table 1.4: Efficiency of the ATLAS subsystems in 2011.

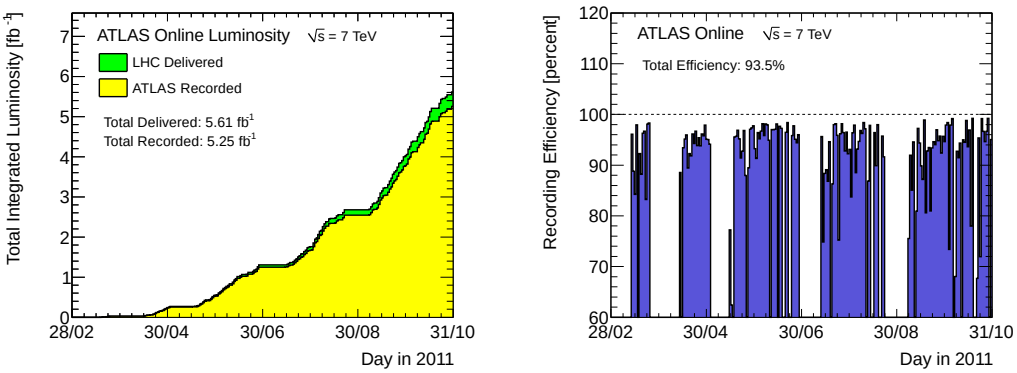

Figure 1.15: Left: Cumulative luminosity versus day delivered to (green), and recorded by ATLAS (yellow) during stable beams and for pp collisions at 7 TeV centre-of-mass energy in 2011; right: recorded efficiency for each day of data taking in 2011.

Chapter 2

Top production in p-p interactions at the LHC

2.1 The Standard Model

Our present understanding of the fundamental constituents of matter, quarks and leptons, and their interactions is provided by the Standard Model (SM), a theory developed in the 1960's and 70's that has been experimentally succesfully tested in the last 40 years.

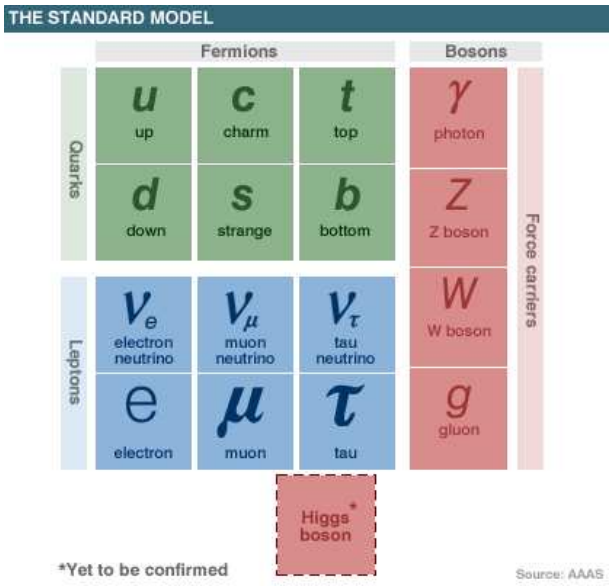

Figure 2.1: Fundamental Particles

The SM is a quantum field theory based on the gauge group $SU(3)_C \times SU(2)_L \times U(1)_Y$, that includes two groups of fundamental particles (see Fig. 2.1): the fermions (six quarks and six leptons and their anti-particles), and twelve gauge bosons which are the interaction carriers. Tree type of basic interactions are embedded:

- **electromagnetic**, which acts between electrically charged particles. The theory of electromagnetic interactions (Quantum Electro-Dynamics) is based on the $U(1)$ symmetry group, and the carrier of this force is the photon (γ);
- **weak**, acting between particle carrying weak charge. The theory describing this interaction is based on the $SU(2)$ group of symmetry, and the carriers are three vector bosons, the electrically charged W^+, W^- and the neutral Z^0;

- **strong**, which acts between particle carrying "colour" charge. This interaction, described by Quantum Cromo-Dynamics (QCD)[10] is based on the $SU(3)$ symmetry group and the carriers are 8 bosons called gluons. Because they carry colour charge too, they interact among themselves.

The problem to incorporate gravity in the theory is still open.

There are three generations of quarks and leptons, labelled by the index i = 1, 2, 3, which have some different characteristics, but the gauge interactions do not distinguish between them, acting with the same strenght indipendently of the generation.

				$SU(3)_C$	$SU(2)_L$	$U(1)_Y$	T	T_3	Q
$Q_L^i =$	$\binom{u_L}{d_L}$	$\binom{c_L}{s_L}$	$\binom{t_L}{b_L}$	3	2	1/6	1/2	$+1/2$ $-1/2$	$+2/3$ $-1/3$
$u_R^i =$	u_R	c_R	t_R	3	1	2/3	0	0	$+2/3$
$d_R^i =$	d_R	s_R	b_R	3	1	-1/3	0	0	-1/3
$L_L^i =$	$\binom{\nu_{eL}}{e_L}$	$\binom{\nu_{\mu L}}{\mu_L}$	$\binom{\nu_{\tau L}}{\tau_L}$	1	2	-1/2	1/2	$+1/2$ $-1/2$	0 -1
$e_R^i =$	e_R	μ_R	τ_R	1	1	-1	0	0	-1
$\nu_R^i =$	ν_{eR}	$\nu_{\mu R}$	$\nu_{\tau R}$	0	0	0	0	0	0
$\phi =$	$\binom{\phi^+}{\phi^0}$			1	2	1/2	1/2	$+1/2$ $-1/2$	$+1$ 0

Table 2.1: The fields of standard model and their gauge quantum numbers

Once the gauge symmetries and the fields with their (gauge) quantum numbers are specified (Table 2.1), the Lagrangian of the Standard Model is fixed by requiring it to be gauge-invariant, local, and renormalisable. The Standard Model Lagrangian can be divided into several pieces:

$$\mathcal{L}_{SM} = \mathcal{L}_{Gauge} + \mathcal{L}_{Matter} + \mathcal{L}_{Yukawa} + \mathcal{L}_{Higgs}. \tag{2.1}$$

The first piece is the pure Lagrangian, given by

$$\mathcal{L}_{Gauge} = \frac{1}{2g_S^2} Tr G^{\mu\nu} G_{\mu\nu} + \frac{1}{2g^2} Tr W^{\mu\nu} W_{\mu\nu} + \frac{1}{2g'^2} Tr B^{\mu\nu} B_{\mu\nu} \tag{2.2}$$

where where $G^{\mu\nu}$, $W^{\mu\nu}$ and $B^{\mu\nu}$ are the gluon, weak, and hypercharge field-strength tensors. These terms contain the kinetic energy of the gauge fields and their self interactions. The next piece is the matter Lagrangian, given by

$$\mathcal{L}_{Matter} = i\bar{Q}_L^i \not{D} Q_L^i + i\bar{u}_R^i \not{D} u_R^i + i\bar{d}_R^i \not{D} d_R^i + i\bar{L}_L^i \not{D} L_L^i + i\bar{e}_R^i \not{D} e_R^i \tag{2.3}$$

This piece contains the kinetic energy of the fermions and their interactions with the gauge fields, which are contained in the covariant derivatives. For example,

$$\not{D} Q_L = \gamma^\mu \left(\partial_\mu + i g_S G_\mu + i g W_\mu + i \frac{1}{6} g' B_\mu \right) Q_L, \tag{2.4}$$

since the field Q_L participates in all three gauge interactions. A sum on the index i, which represents the generations, is implied in the Lagrangian.

These two pieces of the Lagrangian depend only on the gauge couplings g_S, g, g'. Their approximate values, evaluated at the scale M_Z, are

$$\begin{aligned} g_s &\approx 1, \\ g &\approx 2/3, \\ g' &\approx 2/(3\sqrt{3}). \end{aligned} \tag{2.5}$$

Mass terms for the gauge bosons and the fermions are forbidden by the gauge symmetries. The mechanism which gives mass to the particles is described in the other two pieces of the SM lagrangian. One is the Higgs lagrangian[11]:

$$\mathcal{L}_{Higgs} = (D^{\mu}\phi)^{\dagger} D_{\mu}\phi + \mu^2\phi^{\dagger}\phi - \lambda(\phi^{\dagger}\phi)^2, \tag{2.6}$$

with the Higgs doublet ϕ as given in Table 2.1. This piece contains the kinetic energy of the Higgs field, its gauge interactions, and the Higgs potential, shown in Fig. 2.2. The coefficient of the quadratic term, μ^2, is the only dimensionful parameter in the Standard Model. The sign of this term is chosen such that the Higgs field has a non-zero vacuum expectation value v on the circle of minima in Higgs-field space given by $\langle\phi^0\rangle = \mu/\sqrt{2\lambda} \equiv v/\sqrt{2}$. Because no direction is preferred in that circle of minima, an infinite number of fundamental states can be taked. So, we can choose in an arbitrary way the "vacuum" state as

$$\langle\phi\rangle = \begin{pmatrix} 0 \\ v \end{pmatrix}, \tag{2.7}$$

and develop the Higgs field around this value. Then the gauge fields has to be rewritten taking

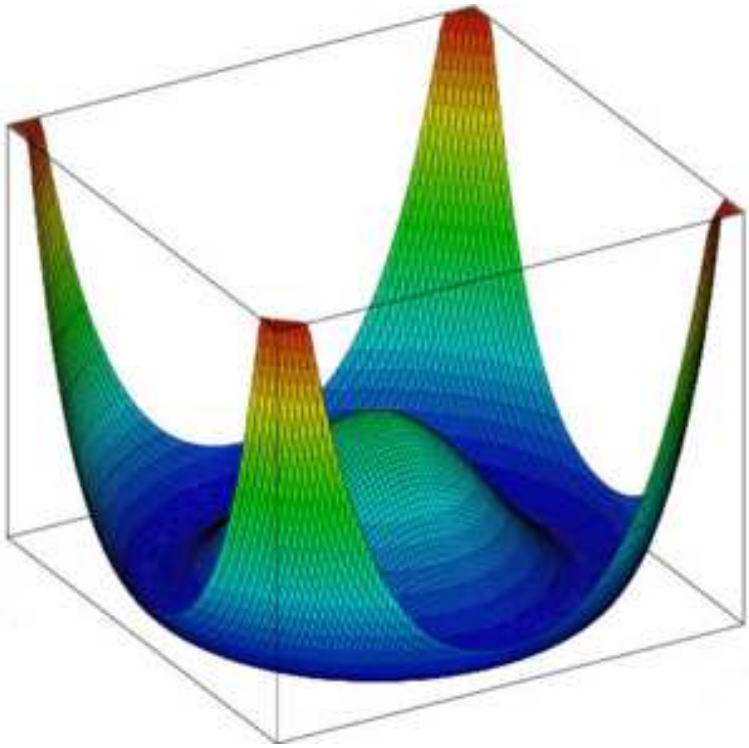

Figure 2.2: The Higgs potential

into account this change of variables, and this lead the vector bosons W^1_{μ}, W^2_{μ} to have a non vanishing mass:

$$M_W = \frac{1}{2}gv \tag{2.8}$$

whereas the mass terms for the W^3_{μ} and B_{μ} fields, is not diagonal:

$$M^2 = \frac{v^2}{4}\begin{pmatrix} g^2 & -gg' \\ -gg' & g'^2 \end{pmatrix}. \tag{2.9}$$

Defining the "Weinberg angle" as $tan(\theta_W) = g'/g$, we can diagonalize the matrix using the orthogonal combinations

$$Z_{\mu} = cos\theta_W W^3_{\mu} - sin\theta_W B_{\mu} \quad , \quad A_{\mu} = sin\theta_W W^3_{\mu} + cos\theta_W B_{\mu}. \tag{2.10}$$

These two new fields carry the characteristics of the EM field (A_μ) and the neutral weak field (Z_μ). This is the core of the Glashow-Salam-Weinberg (GSW) theory of ElectroWeak interactions [12]. The field A^μ is massless, while the field Z_μ acquire the mass

$$M_Z = \frac{1}{2}\sqrt{g^2 + g'^2}v \tag{2.11}$$

Fermions are supposed to experience a further kind of interaction, the Yukawa interaction. The most noticeable characteristic is that, while in the gauge interaction two fermions couple with a gauge boson, in Yukawa interactions two fermions couple to the Higgs field, which is a scalar field,

$$\mathcal{L}_{Yukawa} = -\Gamma_u^{ij}\bar{Q}_L^i\epsilon\phi^* u_R^j - \Gamma_d^{ij}\bar{Q}_L^i\phi d_R^j - \Gamma_e^{ij}\bar{L}_L^i\phi e_R^j + h.c., \tag{2.12}$$

where $\epsilon = i\sigma_2$ is the total antisymmetric tensor in 2 dimensions, related to the second Pauli matrix and required to ensure each term separately to be electrically neutral, and the coefficients Γ_u, Γ_d, Γ_e are 3 x 3 complex matrices in the generation space. Since the Yukawa couplings may involve quarks of different generations, the eigenstates of the EW interaction do not have well-defined masses. Taking into account the spontaneous symmetry breaking, as discussed above, we can express the Yukawa matrices as mass matrices,

$$M_f = \Gamma_t\frac{v}{\sqrt{2}}, \tag{2.13}$$

and we can always find unitary matrices V_{fL} and V_{fR} such that

$$V_{fL}M_f V_{fr}^\dagger = M_f^{diag} \tag{2.14}$$

is a diagonal real matrix. The quark mass eigenstates are then identified as:

$$d_L^{i'} = (V_{dL})_{ij}d_L^j \quad , \quad d_R^{i'} = (V_{dR})_{ij}d_R^j, \tag{2.15}$$

$$u_L^{i'} = (V_{uL})_{ij}u_L^j \quad , \quad u_R^{i'} = (V_{uR})_{ij}u_R^j, \tag{2.16}$$

and the 3×3 unitary matrix

$$V_{uL}V_{dL}^\dagger = V_{CKM} \tag{2.17}$$

is the CKM[13, 14] (Cabibbo, Kobayashi, Maskawa) mixing matrix for quarks:

$$\begin{pmatrix} d' \\ s' \\ b' \end{pmatrix} = \begin{pmatrix} V_{ud} & V_{us} & V_{ub} \\ V_{cd} & V_{cs} & V_{cb} \\ V_{td} & V_{ts} & V_{tb} \end{pmatrix} \times \begin{pmatrix} d \\ s \\ b \end{pmatrix} \tag{2.18}$$

The values of individual matrix elements can in principle all be determined from weak decays of the relevant quarks, or, in some cases, from deep inelastic neutrino scattering. Using the eight tree-level constraints discussed below together with unitarity, and assuming only three generations, the 90% confidence limits on the magnitude of the elements of the complete matrix are

$$\begin{pmatrix} 0.97383^{0.00024}_{0}.00023 & 0.2272^{0.0010}_{0.0010} & (3.69^{+0.09}_{-0.09})x10^{-3} \\ 0.2272^{0.0010}_{0.0010} & 0.97296^{+0.00024}_{0.00024} & (42.21^{+0.10}_{-0.80})x10^{-3} \\ (8.14^{+0.32}_{-0.64})x10^{-3} & (41.61^{+0.12}_{-0.78})x10^{-3} & 0.999100^{+0.000034}_{-0.000004} \end{pmatrix}. \tag{2.19}$$

As a result of the fact that V_{CKM} is not diagonal, the $W^\pm$ gauge bosons can couple to quarks of different generations. Within the SM, this is the only source of flavour changin interactions.

2.2 The top quark

The top quark, the heaviest known fundamental particle, was discovered thirteen years ago [15] at the Tevatron proton-antiproton collider located at the Fermi National Accelerator Laboratory in Batavia, Illinois. To date, the LHC is the only source of these quarks.

2.2.1 Importance of the top quark

Although it is almost as heavy as a gold atom it seems to behave as a point-like particle, at least at length scales $10^{-18}m$, according to experimental findings. So far the results are in accord with expectations and predictions within the standard model (SM) of particle physics. While the mass of this particle has already been precisely measured, other properties and its production and decay dynamics could, however, not be investigated in great detail so far. There are exciting physics topics to be explored and we mention here only a few of them.

In view of its large mass the top quark is an excellent probe of the mechanism that breaks the electroweak gauge symmetry and should therefore play a key role in clarifying the nature of the force(s)/particle(s) responsible for this phenomenon. The top quark is also a good probe for possible new parity-violating and/or non-SM CP violating interactions which could be induced, for instance, by non-standard Higgs bosons.

Are there new top-quark decay modes, for instance to supersymmetric particles? So far, experimental data are consistent with the SM prediction that $t \to W^+ b$ is the dominant mode but there are rooms to measure its branching ratio and the structure of the tWb vertex with higher accuracy.

Does the point-like behaviour of the top quark continue once it can be probed at distance scales significantly below $10^{-18}m$? These and other topics are in row to be studied.

The top quark is unique among the known quarks in that it decays before it can form hadronic bound states, so it offers the possibility to explore the interactions of a bare quark at energies of a few hundred GeV to several TeV. Furthermore, it is an important asset of top quark physics that not only the effects of the electroweak interactions, but also of the strong interactions of these particles can, in most situations, be reliably predicted.

Furthermore, the top quark is the most relevant parameter in the radiative electroweak corrections.

2.2.2 Top quark Identity Card

The only two accelerator complexes where top quarks are (or has been) produced and analyzed are the Tevatron and the LHC. So, the data below comes from the two experiments.

Mass

As the top quark does not hadronize, it seems natural to exploit the picture of the top quark being a highly unstable bare fermion. This suggests to use the concept of on-shell or pole mass, which is defined to be the real part of the complex-valued pole of the quark propagator. This is a purely perturbative concept. A quark is unobservable due to colour confinement, so its full propagator has no pole. In finite order perturbation theory the propagator of the top quark has a pole at the complex value $\sqrt{p^2} = m_t - i\Gamma_t/2$, where m_t is the pole or on-shell mass and Γ_t is the decay width of the top quark. However, the all-order resummation of a class of diagrams, associated with so called infrared renormalons, implies that the pole mass has an intrinsic, non-perturbative ambiguity of order $\Lambda_{QCD} \approx$ a few hundred MeV [16]. The so-called short distance masses, for instance the quark mass $\bar{m}_q(\mu_R)$ defined in the $\bar{M}S$ renormalization scheme, are free from such ambiguities. Here μ_R denotes the renormalization scale. The relation between the pole mass and the $\bar{M}S$ mass is known in QCD to $O(\alpha_s^3)$ [17]. Evaluating this relation for the top quark at $\mu_R = m_t$ it reads

$$m_t(\mu_R = m_t) = m_t \left(1 + \frac{4}{3}\frac{\alpha_s}{\pi} + 8.2364\left(\frac{\alpha_s}{\pi}\right)^2 + 73.638\left(\frac{\alpha_s}{\pi}\right)^3 + O(\alpha_s)^4\right) \tag{2.20}$$

where $\alpha_s(\mu_R = \bar{m}_t)$ is the $\overline{MS}$ QCD coupling for 6 flavours QCD. One should remember that the Eq. (2.20) has an additional uncertainty of $O(\Lambda_{QCD})$. Using $\alpha_s = 0,109$ we get $m_t/\bar{m}_t = 1.06$.

Thus, the $\overline{MS}$ mass is 10 GeV lower than the pole mass; $m_t = 171$ GeV (see below) corresponds to $\overline{m_t} = 161$ GeV. The present experimental determination of the top mass as at June 2012 combining all measurent from ATLAS and CMS ($\sqrt{s} = 7TeV$) is:

$$m_t^{exp} = 173.3 \pm 0.5 \pm 1.3\ GeV \tag{2.21}$$

The relative error is smaller than that of any other quark mass. In view of this precision the question arises how Eq. (2.21) must to be interpreted. As most of the measurements use kinematic variables, it seems natural to identify Eq. (2.21) with the pole mass. However, one should be aware that the present experimental determinations of the top mass cannot be related to observables which have been calculated in higher-order perturbative QCD in terms of a Lagrangian mass parameter.

As is well known, the value of the top-quark mass plays a key role in SM fits to electroweak precision data which yield constraints on the SM Higgs mass. The common practice is to interpret Eq. (2.21) as the on-shell mass m_t. With Eq. (2.21), the upper limit is $m_H < 200\ GeV$ (95% C.L.) [19]. In the following sections, m_t always refers to the pole mass. With no better alternative at present, we shall stick to interpreting Eq. (2.21) in terms of this mass parameter.

Lifetime

Because of top's large mass, it can decay into on-shell W bosons, i.e., the two-particle decay mode $t \to bW^+$ is kinematically possible. The SM predicts the top quark to decay almost exclusively into this mode (see Sec. 2.4). The prediction for the proper lifetime is $\tau_t \simeq 5 \cdot 10^{-25}$ s, an order of magnitude smaller the hadronization time $\tau_{had} \simeq 1/\Lambda_{QCD} \simeq 3 \times 10^{-24}$ s[20], which characterizes the time it takes for an (anti)quark produced in some reaction to combine with other produced (anti)quarks and form a colour-neutral hadron due to confinement. Thus, top quarks are unable to form top mesons $t\bar{q}$ or baryons tqq'. In particular there will be no spectroscopy of toponium $t\bar{t}$ bound states [20].

The decay width of the top quark manifests itself in the Breit-Wigner line-shape, i.e., the width of the invariant mass distribution of the top-decay products, $d\sigma/dM_t, M_t^2 = (\Sigma p_f)^2$. Unfortunately, the top width $\Gamma_t \simeq 1.3$ GeV is much smaller than the experimental resolution at the Tevatron or at the LHC. At present, no sensible method is known how to directly determine Γ_t at a hadron collider. In conjunction with some assumptions, an indirect determination is possible from the measurement of the $t\bar{t}$ and the single-top production cross sections [21].

An important consequence of the distinctive property of the top quark not forming hadrons pertains top-spin effects. The spin polarization and/or spin-spin correlations which are imprinted upon an ensemble of single top quarks or $t\bar{t}$ pairs by the production mechanism are not diluted by hadronization, but result in characteristic angular distributions and correlations of the final state particles/jets into which the top quarks decay [22]. In this respect top quarks offer a richer phenomenology than lighter quarks.

Spin, Colour and electric charge

There is no doubt that the top quark, as observed at the Tevatron, is a spin 1/2 fermion. The observed decay, $t \to bW$, the known spins of W and b, and the conservation of total angular momentum imply that the top quark is a fermion.

Top quarks, like the other quarks, carry colour charge: they transform as a colour triplet under the $SU(3)_c$ gauge group of the strong interactions. Colour confinement precludes the direct measurement of this quantum number; but indeed, measurements of the $t\bar{t}$ production cross section are consistent with the SM predictions for a colour triplet and antitriplet quark-antiquark pair.

The measurement of the top quark charge can be performed either by identifying the charge of its decay products in the main decay channel or by studying radiative top quark processes

As expected by SM, the top quark is the $I_3 = 1/2$ weak-isospin partner of the b quark, and his electric charge is $Q_t = 2/3$, in units of positron charge.

2.3 Production of $t\bar{t}$ pairs in p-p collisions

In perturbative QCD (pQCD), the total and differential cross sections for the process

$$pp \rightarrow t\bar{t} + X \tag{2.22}$$

can be calculated via the factorization theorem [23]. In this section we describe in detail the total and differential $t\bar{t}$ cross sections as well as the main sources of theoretical uncertainties.

2.3.1 Factorization theorem

The interaction between two protons, in general, is calculable in pQCD only in the presence of an hard scale characterizing the partonic cross section.

The motivation is to be attributed to the behaviour of the strong coupling constant, α_s. As a result of the renormalizability of the theory, the strong coupling depends on an unphysical scale μ_R, called *renormalization scale*, that is typically set equal to an high-energy scale or momentum transfer characterizing the given process. As we can see in Fig. 2.3, the strong coupling decreases with increasing transfer momentum, and in the high-energy limit, the coupling vanishes demostrating the asymptotic freedom property of QCD. On the other hand, α_S becomes very large at low transfer momenta and so it is not possible to use a perturbative approach to describe *soft* processes in QCD. Therefore one must introduce a cut-off parameter Λ_{QCD} which set the scale above which perturbative QCD is applicable.

A relation which bonds α_s to μ_R can be obtained using the Renormalization Group Equation; an equation that allows to investigate the changes of the strong coupling for varying renormalization scales. Writing $\alpha_s(\mu^2)$ as an expansion in powers of $1/ln(\mu_r^2/\Lambda_{QCD}^2)$, we have

$$\frac{\alpha_s(\mu^2)}{4\pi} = \frac{1}{\beta_1 ln(\mu^2/\Lambda_{QCD}^2)} - \frac{\beta_2 ln(ln(\mu^2/\Lambda_{QCD}^2))}{\beta_1^3 ln^2(\mu^2/\Lambda_{QCD}^2)} + O\left(\frac{1}{ln^3(\mu^2/\Lambda_{QCD}^2)}\right) . \tag{2.23}$$

Because the reaction which carry to the production of $t\bar{t}$ pairs occours in the low-α_s regime, where pQCD can be applied (see Fig. 2.3), we can divide (*factorize*) the overall process in two parts: one (perturbatively calculable) which includes only the "hard" interaction between the constituents of the hadrons (quarks and gluons), and the other which contains the information on the proton's parton distribution functions (PDF), that parametrize the proton constituents in the non-perturbative regime. The PDF are universal quantities, that is once determined in a given process can be used to compute cross sections for other perturbative hadronic processes.

Such separation requires the introduction of another energy scale, the *factorization scale* μ_F, in addition to the renormalization scale μ_R, which is necessary in any perturbative computation.

The factorization theorem permits us to calculate a cross-section as a convolution of the partonic cross sections with PDF:

$$\sigma(pp \rightarrow t\bar{t} + X) = \sum_{i,j} \int dx_a dx_b f_i(x_a, \mu_f^2) f_j(x_b, \mu_f^2) \hat{\sigma}_{i,j}(x_a, x_b, \alpha_s(\mu_r^2), \mu_F^2, \mu_r^2) , \tag{2.24}$$

where $\hat{\sigma}_{i,j}$ denotes the short-distance partonic cross section and f_i, f_j are the parton densities which include long-distance interactions. The dependence of an hadronic observable σ on μ_R

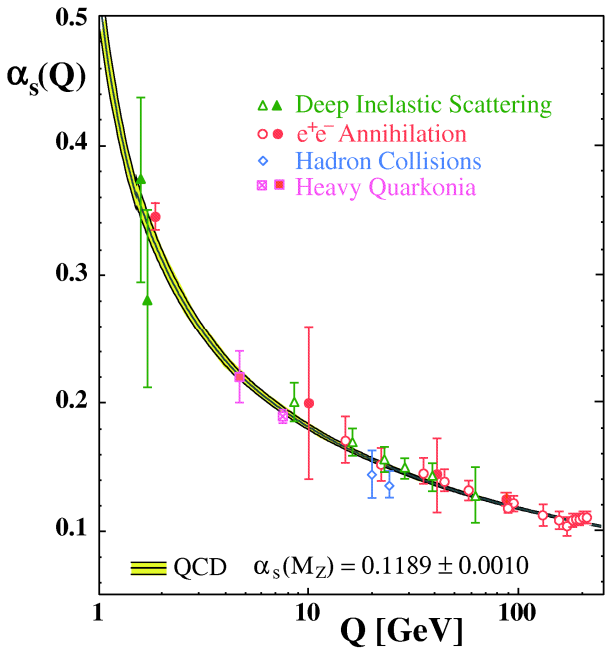

Figure 2.3: Running of α_S[24]

and μ_F decreases with increasing order of the perturbation series. Often one varies μ_R and μ_F in some range and takes the resulting spread in the value of σ – for no deeper reason – as an estimate of the theoretical error, i.e., of the size of the uncalculated higher-order perturbative contributions.

Fig. 2.5 illustrate the factorization idea: the process can be split into a short-distance part at the partonic level and a long-distance part which includes non-perturbative effects together with soft and collinear gluon radiation. $\hat{\sigma}$ denotes the partonic cross section (*hard process*) from which the mass singularities have been factorized. Typically, this process involves the radiation of gluons which give rise to the characteristic gluonic radiative corrections. Due to the zero-mass of the gluon and to the fact that the masses of the light quarks are negligible with respect to the exchanged energies, the radiative corrections contain infrared and mass singularities. The origin of infrared singularities is related to the soft gluon radiation whereas the mass singularities, also called collinear singularities, emerge if a quark radiates a collinear gluon. Although both soft and collinear gluon contributions can be calculated within perturbation theory, they are experimentally unresolvable. Therefore, they cannot be distinguished from other long-distance effects and are implicitly present in all measurements from which the parton densities are extracted. For a consistent computation of the hadronic cross section it is necessary that the short-distance partonic cross section is infrared-safe and also the mass singular terms have to be subtracted and absorbed into the parton densities.

2.3.2 Hard process

The essence of a "hard process" is that the quark is knocked out from the hadron as a bare particle. This occurs when the time-scale of the interaction ($1/Q$, where Q is the energy scale of the process) is little compared to the typical time-scale of interactions binding the proton ($O(1/m_p)$, with m_p the proton mass), so there is no time for other partons to negotiate a coherent response.

Because $m_t \gg m_p$, top quark production and decay processes are hard scattering reactions, and so they can be computed in QCD truncating their perturbative expansion at a fixed order

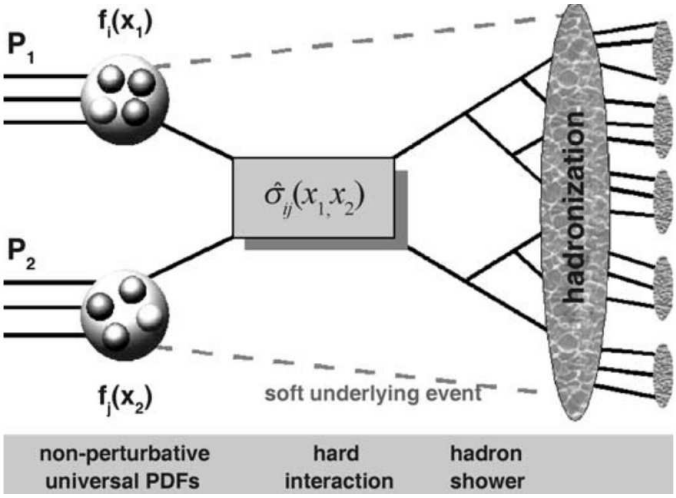

Figure 2.4: Sketch of a hadron-hadron interaction

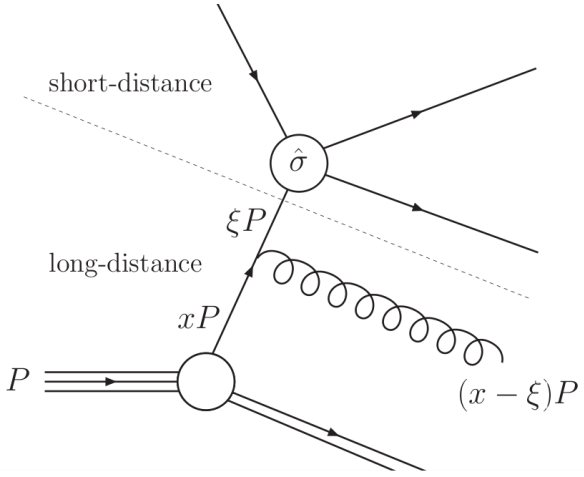

Figure 2.5: The schematic structure of a hadronic process as given by factorization.

in α_s:

$$\hat{\sigma}(p_1, p_2; Q; \mu_F^2) = \alpha_s^k(\mu_R^2) \left\{ \hat{\sigma}^{(LO)}(p_1, p_2; Q) + \alpha_s(\mu_R^2)\, \hat{\sigma}^{(NLO)}(p_1, p_2; Q; \mu_R^2; \mu_F^2) + ... \right\} \quad (2.25)$$

Although the 'exact' partonic cross section on the left-hand side of Eq. (2.25) does not depend on μ_R, each term on the right-hand side (and, hence, any fixed-order truncation) separately depends on it.

The LO (or tree-level) term $\hat{\sigma}^{(LO)}$ (relative Feynman diagrams are in Fig. 2.6) gives only an estimate of the order of magnitude of the partonic cross section, because at this order α_s is not unambiguously defined. Equivalently, we can say that since $\hat{\sigma}^{(LO)}$ does not depend on μ_R, the size of its contribution can be varied quite arbitrarily by changing μ_R in its coefficient $\alpha_s^k(\mu_R^2)$. The strong coupling α_s can be precisely defined only starting from NLO. A 'reliable' estimate of the central value of $\hat{\sigma}$ thus requires the knowledge of (at least) the NLO term $\hat{\sigma}^{(NLO)}$. This term explicitly depends on μ_R and this dependence begins to compensate that of $\alpha_s(\mu_R^2)$.

In general, the n-th term in the curly bracket of Eq. (2.25) contains contributions of the type $(\alpha_s(\mu_R^2) \ln Q/\mu_R)^n$. If μ_R is very different from the hard scale Q, these contributions become large and spoil the reliability of the truncated expansion. Thus, in practical applications the scale μ_R should be set approximately equal to the hard scale Q.

The fixed-order expansion provides us with a well-defined and systematic framework to com-

pute the partonic cross section $\hat{\sigma}(p_1, p_2; Q; \mu_F^2)$ of any hard-scattering process that is sufficiently inclusive or, more precisely, that is defined in an infrared- and collinear-safe manner. When the hard-scattering process involves two (or several) very different scales, say $Q_1 \gg Q$, the N^{n}LO term can contain double- and single-logarithmic contributions of the type $(\alpha_s L^2)^n$ and $(\alpha_s L)^n$ with $L = \ln(Q_1/Q) \gg 1$. These terms spoil the reliability of the fixed-order expansion and have to be summed to all orders by systematically defining logarithmic expansions (resummed calculations).

2.3.3 Parton Distribution Functions

As previously mentioned, the calculation of any cross-section in a hadron interaction relies upon the knowledge of the distribution of hadrons' constituents with their longitudinal momentum fractions, x, and because interaction within a baryon happens in high-α_s regime, they are non-perturbative quantities.

The main source of information on quark distributions inside hadrons come from the measurements of deep-inelastic scattering (DIS) structure functions in lepton-hadron scattering and of lepton pair production cross sections in hadron-hadron collisions, but also Drell-Yan, prompt-photon and jet production in hadron-hadron experments are needed to have complementary informations to extract the probability density $f_i(x, Q_0^2)$ of finding a parton i with x momentum fraction at momentum transfer scale Q_0. This densities are universally known as parton distribution (or density) functions.

The data coming from DIS and Drell-Yan processes cover a wide range in x and Q^2: HERA data are predominantly at lower x, while the fixed target data cover mostly the higher one. Jet data from hadron colliders cover a broad range in x and Q^2 themselves, but above all they are particulary important in the determination of the distribution of gluons, that are invisible in DIS experiments.

Thanks to the high $\sqrt{s}$ of the LHC, we can probe kinematic regions in x and Q^2 never explored before (Fig. 2.7), where at the moment PDF will rely exclusively on a large extrapolation (see below).

It is important to realize that the parton densities depend on the hadron structure alone and are completely independent of the nature of the hard process. This makes them universal and therefore, they can be used for the calculation of any hadronic cross section.

PDFs for the valence quarks and sea quarks are very different, as the latter are abundant at low x but negligible at $x \approx 1$, while valence quarks are peaked for larger values of x (as example, see Fig. 2.8).

The gluons distribution is similar to that of sea quarks, increases at low x, but gluons are more abundant. With respect to $q\bar{q} \to q\bar{q}$, $qq \to gg$, $qg \to qg$ the gluon gluon scattering $gg \to gg$ is also increased by large color factors, related to the larger multiplicity of gluon states, so that it is the dominant process in in pp or $p\bar{p}$ interactions at low x.

The PDFs are extracted from fits of the data described before at a fixed scale, say Q_0^2, after having assumed a functional x dependence at the same scale. Perturbative QCD can then predict the values of the PDF at any other scale μ^2 via the (Dokshitzer-Gribov-Lipatov-Altarelli-Parisi)

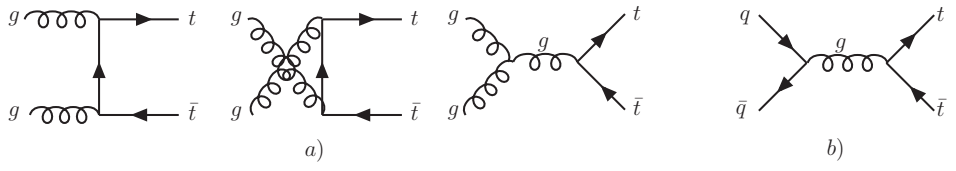

Figure 2.6: Lowest order Feynman diagrams for $t\bar{t}$ production by the strong interactions: $gg \to t\bar{t}$ (a) and $q\bar{q} \to t\bar{t}$ (b).

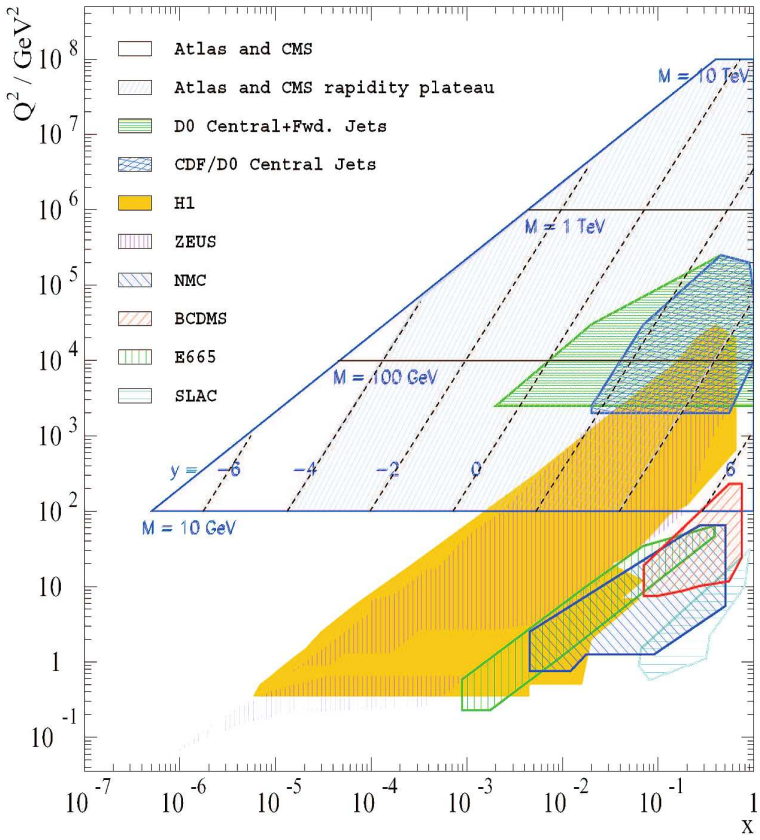

Figure 2.7: The Q^2-x kinematic plane for the LHC and previous experiments, showing the mass (M) and rapidity (y) dependence.

evolution equations[25]:

$$\frac{d\ f_a(x,\mu^2)}{d\ ln\mu^2} = \sum_b \int_0^1 \frac{dz}{z} P_{ab}(\alpha_s(\mu^2), z) f_a(x/z, \mu^2)\ . \tag{2.26}$$

The kernels $P_{ab}(\alpha_s, z)$ are the Altarelli-Parisi (AP) splitting functions, who can be computed as a power series expansion in α_s:

$$P_{ab}(\alpha_s, z) = \alpha_s P_{ab}^{(LO)}(z) + \alpha_s^2 P_{ab}^{(NLO)}(z) + \alpha_s^3 P_{ab}^{(NNLO)}(z) + \mathcal{O}(\alpha_s^4)\ . \tag{2.27}$$

The leading order (LO), next-to-leading order (NLO), and next-to-next (NNLO) leading terms $P_{ab}^{(LO)}(z)$, $P_{ab}^{(NLO)}(z)$ and $P_{ab}^{(NNLO)}(z)$ in the expansion are known, and the first two terms are used in most of the QCD studies.

The range of application of the DGLAP formalism does not cover the low x region, so in that case one must use the BFKL (Balitsky-Fadin-Kuraev-Lipatov[26]) description. However, at the moment there is no clear evidence of the need of BFKL formalism in the current range of the data, thus all global analyses use conventional DGLAP evolution of PDFs.

Global DGLAP fits

At the moment, there are various groups that are very active in the determination of PDF from DGLAP fits of existing data that is sensitive to them: these are the CTEQ and MSTW (formerly MRST) collaborations, and H1 and ZEUS experiments at HERA.

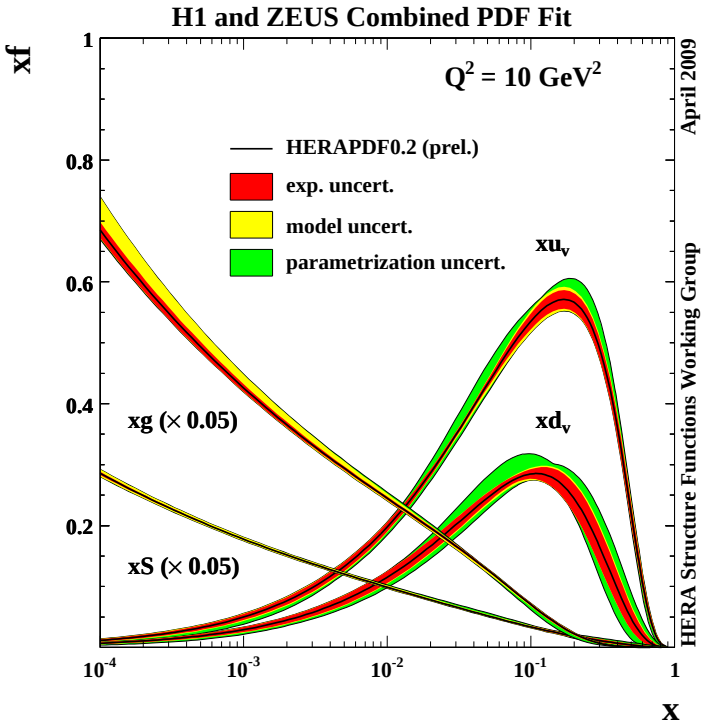

Figure 2.8: A recent set of HERA PDF determined by H1 and ZEUS collaboration at HERA.

Parton Luminosities

Because at hadron colliders the interaction which produces interesting events is between partons, it can be useful to define the parton-parton luminosity as:

$$\frac{dL_{ij}}{d\hat{s}\,dy} = \frac{1}{s}\frac{1}{1+\delta_{ij}}\left[f_i(x_1,\mu)f_j(x_2,\mu) + (1 \leftrightarrow 2)\right] . \tag{2.28}$$

where $y = 1/2ln(x_1/x_2)$ (x_i are the momentum fraction carried by the partons), and $\hat{s}$ is the square of the partonic center of mass. The Kronecker delta is useful to avoid the double-counting in case of identical partons. With this definition, the cross section in Eq. (2.24) can be rewritten as:

$$\sigma = \sum_{i,j}\int\left(\frac{d\hat{s}}{\hat{s}}\,dy\right)\left(\frac{dL_{ij}}{d\hat{s}\,dy}\right)(\hat{s}\,\hat{\sigma}_{ij}) \ . \tag{2.29}$$

Uncertainty on PDF

As PDF parameters are fitted from experimental data, they are affected by uncertainties which will propagate to any cross section calculated; these uncertainties affect mostly the gluon PDF, for which less measurements are available and evolution through a larger Q^2 range is needed in order to reach the energy scale of the interactions at LHC, while the densities for valence quarks are more constrained. In particular at the TeV scale, where one expect new physics, the interacting partons have higher momentum fractions and very high Q^2, and there the cross section predictions are dominated by PDF uncertainty.

There are many sources of uncertainty, but they can be divided into two classes: those which are associated with the "experimental" errors on the data that are fitted in the global analysis and those which are due to what can loosely be called "theoretical" errors, like those of input parametrisation form, neglected higher-order terms and higher-twist QCD corrections, electroweak corrections, choice of cuts, nuclear corrections, heavy flavour treatment.

To estimate the uncertainty, the CTEQ and MSTW groups, use the *Hessian* method, which consists in the study of the quadratic expansion of the χ^2 function about its global minimum.

The χ^2 function is defined as:

$$\chi^2_{global} = \sum_n \sum_I \left(\frac{D_{nI} - T_{nI}}{\sigma_{nI}} \right)^2 , \tag{2.30}$$

where T_{nI}, D_{nI}, and σ_{nI} are the theory value, data value, and uncertainty for data point I of data set (or "experiment") n. Having specified the effective χ^2 function, we find the parameter set that minimizes it to obtain a "best estimate" of the true PDFs. To study uncertainties, we must check the variation of χ^2_{global} in the neighborhood of its minimum, in an amount $\Delta\chi^2_{global}$.

Expanding χ^2_{global} with a Taylor series around its minimum and taking only the leading terms we obtain:

$$\Delta\chi^2_{global} \; = \; \chi^2_{global} - \chi^2_0 \; = \; \sum_{i=1}^{d} \sum_{j=1}^{d} H_{ij} \, (a_i - a_i^0) \, (a_j - a_j^0) \tag{2.31}$$

where H_{ij} is the Hessian matrix:

$$H_{ij} = \frac{1}{2} \frac{\partial^2 \chi^2_{global}}{\partial a_i \partial a_j} \; |_{min} \; . \tag{2.32}$$

The Hessian matrix has a complete set of orthonormal eigenvectors v_{ik} defined by

$$\sum_{j=1}^{d} H_{ij} \, v_{jk} = \epsilon_k \, v_{ik} \tag{2.33}$$

where $\{\epsilon_k\}$ are the eigenvalues. Now we can express the displacements from the minimum in terms of the eigenvectors:

$$a_i - a_i^0 = \sum_{k=1}^{d} v_{ik} \, s_k \, z_k \; , \tag{2.34}$$

where scale factors s_k are introduced to normalize the new parameters z_k such that

$$\Delta\chi^2_{global} \; = \; \sum_{k=1}^{d} z_k^2 \; . \tag{2.35}$$

i.e., $\sum_k z_k^2 \leq T^2$ is the interior of a hypersphere of radius T.

One of the most controversial aspect of PDF uncertainties is the determination of the excursion from the central value of the fit that represent a reasonable error: CTEQ choose a value of $\Delta\chi^2 = 100$, while MSTW choose $\Delta\chi^2 = 50$, so in general the uncertainties will be larger for the first set than the second. This difference indicates there is not a unique, rigorous manner in treating the error analisys for such large sample of data.

Fitting groups (CTEQ, MSTW), produce the eigenvector PDF sets $S_k^{\pm}$, with parameters a_i shifted from the global minimum:

$$a_i(S_k^{\pm}) = a_i^0 \pm t e_{ik} \tag{2.36}$$

with t adjusted to give the desired $T = \sqrt{\Delta\chi^2_{global}}$. Doing so, the final users can calculate the value of an observable O depending on PDF using the central value (which is the best fit estimate), and to find the uncertainty it is only necessary to evaluate O for each of the $2k$ set $(S_k^{\pm})$, and applying the formula:

$$\Delta O = \frac{1}{2} \sqrt{\sum_k \left[O(S_k^+ - O(S_K^-)) \right]^2} \; . \tag{2.37}$$

Again, there is another source of uncertainty in PDF sets: the global fits done to extrapolate PDFs are dependent on α_s value, which is not constant. Both CTEQ and MSTW agree to use a fixed value of $\alpha_s(M_Z^2)$, because the additional uncertainty associated to it is smaller compared to other souces of PDF uncertainties[28]. However, the two groups build PDF with different value of α_s, that may be useful for particular kind of analises.

2.3.4 Shower monte carlo

The factorization theorem alone does not fully describe the final state in hadronic collisions. First of all, we lack a practical way of computing QCD at low energy, and thus we are incapable to describe the formation of a final state made up of hadrons. But, even if we put aside this problem, we have seen that the formation of a specific final state involves an arbitrary number of collinear (and soft) emissions, all of them contributing corrections of order one. These corrections cancel for inclusive observables. However, a specific final state is not inclusive by definition, and so fixed order calculations cannot predict its probability. There are, however, algorithms that are capable to resum to all orders in perturbation theory the most important real and virtual emission corrections (namely the corrections that are collinear divergent), the so called *shower* algorithms. These algorithms are thus capable to associate with a given hard event an arbitrary number of accompanying partons. In order to yield a finite result, they must contain an explicit cut-off on the transverse momentum of emitted partons, and on their energy. The final state they generate is still unphysical, since it is made up by quarks and gluons, rather than hadrons. In order to generate a physical final state, phenomenological models of hadron formation are used. These models are not soundly motivated from a theoretical viewpoint. However, it is also true that the same models should be applicable to any hard collision, since the part of the collision that involves distances below the typical hadronic scale is well described by the perturbative QCD formalism embodied in the computation of the short distance cross section and of the shower development. Shower Monte Carlo programs are thus event generators that can model the full final state.

This pictures, still misses one ingredient for the description of the full final state. In fact, we still have to specify how to treat the remnant of the two initial hadrons that have provided the initial state partons. These remnants carry energy, momentum, flavour and colour, so their treatment is indispensable for a realistic description of the event. We are unable, at present, to describe this aspect of the process within QCD, and thus we have to resort to a model, the "underlying event" model. One very crude model would be to include the hadron remnant in the final state (for example, if the incoming parton is a quark, the hadron remnant is a di-quark), and provide a mechanism for the hadronization of the remnant (that will be typically correlated in colour to some final state partons) in the fragmentation stage of the shower.

2.3.5 From Tevatron to the LHC

As already said, the only two machines which have (or have had) enough center of mass energy to produce top-antitop pairs are the LHC and the Tevatron, which ended his operation in 2011.

The two main differences from Tevatron and the LHC are the center-of-mass energy (1.96 TeV at the Tevatron in run II, 14 TeV at the designed working point the LHC), and the type of hadron involved ($p-\bar{p}$ at the Tevatron, $p-p$ at the LHC).

At Tevatron energy the inclusive p-p cross section is much smaller with respect to the inclusive cross section for the p-$\bar{p}$ initial state. This justified the heavy work needed to produce an anti-proton beam used to achieve high luminosity. On the other hand, at the center-of-mass energy of 14 TeV of the LHC the difference between the p-p and the p-$\bar{p}$ becomes extremely small. As an example, in Fig. 2.9 we can see a comparison of the $t\bar{t}$ total cross section as a function of the center-of-mass energy $\sqrt{s}$. While at the Tevatron center-of-mass energy of 1.96 TeV the p-p and

p-$\bar{p}$ cross-section differ by almost a factor 3, their difference at the 14 TeV of the LHC amounts to less than 2%. The phenomenon is known as the Pomeranchuk theorem [29], and it predicts that the cross section for the particle-target and antiparticle-target collisions approach the same value as the energy tends toward infinity. As explained in Section 2.3.3, high-energy particles probe the proton (or antiproton) more deeply, therefore they interact with partons with low x, where the sea partons are greatly dominant and distribution are similar in all baryons, so the interaction probability is the same in the asymptotic regime. For comparison, the experimental point in the figure indicates $\sigma_{t\bar{t}}$ as measured by the D0 experiment ($7.83^{+0.92}_{-0.85}$[30]).

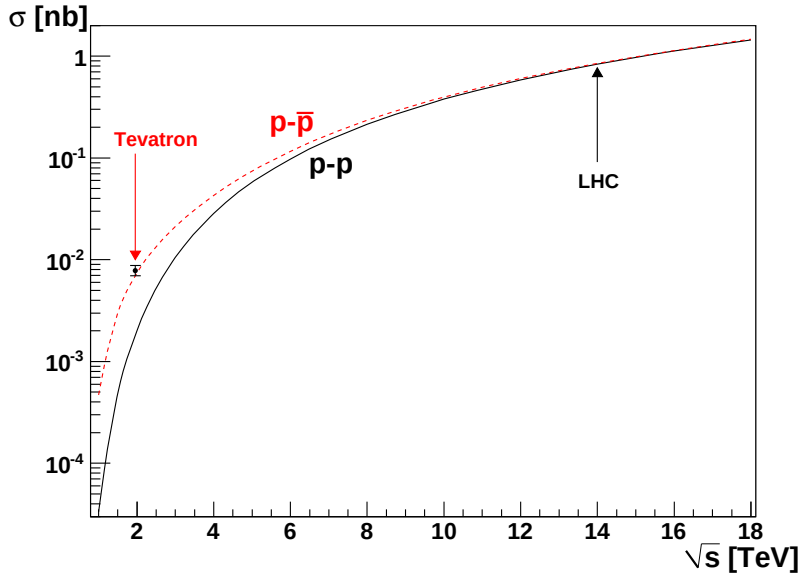

Figure 2.9: Difference in the $t\bar{t}$ production cross-section between $p-p$ and $p-\bar{p}$ colliders.

For the process ($p-p(or\ p-\bar{p}) \to t\bar{t}$), we must consider not only the parton luminosity, to estimate the production rate, but also the partonic cross sections. At LHC the highest partonic luminosity (L_{xy}, where x, y is a combination of partons) is provided by the quark-gluon initial state (Fig. 2.10). However, as can be seen from the cross section plot of Fig. 2.10, the parton level cross section $\hat{\sigma}_{qg\to t\bar{t}}$ is much smaller than the partonic cross section for the $q\bar{q}$- or gg-initiated processes, since the qg-channel is of order α_s^3 and thus formally a NLO correction. As a consequence, in the total hadronic cross section the qg-channel gives only a contribution at the percent level (see second last plot in Fig. 2.10). In principle the same argument applies for $\bar{q}g$-channel, however its contribution to the hadronic cross section is even further suppressed because of the smaller parton luminosity.

The second largest parton flux is delivered by the gg-channel. In combination with the large partonic cross section $\hat{\sigma}_{gg\to t\bar{t}}$ this is the most important channel at LHC, resulting in about 90% of all top-quark pairs produced via gluon fusion.

The parton luminosity $L_{q\bar{q}}$ ranks third at LHC. The corresponding parton cross section $\hat{\sigma}_{q\bar{q}\to t\bar{t}}$ vanishes in the high energy limit in contrast to the gg- and qg-case where the partonic cross sections approach a constant value at high energies. Thus, the $q\bar{q}$-contribution to the hadronic cross section saturates well below 1 TeV and adds the known 10% at LHC.

At the Tevatron, the situation is reversed (see Fig. 2.10). The luminosities L_{ij} are ordered in magnitude according to $L_{q\bar{q}} > L_{qg} > L_{gg}$. This makes the $q\bar{q}$-channel by far the dominant one contributing 85% to the hadronic cross section $\sigma_{pp\to t\bar{t}X}$, while gluon fusion almost makes up for the rest.

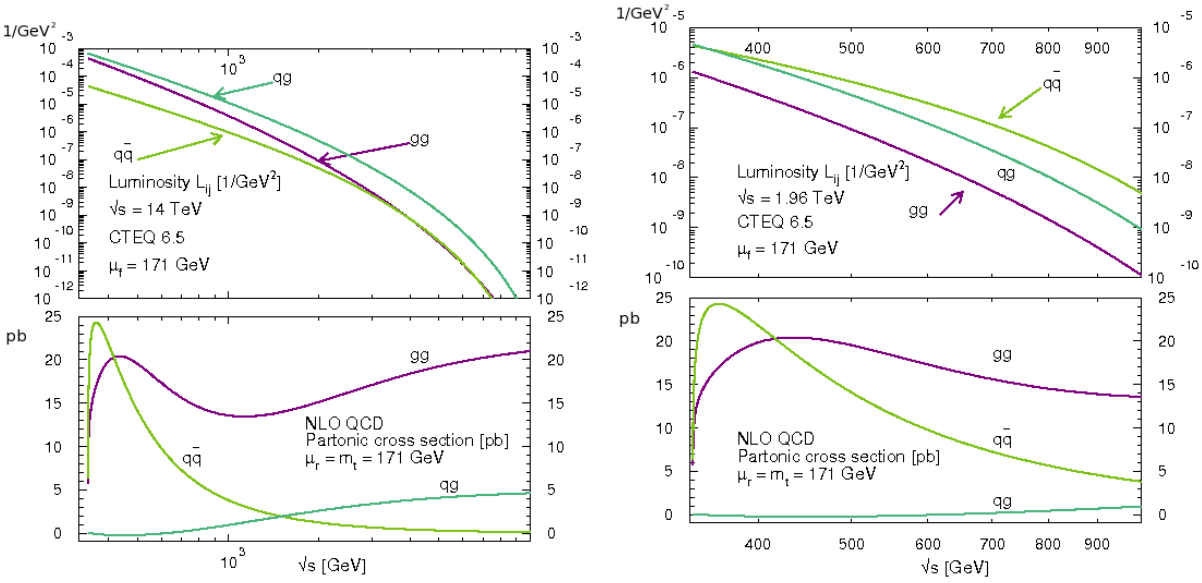

Figure 2.10: Parton luminosities and cross sections for LHC and Tevatron, $m_t = 171$ GeV, $\mu = m_t$ and the CTEQ6.5 PDF set [31]

2.4 Top Decay

In the SM, which involves three generations of quarks and leptons, the only two-particle decays of the top quark[1] which are possible to lowest order in the (gauge) couplings are $t \to bW^+$, $t \to sW^+$, and $t \to dW^+$. Their rates are proportional to the squares of the CKM matrix elements $|V_{tq}|^2$, $q = b, s, d$, respectively. The rate of $t \to X$, i.e. the total decay width Γ_t of the top quark, is given by the sum of the widths of these three decay modes, as the branching ratios of the loop-induced flavour-changing neutral current decays are negligibly small in the SM. The analysis of data from weak decays of hadrons yields $0.999096 < |V_{tb}| < 0.999134$ at 95% C.L. [32], using the unitarity of the CKM matrix. The unitarity relation $|V_{tb}|^2 + |V_{ts}|^2 + |V_{td}|^2 = 1$ implies that the total decay rate is completely dominated by $t \to bW^+$. Branching ratios are:

$$B(t \to bW^+) = 0.998, \qquad B(t \to sW^+) \simeq 1.9 \times 10^{-3}, \qquad B(t \to dW^+) \simeq 10^{-4} \tag{2.38}$$

So, the total decay width of the top quark is given by the partial width of the decay $t \to bW^+$, more precisely, of the sum of the widths of the decays

$$t \to b\,W^+ \;\to\; b\,\ell^+\nu_\ell, \quad b\,u\,\bar{d}, \quad b\,c\,\bar{s}, \quad \cdots \tag{2.39}$$

Taking the intermediate W boson to be on-shell, one gets to Born approximation:

$$\Gamma_t^B \equiv \Gamma_t^B(t \to bW) = \frac{G_F}{8\pi\sqrt{2}} m_t^3 |V_{tb}|^2 \left(1 - \frac{m_W^2}{m_t^2}\right)^2 \left(1 + 2\frac{m_W^2}{m_t^2}\right) = 1.44\,\text{GeV}, \tag{2.40}$$

where G_F is the Fermi constant, $m_t = 171$ GeV and $m_W = 80.40$ GeV has been used, and the mass of the b quark ($m_b \simeq 4.9$ GeV) has been neglected. The order α_s QCD corrections [33], the order α weak and electromagnetic corrections [34, 35], and the corrections due to the width of off-shell W bosons [36] and to $m_b \neq 0$ were determined quite some time ago. Moreover, the order α_s^2 QCD corrections were computed as an expansion in $(m_W/m_t)^2$ [37, 38]. Thus, the SM prediction for the radiatively corrected width may be represented by the following expression [37, 38]:

$$\Gamma_t = \Gamma_t^B\,(1 - 0.81\alpha_s - 1.81\alpha_s^2) \tag{2.41}$$

[1] Unless stated otherwise, the discussion of this section applies analogously also to $\bar{t}$ decays.

where $\alpha_s = \alpha_s(m_t)$ is the QCD coupling in the $\overline{\text{MS}}$ renormalization scheme. With $\alpha_s(m_t) = 0.108$ the correction factor to the lowest-order width is 0.89. Thus for $m_t = 171$ GeV we have $\Gamma_t = 1.28$ GeV.

For the dominant semileptonic and nonleptonic decay modes (eq. 2.39) the branching ratios are, for $\Gamma_W, m_b \neq 0$ and including the $O(\alpha_s)$ QCD corrections:

$$B(t \to b\ell^+\nu_\ell) = 0.108 \quad (\ell = e, \mu, \tau), \qquad B(t \to bq\bar{q}') = 0.337 \times |V_{q\bar{q}'}|^2 . \tag{2.42}$$

Using the central values of the respective CKM matrix elements [32] we have then $B(t \to bu\bar{d}) = B(t \to bc\bar{s}) = 0.328$, $B(t \to bu\bar{s}) = 0.017$, and $B(t \to bc\bar{b}) = 6 \times 10^{-4}$.

2.4.1 W boson helicity in top quark decay

The Standard Model dictates that the top quark has the same V-A charged-current weak interaction as all the other fermions $\left(-ig\sqrt{2}V_{tb}\gamma^\mu 1/2(1-\gamma_5)\right)$. This implies that the W-boson in top quark decay cannot be right-handed i.e. have positive helicity. In the idealised limit of a massless b-quark, the V-A current dictates that the b-quark in top decay is always left-handed. If the W-boson were right-handed, then the component of total angular momentum along the decay axis would be $+3/2$ (there is no component of orbital angular momentum along this axis). But the initial top quark has spin angular momentum $\pm 1/2$ along this axis, so this decay is forbidden by conservation of angular momentum (Fig. 2.11).

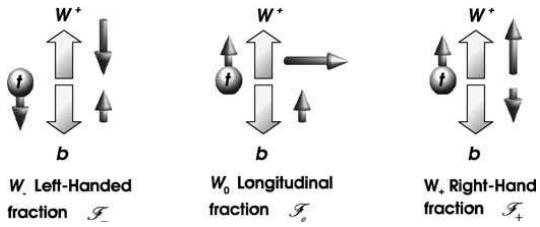

Figure 2.11: Forbidden W-boson helicity

So, the top quark may decay to a left-handed (negative helicity) or a longitudinal (zero helicity) W-boson, with a little preference to longitudinal polarization [39]:

$$B(t \to W_0 b) \approx \frac{m_t^2}{m_t^2 + 2M_W^2 + m_b^2} = 70.3 \pm 1.2\% \tag{2.43}$$

Direct measurements of the boson polarization made with ATLAS give $F_0 = 0.67 \pm 0.07$, $F_L = 0.32 \pm 0.04$[40], where F_0 and F_L are the longitudinal and left-handed fractions, respectly.

2.4.2 Decay channels

Given that the top quark decays almost 100% of the time as $t \to Wb$, typical final states for the leading pair production process can therefore be divided into three classes (Fig. 2.12):

A.	$t\bar{t} \to W^+bW^-\bar{b} \to q\bar{q}'bq''\bar{q}'''\bar{b}$	(46.2 %)
B.	$t\bar{t} \to W^+bW^-\bar{b} \to q\bar{q}'b\ell\bar{\nu}_\ell\bar{b} + \bar{\ell}\nu_\ell bq\bar{q}'\bar{b}$	(43.5%)
C.	$t\bar{t} \to W^+bW^-\bar{b} \to \bar{\ell}\nu_\ell b\ell'\bar{\nu}_{\ell'}\bar{b}$	(10.3%)

The quarks in the final state evolve into jets of hadrons. A, B, and C are referred to as the all-jets, lepton+jets (ℓ + jets or semileptonic), and dilepton ($\ell\ell$) channels, respectively.

The signature for the ℓ + jets channel, that is the decay mode studied in our analysis, consists of an isolated, high p_T charged lepton, large missing transverse energy/momentum, and at least four jets, two of which originate from b quarks.

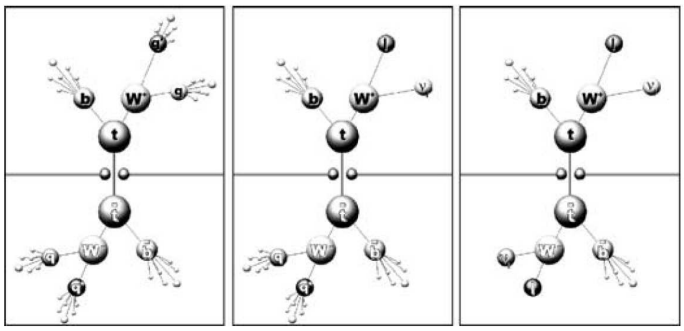

Figure 2.12: Schematic diagrams of $t\bar{t}$ decay channels

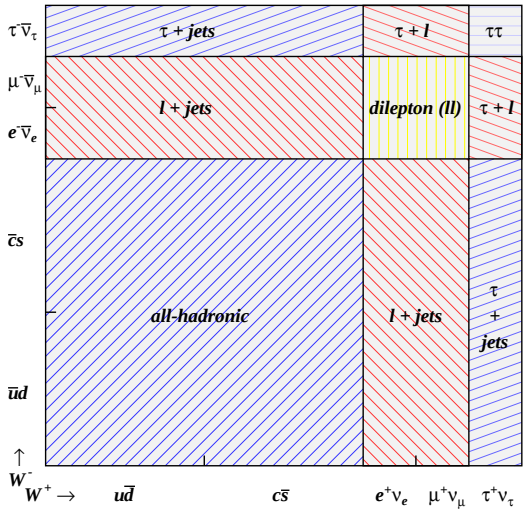

Figure 2.13: Illustration of the various $t\bar{t}$ decay modes via the possible W boson decay.

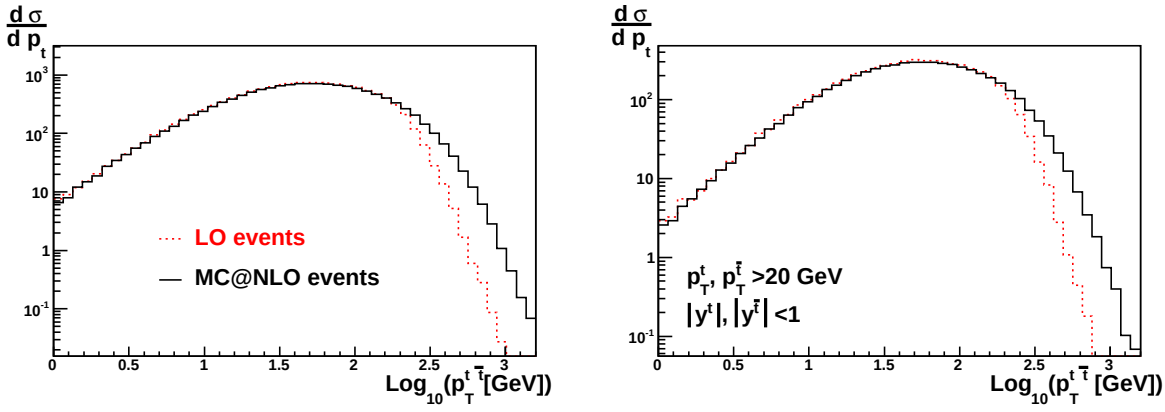

Figure 2.14: Transverse momentum of $t\bar{t}$ pair in LO Monte Carlo (HERWIG) and in MC@NLO. With acceptance cuts on the right.

2.5 Monte Carlo

A reliable and well-understood Monte Carlo (MC) simulation of signal and background processes is a crucial ingredient for any high-energy physics analysis, for example to understand detector acceptances, derive selection efficiencies and model expected kinematic distributions and their normalisation. It requires both good modelling of the physics process of interest from the parton to the hadron level and an accurate simulation of the actual detector's response when exposed to such a signature.

MC simulations of hadron interactions are based on the factorisation theorem discussed in Section 2.3.1. The interaction of the incoming partons in the hard process of interest is then evaluated based on fixed-order (NLO, in our case) matrix elements, yielding the outgoing partons and their characteristics like momenta and colours. The following parton shower adds higher-order effects by allowing partons to split into pairs of partons (gluon radiation, gluon-splitting, photon radiation,...) until at a sufficiently low Q^2 scale non-perturbative hadronization sets in, forming colour-neutral hadrons from the coloured partons based on phenomenological models. Unstable particles and resonances then need to be decayed appropriately.

In principle, for every stage in the above process different programs and models can be used, and the best choice may depend on the process to be studied. For our study, the program MC@NLO[41] has been used.

Simplest MC are based on a leading-order (LO) QCD calculation of the hard Process, combined with a leading-logarithmic (LL) treatment of higher orders via the parton shower approximation. Also, there are some MC which can do next-to-leading order calculation in the event generator, but is highly non-trivial to incorporate the benefits of NLO calculations into event generator. MC can generate events with real parton emission in a kinematical configuration that can be the same of the NLO computation, and this may lead to a *double counting*, therefore an overstimated correction (in excess or in defect) of the total rate of any cross section.

On the other hand, the parton showers cannot be omitted, since they provide a reliable description of how final state partons evolve into QCD jets.

The goal of combining NLO computations with parton showers was reached in programs like MC@NLO. The basic idea is to modify the substraction method utilized in the NLO computation to take in account the terms generated by the parton shower. However, some event carry a negative weight[2]. With this trick, the total rates coming from the NLO computation are the same of MC, so the double-counting is avoided.

A comparison between the predictions of MC@NLO and LO MC, obtained at $\sqrt{s}$ =14 TeV is

[2]These negative weights are of a different nature from the negative contribution that appear in NLO computation.

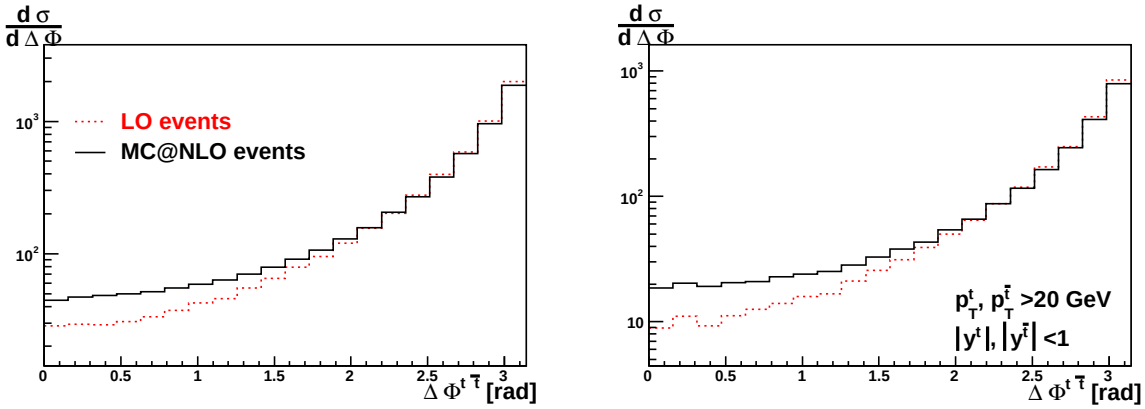

Figure 2.15: Angular distance from t to $\bar{t}$ in LO Monte Carlo (HERWIG) and in MC@NLO. With acceptance cuts on the right.

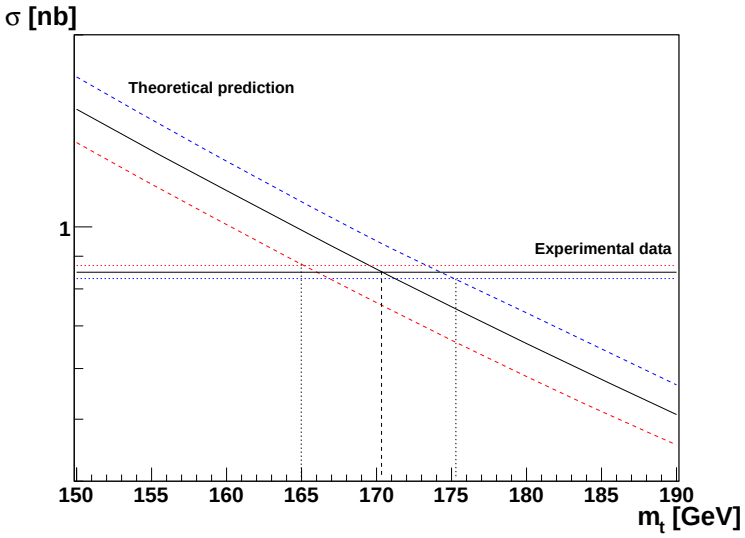

Figure 2.16: Example of top mass measurement from comparison between theoretical predictions on cross section and experimental data, with relative uncertainty.

shown in Fig. 2.14 and Fig. 2.15. In the first plot the single differential cross section, $d\sigma/dp_T^{t\bar{t}}$, as a function of the transfer momentum of the $t\bar{t}$ pair is shown and compared with the leading order predictions obtained with the HERWIG MC program [42]. In the low transverse momentum region the LO and the NLO predictions agrees with each other but in the high $p_T^{t\bar{t}}$ region, which is populated by events in which a hard parton recoils against the $t\bar{t}$ pair, MC@NLO predict a much larger cross section with respect to HERWIG. The same complementary behaviour is shown when applying realistic acceptance cut on the $t\bar{t}$ pair (in the right picture).

An analogous interpretation one can make for the azimuthal difference between t and $\bar{t}$ in the transverse plane, denoted by $\Delta\phi^{t\bar{t}}$ and plotted in Fig. 2.15. In the region $\Delta\phi^{t\bar{t}} \simeq 0$, populated by configurations in which a hard jet recoils against the $t\bar{t}$ pair, MC@NLO predict a larger differential cross-section, and this difference is more evident when applying standard acceptance cut (right picture).

2.5.1 Study of $t\bar{t}$ with MC@NLO

First of all, one need an analysis of the pure $t\bar{t}$ pair production, so we neglet the underlying event and take the tops undecayed.

We emphasized that a physics observable cannot depend on non-physical parameters, like the renormalization and the factorization scales, in an all-orders calculation. However, theoretical predictions of observables are typically obtained calculating only the first terms of the perturbative expantion and do depend on the renormalization and factorization scales. In addition, the PDF are themselves affected by experimental and theoretical uncertainties, as already explained, and these uncertainties propagate to the $t\bar{t}$ cross section.

It is important to evaluate the total theoretical uncertainty affecting the $t\bar{t}$ cross section not only to access the theoretical precision of the NLO calculation, but also because this theoretical uncertainty directly translates into an uncertainty of the top quark mass. This is illustrated in Fig. 2.16 that shows the total $t\bar{t}$ pair cross section as a function of the top quark mass value assumed in the calculation. In the figure, this theoretical cross section is compared with an hypothetical measurement of the $t\bar{t}$ cross section affected by 1% experimental uncertainty. As can be seen, this translates in a almost 5 GeV/c^2 uncertainty on the top mass.

Altough this method is rather crude (in the next chapter we will determine the top mass in a more sophisticated way) it nicely illustratethat in order to extract QCD parameters theory predictions affected by the smallest theoretical uncertainties are required.

In the following we will describe the uncertainties on the total and differential $t\bar{t}$ cross sections due to the uncalculated high-order terms and the PDF-related uncertainties.

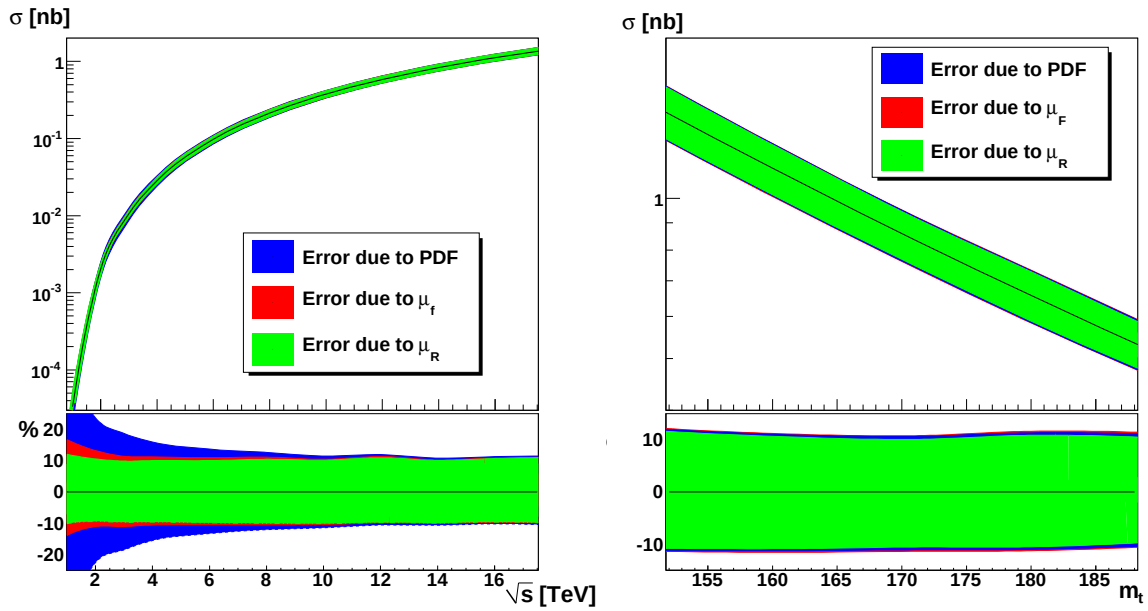

Figure 2.17: Total estimation of errors on $\sigma_{t\bar{t}}$ due to μ_R, μ_F and PDF uncertainty, for different $\sqrt{s}$ and for different top quark masses.

Scales and PDF uncertainties

To estimate the uncertainty due to renormalization and factorization scales, we have varied, following a well established convention, these scales by a factor two up and down, and taken the corresponding variation as an estimate of the uncertainty due to the high-order terms.

To estimate the uncertainty related to the PDF we have instead followed the Hessian method explained in Section 2.3.3.

The resulting total theoretical uncertainty, obtained by adding in quadrature these two con-

tributions, are shown for the total $t\bar{t}$ cross section in Fig. 2.17, as a funcion of $\sqrt{s}$ and m_t. For all the calculations the reference values of μ_R and μ_F have been taken equal to the top transverse mass, $\sqrt{m_t^2 + p_T^2}$, the top mass has been assumed to be equal to the PDG value, m_t=171.2 GeV, and the set CTEQ 6.6 has been used for the PDF in the calculations.

From Fig. 2.17 it is clear that the renormalization scale uncertainty is by far the largest component contributing to the total uncertainties. It amounts to $\simeq$11% and it is almost independent of the center-of-mass energy and the top mass. The factorization scale uncertainty instead is almost negligible at high $\sqrt{s}$ with respect to the one due to the renormalization scale but increasing at low $\sqrt{s}$ up to 10%. The uncertainties related to the PDF are at level of 3-4% level at the LHC center-of-mass energy and increase significantly with decreasing $\sqrt{s}$.

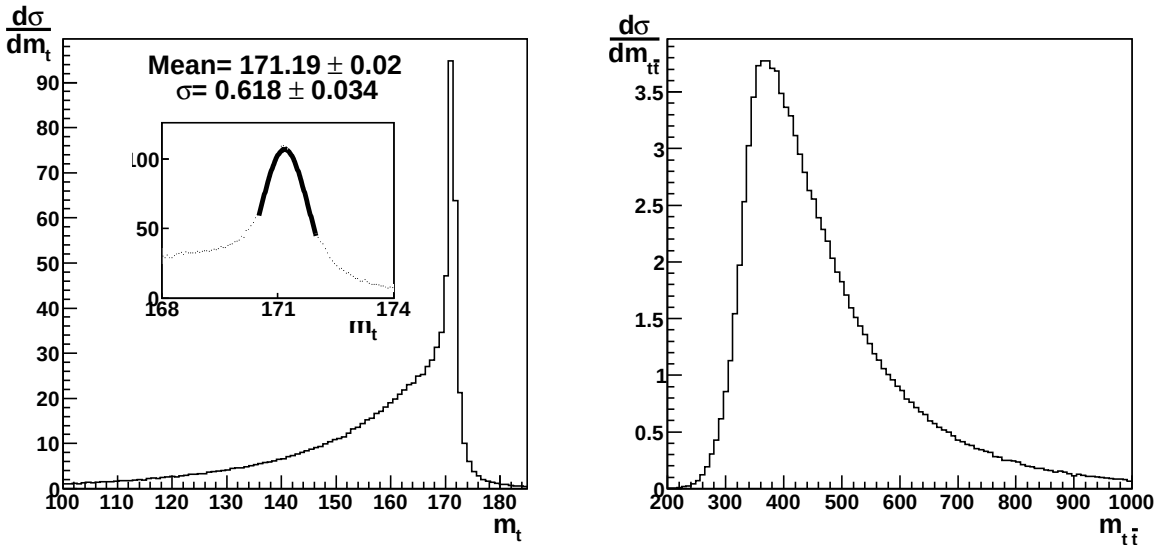

Figure 2.18: Invariant mass of top quark (left) and top quark pair (right), obtained from b quark and direct w boson decays.

For the total theoretical $t\bar{t}$ cross section at 14 TeV, we have obtained the following final value:

$$\sigma_{t\bar{t}} = 836\ (\pm 84)_{\mu_R}\ (\pm 14)_{\mu_F}\ (\pm 29)_{PDF}\ \ pb \tag{2.44}$$

that has to be compared with a recent prediction for the same cross section at NLO (with $m_t = 171$ GeV) [43]:

$$\sigma_{t\bar{t}} = 877\ \left(^{+105}_{-103}\right)_{scales}\left(^{+28}_{-29}\right)_{PDF}\ \ pb \tag{2.45}$$

and an approximate NNLO calculation[43], which resulted in:

$$\sigma_{t\bar{t}} = 944\ \pm 4_{kin}\ \left(^{+72}_{-47}\right)_{scales}\left(^{+30}_{-31}\right)_{PDF}\ \ pb \tag{2.46}$$

Invariant mass

In Fig. 2.18 the single differential cross section, as a function of the top quark and top quark pair invariant masses, reconstructed using the top decay products is shown. In the left plot, in addition to the top mass peak, is visible a long tail towards smaller invariant masses. This tail is due to the final state QCD radiation of gluons that is not taken into account in the calculation of the invariant mass. The differential cross section $d\sigma/dm_{t\bar{t}}$ extends up to invariant masses as high as 1 TeV. Various studies beyond the standard model try to identify new particles as resonances that will appear above this QCD standard model background.

2.5.2 Leptons from W decay

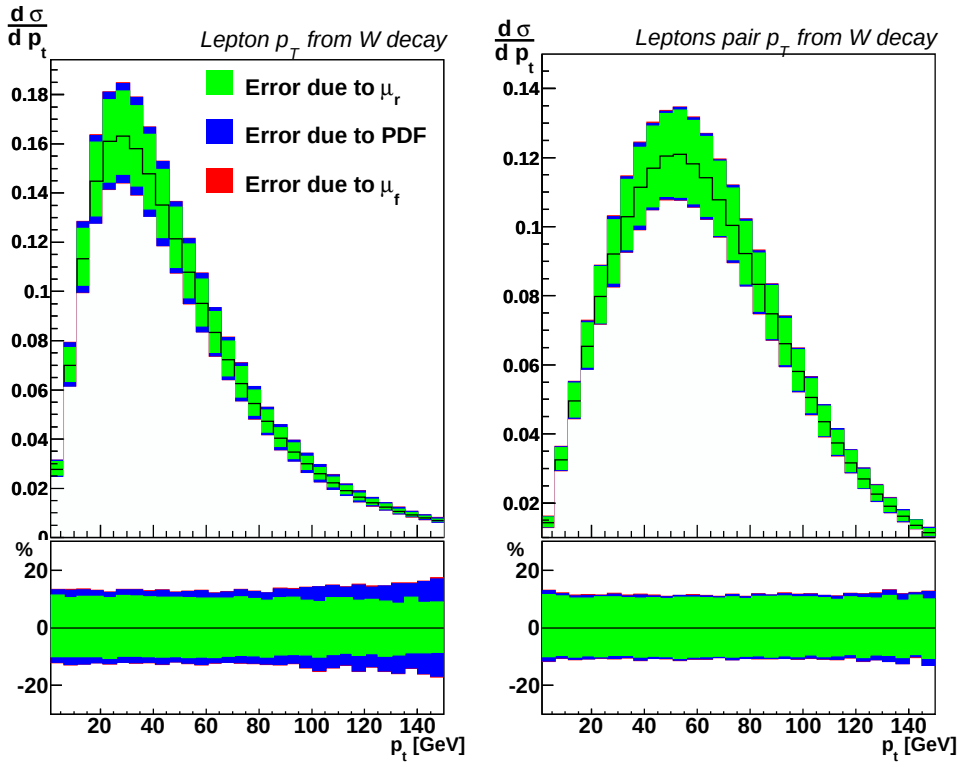

Figure 2.19: Uncertainties in transverse momentum of (left) leptons and (right) lepton pair coming from W-decay.

We next study the characteristics of the charged leptons coming from the W-boson decay (Fig. 2.19 and Fig. 2.20). The single differential cross section as a function of the transverse momentum of the electron shows a characteristic peak around 40 GeV. Its theoretical uncertainty is again dominated, for most of the p_T spectrum, by the renormalization scale uncertainty. The PDF related uncertainty increase with increasing p_T. The right figure shows the single differential cross section and its total uncertainty, this time as a function of the transverse momentum of the di-lepton pair.

The cross sections as a function of the pseudorapidity of the lepton and lepton pairs are presented in Fig. 2.20, and are symmetric around $\eta = 0$. In this case, in addition to the usual renormalization scale uncertainty the PDF related uncertainties increase and dominate the total uncertainty in the forward and rear rapidity regions.

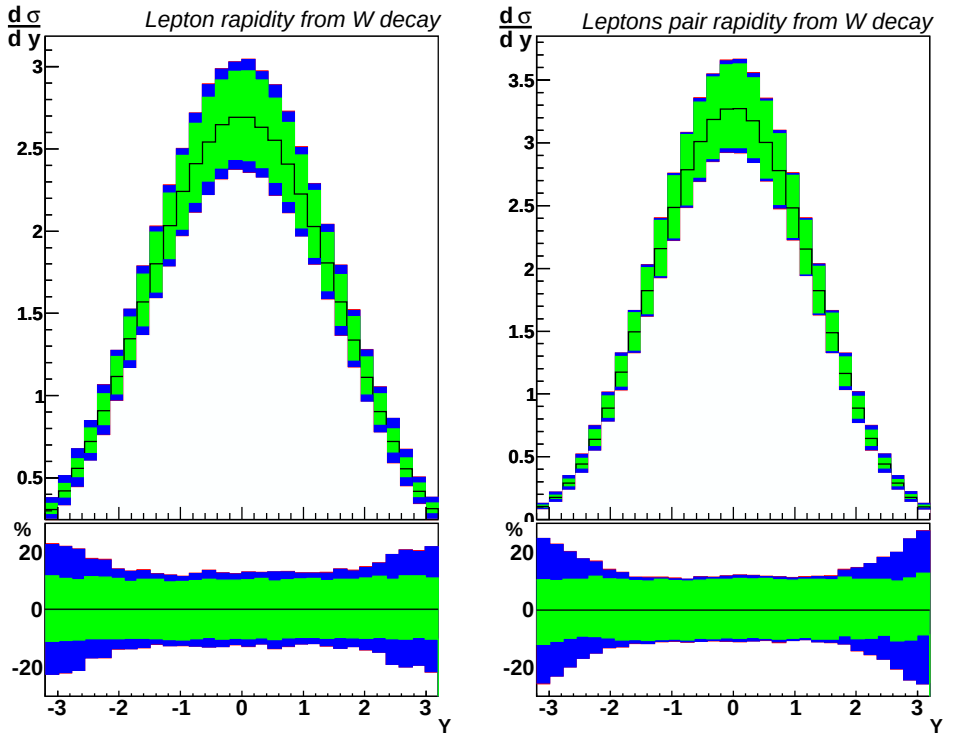

Figure 2.20: Uncertainties in rapidity of (left) leptons and (right) lepton pair coming from W-decay.

Chapter 3

Measurement of $t\bar{t}$ production in the semileptonic channel

3.1 $t\bar{t}$ Event characteristics

In the Standard Model, the decay of the top quarks take place almost exclusively trough the $t \to Wb$ decay mode. A W-boson decay in about 1/3 of the cases into a charge lepton and a neutrino. All three leptons flavours are produced at approximately equal rate. In the remaining 2/3 of the cases, the W^+-boson decays into a quark of up-type and an anti-quark of down-type, e.g. $W^+ \to c\bar{s}$, and similarly for the W^-. Since the CKM matrix suppresses decays involving b-quarks as $|V_{cb}|^2 \sim 1.7 \times 10^{-3}$, W-boson decay can be considered as a clean source of light quarks.

From an experimental point of view where one measures final states, one characterises top pair events by the number of W-bosons that decay leptonically. A value of 10.8% and 67.6% has been used for the leptonic and hadronic branching ratio (BR) of the W-boson, respectively. The following signatures can be identified:

- *Fully leptonic*: represents about 1/9 of the $t\bar{t}$ events. Both W-bosons decay into a lepton-neutrino pair, resulting in events with two charged leptons, two neutrinos and two b-jets. This mode is identified by requiring two high p_T leptons and the presence of missing transverse energy (MET), and allows a clean sample of top quark events to be obtained. However, this sample has limited use in probing the top quark reconstruction capability of the ATLAS experiment, due to the presence of two neutrinos.

- *Semi-leptonic*: represents about 4/9 of the $t\bar{t}$ decays. One W boson decays leptonically, the other hadronically. The presence of a single high p_T lepton helps to suppress the Standard Model QCD background. The p_T of the neutrino can be reconstructed as it is the only source of MET for signal events.

- *Fully hadronic*: represents about 4/9 of the $t\bar{t}$ decays. Both W-bosons decay hadronically, which often gives at least six jets in the event: two b-jets from the top quark decay and four light jets from the W-boson decay. In this case, there is no high p_T lepton to trigger on, and the signal is not easily distinguishable from the abundant Standard Model QCD multi-jets production, which is expected to be many orders of magnitude bigger than the signal. Another challenging point of this signature is the presence of a high combinatorial background when reconstructing the top quark mass.

In this analysis we will consider $t\bar{t}$ events in the semileptonic channel:

$$pp \to t\bar{t} \to W^+W^-b\bar{b} \to l\nu_l q\bar{q}b\bar{b}. \tag{3.1}$$

that is characterized by a single high-p_T lepton, a neutrino (and hence, missing transverse energy) and high-p_T hadronic jets originating from the b-quarks and the light quarks of the W-boson taht decays hadronically. This will be than our main experimental signature and after having discussed the quality of the reconstruction of the relevant experimental objects (electron, muon, MET and hadronic jets), we will describe how an effective event selection can be developed to measure top pair production.

In the analysis, we will consider the 2011 data taking period, where protons collided at a center of mass energy of 7 TeV, for a total integrated luminosity of 4.7 fb^{-1}.

3.2 Physics backgrounds

In this section we describe the most important background processes, listed in Table 3.1, that can give rise to a similar experimental signature to the $t\bar{t}$ process we are interested in.

Process	Events in e+jets	Events in μ+jets
W + jets	1102	2131
Z + jets	224	252
Single top	670	1114
QCD multijet	1443	1088
Di-boson production (WW, WZ, ZZ)	23	41

Table 3.1: Most relevant background processes for the electron channel.

W + jets

The major source of background in $t\bar{t}$ production is W-boson + jet production. Its cross section is large, and the leptonic decay of the W-boson results in a large MET, one of the main signatures of the top events (Section 3.8). Since both the overall normalisation and the heavy flavour (HF) composition are not accurately known in MC, a data driven approach is required.

To extract the overall normalisation, the charge asymmetry method is used. At LHC, where protons collide wit protons, the production of W bosons is characterized by a charge asymmetry, due to relative differences in the quark-antiquark composition of the proton, which led the W^+ boson to be statistically more produced than the W^- boson.

The ratio of the cross-sections, $r = \frac{\sigma(pp\to W^+)}{\sigma(pp\to W^-)}$ is theoretically well understood (the main uncertainty is the PDFs one amounting to a few percent), and is much better known then the prediction of the W+jets production, with a number of jets bigger than three. One can use that ratio to estimate the total number of W+jets background:

$$N_{W^+} + N_{W^-} = \frac{N^{MC}_{W^+} + N^{MC}_{W^-}}{N^{MC}_{W^+} - N^{MC}_{W^-}}(D^+ - D^-) = \left(\frac{r_{MC}+1}{r_{MC}-1}\right)(D^+ - D^-) \tag{3.2}$$

where D^+ and D^- are the total number of events selected in data with respectly a positively and a negatively charged lepton, while r_{MC} was evaluated from Monte Carlo simulation. Since the charge asymmetry depends on the jets flavour composition, the data driven HF fractions are used in this procedure when estimating r_{MC}. In Table 3.2 we can see all the scale factors used in the W+jets normalization. All the details are described in details in [53].

Single Top

Single top production represents, after the W+jets process, and because of its characteristic experimental signature, the largest background process to $t\bar{t}$ production.

Channel	Electron	Muon
1 jet	$0.972^{+0.262}_{-0.253}$	$0.998^{+0.220}_{-0.210}$
2 jets	0.883 ± 0.150	0.919 ± 0.092
3 jets	$0.799^{+0.160}_{-0.152}$	$0.832^{+0.133}_{-0.125}$
4 jets	0.823 ± 0.156	$0.899^{+0.142}_{-0.133}$
≥ 5 jets	$0.836^{+0.192}_{-0.184}$	$0.824^{+0.132}_{-0.148}$

Table 3.2: Scale factors for W+jets production in both the electron and muon channel for events with at least 1 jet tagged as b-jet.

Of all the possible channels of single top production, two are the ones that are particularly relevant to a $t\bar{t}$ analysis. The first is the Wt channel, so called because in the final state there is a real W boson and a top quark. The second is the t-channel, characterized by the process $q\ b \to q\prime t$ that proceeds via the exchange of a virtual W boson.

The final state for the Wt channel, depending on the decay modes of the W bosons can be characterized as semi-leptonic, di-leptonic and hadronic. Of course only the first two modes can give rise to compatible topologies of a $t\bar{t}$ semileptonic process (for the hadronic mode there would be no charged lepton as well as MET). Hence only these two contributions have been considered in the background estimation.

The MC samples have been generated using the AcerMc Monte Carlo program, for the hard process, and PYTHIA for the parton shower, the hadronization and the simulation of the underlying event. The CTEQ6M PDFs were used. The Wt sample has been normalized to the NLO level using a K-factor, while the t-channel has been generated using NLO matrix elements.

QCD Multijet

Another class of process where the signature is the same as $t\bar{t}$ production is the case in which many jets are generated and there is a misidentified isolated charged lepton (pions, etc). Even though the probability to misidentify a jet as an high-pt isolated lepton is low, the very high cross-section for QCD multijet production makes this process to contribute significantly to $t\bar{t}$.

The estimation of this background based only on Monte Carlo simulation is not very good, mainly because of the model in Geant4, which describes the *fake* leptons, is not very affordable. Therefore, even in this case a data-driven technique need to be used.

The technique used in this analysis is called simply "Matrix Method".

This method is based on selecting two cathegories of events, using the two opposed quality criteria in the lepton selection: loose and tight. The number of events which contain one loose lepton can be write as the sum of the events which contain a true lepton and the nuber of events which contain a fake lepton signal:

$$N^{loose} = N^{loose}_{real} + N^{loose}_{fake}. \tag{3.3}$$

Because of the higher quality of selecting criteria of the *tight* selection, we can take the ratio between loose an tight as an efficiency, and this efficiency will be different from real to fake leptons:

$$\epsilon_{real} = \frac{N^{tight}_{real}}{N^{loose}_{real}}. \tag{3.4}$$

So, we can write:

$$N^{tight} = \epsilon_{real} N^{loose}_{real} + \epsilon_{fake} N^{loose}_{fake}. \tag{3.5}$$

Now, the number of fake leptons passing the tight selections can be written as:

$$N^{tight}_{fake} = \frac{\epsilon_{fake}}{\epsilon_{real} - \epsilon_{fake}} \left(N^{loose} \epsilon_{real} - N^{tight} \right) \tag{3.6}$$

The effciency of real leptons is measured using Z boson production with the *Tag & Probe* method. The ϵ_{fake} factor is then measured in a special control region, where one knows that the contibution of fake leptons is significantly higher. This last estimate is different in the two lepton channels; details in next subsections.

QCD multijet in Muon channel - method A

In this channel we require a single, isolated muon, (see Section 3.8) in order to avoid muons coming from jets decay. But some muons, in fact non isolated, can pass our selection criteria.

To estimate ϵ_{fake} we take the W+jets like sample in the kinematic region where the transverse mass of the W boson candidate, $M_T(W)$ is less than 20 GeV, and the sum of the missing transverse energy and the transverse mass of the W boson less than 60 GeV. The loose selection will be the same as the tight one except for the isolation requirements, which are dropped. In addition, the small contribution due to true W and Z bosons decay is substracted basing on Monte Carlo simulations. More details on this can be found in [53].

QCD multijet in Muon channel - method B

Another method can be used to scale the QCD multijet background in the muon channel. This one lye on the characteristic that the major source of muons that can be misidentified as isolated comes from the decay of heavy flavour jets, and This kind of jets are characterized by an high impact parameter with respect to the primary vertex.

In this case, ϵ_{fake} is defined as the ratio between the events where the tight muon comes from decay with an impact parameter above a certain value, x, and the loose muon which have the same characteristic:

$$\epsilon_x = \frac{N^{tight}_{d_0>x}}{N^{loose}_{d_0>x}}. \tag{3.7}$$

More details on this can be found in [54]

This two methods give results consistely different ($\tilde{3}0\%$[53]), and ad-hoc studies does not show preference for one of the two methids. For that reason, we use the average over the fractions to normalize the multijet background.

QCD multijet in Electron channel

In the electron channel which has signficantly more misreconstructed jets the ϵ_{fake} is extimated by simply examining a sample where the missing transverse is required to be small (less than 20 GeV).

Z $(\rightarrow ll)$ and diboson + jets

Another source of background, although smaller than the previous ones, is represented by the Z+jets processes. One of the charged leptons coming from the decay of the Z boson could in fact pass the top trigger selection and the other lepton could escape detection, the net result being a fake event with an high-p_T lepton and missing transverse energy. However the strong cut on MET in the $t\bar{t}$ analysis strongly suppress this source of background events. The last source of electroweak background is the generation of two bosons (WW, ZZ or WZ) in association with a number of jets. However, this background is strongly suppressed too.

Another source of background comes from $t\bar{t}$ events themselves, in the fully hadronic channels. Moreover, $t\bar{t}$ events in which the W boson dacays into $\tau\nu_\tau$ are classified as signal if τ decay leptonically (35% of total), whereas if τ decay hadronically the event belongs to background.

3.3 Detector simulation

A parton-level event generator, as described in Chapter 2, by its own, it is of limited use to a high-energy physicist. To have a Monte Carlo simulation that is comparable to the real data, the partons produced by the event generator have to be transformed into hadrons and the interaction of the latter with the detector has to be fully implemented. Hadronization and detector simulation are hence essential to compare Monte Carlo predictions with real data.

In the ATLAS software framework there are two different programs of the detector simulation: the first, based on *Geant4* [44], performs a complete and detailed simulation of the detector, while a second program, called *Atlfast II*[45], compensates the high execution speed by a less precise description of the interaction of the particles with the detector. More precisely, *Atlfast II* only smears the kinematic of the MC particles according to the detector performance specification.

In this studies, because we want to use the best simulation of the detector, we have used the complete Geant4-based simulation of the ATLAS detector.

Fig. 3.1 shows how the simulated raw data, Raw Data Object (RDO), is produced from the generated Monte Carlo (*Truth*) events using the Geant4 program.

Geant4 is an Object Oriented set of libraries and utilities to develop Monte Carlo applications and simulate the interaction, transport and digitization of particles in matter. Detector geometry descriptions are stored in a database and retrieved by the simulation jobs. Geant4 creates a simulated detector in memory based on the description and then simulates the interaction of input particles with the detector. Material within the inner detector is particularly important as it affects subsequent tracking precision and calorimeter resolution. The simulation step creates Geant4 "hits" in the detector and may produce secondary particles which may also be reconstructed as separate objects by the reconstruction algorithms. Production of new particles during simulation is hence recorded onto the Truth record. Hits from pile-up may be added after the hard scattering process has been simulated and together, the detector hits are digitised to imitate the output from the detector. The package cointains in addition a visualization package, event display, and a software interface to simulate the electric signals that will be collected by the front-end electronics.

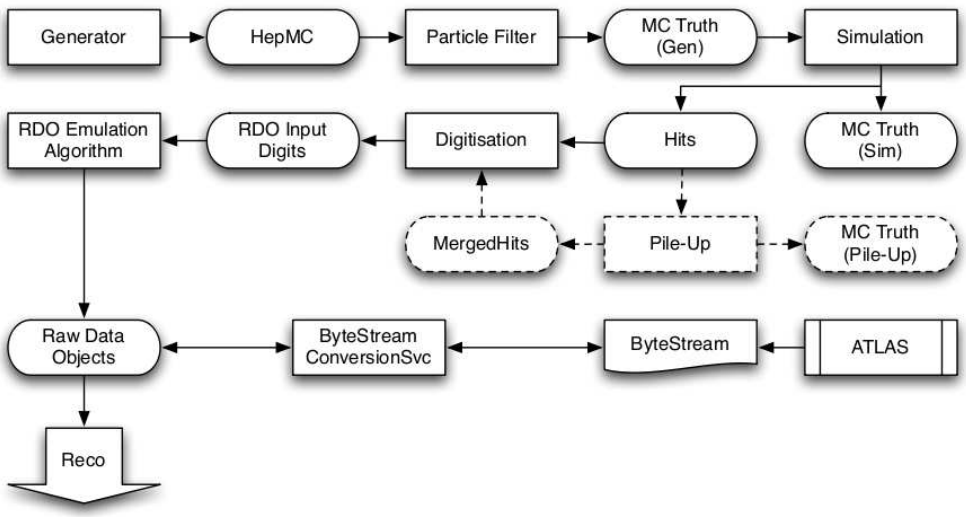

Figure 3.1: Schematic diagram showing the flow of MC data through simulation and digitisation process

3.4 Data Samples

The data used in this analysis where collected in 2011 with the ATLAS detector, and correspond to an integrated luminosity of approximately 4.7 fb^{-1}. In the year 2011, the LHC has changed the working conditions several times, expecially with increasing luminosity and, by consequence, pile-up events. In Fig. 3.2 we can see the cumulative luminosity for each day in 2011 as recorderd by ATLAS during stable beams state, while in Table 3.3 there are the details about the integrated luminosity for each period.

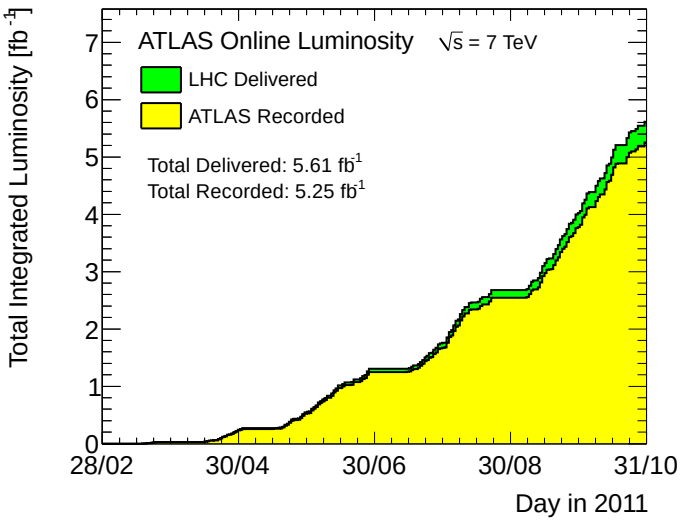

Figure 3.2: Cumulative luminosity versus day delivered to (green), and recorded by ATLAS (yellow) in 2011.

Period	Integrated Luminosity
B	$17\,pb^{-1}$
D	$179\,pb^{-1}$
E	$50\,pb^{-1}$
F	$152\,pb^{-1}$
G	$560\,pb^{-1}$
H	$278\,pb^{-1}$
I	$399\,pb^{-1}$
J	$232.9\,pb^{-1}$
K	$660.2\,pb^{-1}$
L	$1568\,pb^{-1}$
M	$1121\,pb^{-1}$

Table 3.3: Luminosity by data period for the 2011 data taking.

In our analysis, this changes led to a change in the trigger conditions, as described inSection 3.7.

3.5 Monte Carlo Samples

The Monte Carlo (MC) samples which have been used for the top quark analysis are described in this section. All MC samples comes from the MC11 production campain[46].

The calculation of many processes benefit from methods such as resummation of next-to-leading log terms and some are calculated at the full NLO accuracy. All the samples used have been normalized using "K-factors", to the NLO theoretical cross-section calculations whenever available. The value of $m_{top} = 172.5$ GeV has been used for the generation of all samples and all cross-sections correspond to this value. All samples were processed with the full Geand4 ATLAS detector simulation and reconstruction code.

All the MC samples refer to a center-of-mass energy of 7 TeV.

3.5.1 Simulation of $t\bar{t}$ signal events

Top quark pair production has been simulated using the Monte Carlo generator MC@NLO version 4.01. The hard process of $t\bar{t}$ production is calculated at NLO, so that diagrams that produce one additional parton in the final state are included at matrix element level. The parton density functions CT10[50] are used. Fragmentation and hadronisation are simulated using HERWIG (version 6.520) and the underlying event by JIMMY (version 4.31), both with the AUET2 tunes[47]. Those settings are extrapolated from the fits to the first 7 TeV LHC data.

The main $t\bar{t}$ samples used in the analysis are a sample of single and double leptonic events but do not contain fully hadronic events. There are no cuts applied at generation level other than the lepton flavour separation according to W-boson decay type that allowed subdividing the generated events into these two samples.

3.5.2 Simulation of background processes

A detailed descriptions of the main background processes affecting our analysis is described in detail in Section 3.2. Here we limit ourselves to describe the MC Event Generators, and their characteristics, used to generate these samples.

Simulation of single top events

For the single top quark signal production, the AcerMC matrix element generator was used in conjunction with PYTHIA, that was used for hadronisation, fragmentation and simulation of the underlying event. The parton density functions CTEQ6M have been used.

Simulation of W+jets , Z+jets and diboson plus jets

For the vector boson production, the ALPGEN generator has been used. It is a Monte Carlo event generator particularly indicated for the simulation of multi-partons hard-processes. The program has been interfaced to HERWIG for the simulation of the parton shower and hadronization, while the underlying event is simulated using JIMMY.

The Monte Carlo samples available for this process include, in addition to the bosons decaying into the three leptonic channels, a number of jets originating from the hard process that can go from zero to five, a value above which the production cross section becomes so small to be completely negligeable.

Because of the LO nature of this generator, a LO PDF is used (CTEQ6.1). The MLM[48] algorithm has been used to match the parton shower and the matrix element calculations.

Finally, double counting of heavy flavour quark production have been removed as described in [49].

In Table 3.4 are shown all the samples used for this analysis, as weel as the k factors applied to correct the total cross sections at the NLO level.

Data Sample	Generator	Dataset Number	Cross-Section (pb)	k-factor
$t\bar{t}$	MC@NLO	105200	79.01	1.146
single top	MC@NLO	108340	7.12	0.98
W+0 parton	Alpgen + Herwig,Jimmy	107680	6930.50	1.196
W+1 parton	Alpgen + Herwig,Jimmy	107681	1305.30	1.196
W+2 parton	Alpgen + Herwig,Jimmy	107682	378.13	1.196
W+3 parton	Alpgen + Herwig,Jimmy	107683	101.86	1.196
W+4 parton	Alpgen + Herwig,Jimmy	107584	25.68	1.196
W+5 parton	Alpgen + Herwig,Jimmy	107685	6.88	1.196
W+bb+0 NP	Alpgen + Herwig,Jimmy	107280	47.35	1.200
W+bb+1 NP	Alpgen + Herwig,Jimmy	107281	35.76	1.200
W+bb+2 NP	Alpgen + Herwig,Jimmy	107282	17.33	1.200
W+bb+3 NP	Alpgen + Herwig,Jimmy	107283	7.61	1.200
W+c+0j	Alpgen + Herwig,Jimmy	117293	644.4	1.200
W+c+1j	Alpgen + Herwig,Jimmy	117294	205.0	1.200
W+c+2j	Alpgen + Herwig,Jimmy	117295	50.8	1.200
W+c+3j	Alpgen + Herwig,Jimmy	117296	11.4	1.200
W+c+4j	Alpgen + Herwig,Jimmy	117297	2.8	1.200
W+cc+0j	Alpgen + Herwig,Jimmy	117284	127.5	1.200
W+cc+1j	Alpgen + Herwig,Jimmy	117285	104.7	1.200
W+cc+2j	Alpgen + Herwig,Jimmy	117286	52.1	1.200
W+cc+3j	Alpgen + Herwig,Jimmy	117287	16.9	1.200
Z+0 parton	Alpgen + Herwig,Jimmy	107650	668.7	1.25
Z+1 parton	Alpgen + Herwig,Jimmy	107651	134.8	1.25
Z+2 parton	Alpgen + Herwig,Jimmy	107652	40.3	1.25
Z+3 parton	Alpgen + Herwig,Jimmy	107653	11.2	1.25
Z+4 parton	Alpgen + Herwig,Jimmy	107554	2.5	1.25
Z+5 parton	Alpgen + Herwig,Jimmy	107655	0.77	1.25
Z+bb+0 parton	Alpgen + Herwig,Jimmy	109300	6.6	1.25
Z+bb+1 parton	Alpgen + Herwig,Jimmy	109301	2.5	1.25
Z+bb+2 parton	Alpgen + Herwig,Jimmy	109302	0.9	1.25
Z+bb+3 parton	Alpgen + Herwig,Jimmy	109303	0.4	1.25
WW+0 parton	Alpgen + Herwig,Jimmy	107100	2.1	1.26
WW+1 parton	Alpgen + Herwig,Jimmy	107101	1.0	1.26
WW+2 parton	Alpgen + Herwig,Jimmy	107102	0.5	1.26
WW+3 parton	Alpgen + Herwig,Jimmy	107103	0.18	1.26
WZ+0 parton	Alpgen + Herwig,Jimmy	107104	0.7	1.26
WZ+1 parton	Alpgen + Herwig,Jimmy	107105	0.4	1.26
WZ+2 parton	Alpgen + Herwig,Jimmy	107106	0.2	1.26
WZ+3 parton	Alpgen + Herwig,Jimmy	107107	0.1	1.26
ZZ+0 parton	Alpgen + Herwig,Jimmy	107108	0.5	1.26
ZZ+1 parton	Alpgen + Herwig,Jimmy	107109	0.2	1.26
ZZ+2 parton	Alpgen + Herwig,Jimmy	107110	0.09	1.26
ZZ+3 parton	Alpgen + Herwig,Jimmy	107111	0.03	1.26

Table 3.4: Summary table of Monte Carlo samples used. Shown: the name of the generator, the dataset number, the cross-section value, and the k-factor applied.

3.6 Objects Definitions

In this section we give the definition of the basic reconstructed objects - electrons, muons, jets and missing transverse energy - used throughout this analysis. The definitions used are based upon reconstruction algorithms standard in ATLAS and recommended by the combined performance groups.

3.6.1 Electrons

The reconstruction of electrons and photons starts from the EM calorimeter, using the so called sliding-window algorithm. This algorithm proceeds in three main steps: the tower building, the pre-cluster (seed) finding, and the cluster filling.

In the first step, the $\eta - \phi$ space of the calorimeter is divided into a grid of elements (each of size $\Delta\eta \times \Delta\phi$). Inside each of these elements, the energy of all cells across the longitudinal layers is summed into the tower energy.

In the pre-clustering step, a window of fixed $N_{\eta}^{window} \times N_{\phi}^{window}$ size is slided to each node of the tower grid defined above. If the window transverse energy (defined as the sum of the transverse energy of the towers contained in the window) at a given node is above a threshold, a pre-cluster is formed for this window. The size of the window and the threshold are optimised to obtain the best efficiency of the pre-cluster search and to limit the rate of fake pre-clusters due to noise. When all the pre-clusters are formed, one check for duplicates: if two pre-clusters have positions closer than a certain $\eta - \phi$ distance, only the one with the largest transverse energy is kept, and the other one is removed.

The positions of pre-clusters are used as seeds around which final clusters are subsequently filled. The EM cluster filling consists of including all cells that are located inside a rectangle centered on the seed position. The rectangular size is given in tower units $\Delta\eta \times \Delta\phi$.

At this point, for each of the reconstructed clusters, the reconstruction tries to find a matching track in the Inner Detector, within a $\eta - \phi$ window of 0.05×0.1 with momentum p compatible with the cluster energy E ($E/p < 10$), to check if the cluster is generated by a charged particle. If one is found, the reconstruction checks for presence of an associated conversion. An electron candidate is created if a matched track is found and no conversion is flagged, otherwise, the candidate is classified as a photon. Another check consist in distinguish electron from hadrons. This is done by looking at the TRT detector, where only the lightest particle leave signal.

The electron objects reconstructed with this algorithm described are electron candidates in the sense that there is still a chance that they are caused by another object than an electron, such as a jet or a charged pion. Accepting losses in the electron reconstruction efficiency one can apply certain cuts and methods in order to reduce such fake electrons.

In ATLAS there are three main standard categories for electron candidates. These are *loose++*, *medium++* and *tight++*, and the classification is done by a set of different cuts.

The "Loose++" set of cuts performs a simple electron identification based only on limited information from the calorimeters. Cuts are applied on the hadronic leakage and on shower-shape variables, derived from only the middle layer of the EM calorimeter (lateral shower shape and lateral shower width). This set of cuts provides excellent identification efficiency (88%[51]), but low background rejection.

The "medium++" set of cuts improves the quality by adding cuts on the strips in the first layer of the EM calorimeter and on other tracking variables, increasing the jet rejection by a factor of 3-4 with respect to the loose++ cuts, while reducing the identification efficiency to 77% .

The "tight++" set of cuts makes use of all the particle-identification tools currently available for electrons, leading to a fake rejection of 10^5, but the efficiency decreases down to 64%[51].

In our analysis, the *Tight++* criteria are used.

The geometrical acceptance is reduced in order to have informations by the Inner Detector, and to exlude the so-called *crack region*, which is the transition region between barrel end endcap calorimeters. So, we will consider electrons with η<2.47 and $1.37 \leq |\eta| \leq 1.52$, where η is the pseudo-rapidity of the corresponding cluster in the EM calorimeter.

In addition to this, we require other constraints:

- the angle difference between the cluster posistion in the second layer of the EM calorimeter and the ID track must be $\Delta\phi < 0.2$;
- electrons must be isolated: the electron candidate must be far (ΔR>0.2) from other ID tracks, and ΔR>0.3 from EM clusters;
- cluster energy over track momentum, $\frac{E}{p}$, has to satisfy η and E_T dependent constraints;
- the difference between the measured number of TRT hits and the expected ones is required to be less than 15;
- electrons matching converted photons are rejected;

At the end, to reduce the presence of electrons coming from quark decay, jets within ΔR=0.2 from the electorn are removed from the event. If after this overlap removal there is another jet within ΔR=0.4 and p_T>20 GeV, the electron is discarded.

Performance

Besides improving the quality of the electron reconstruction, the isolation cut is very effective in selecting those electrons that are coming from the W-boson decay while removing the electrons coming from the hadron decays within a hadronic jet. The latter electrons are expected to be characterized by electromagnetic clusters having on average a greater energy, because they are likely to be contaminated by the others nearby calorimeter energy deposits.

The electron reconstruction efficiencies are measured with the *Tag & Probe* method, using $Z \to e^+e^-$ samples. The scale factors, defined as $\epsilon_{data}/\epsilon_{MC}$ are delivered in 9 η bins.

The Tight++ scale factors are binned in 9 η bins with E_T-corrections in 6 E_T bins, as shown in Fig. 3.3. The main source of the systematic uncertainties comes from the background subtraction in data for both sample, and is much more in the endcap regions that in the barrel ones.

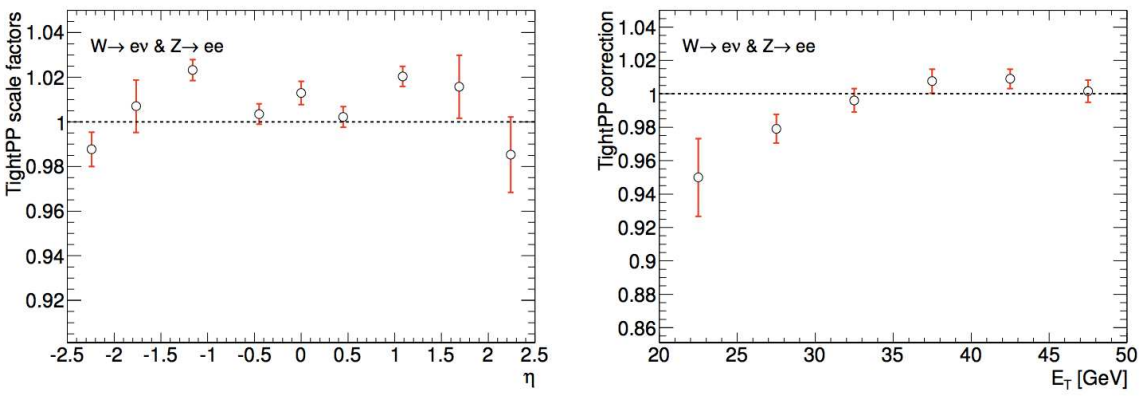

Figure 3.3: Electron $Tight++$ scale factors as function of η (left) and E_T-corrections (right). Data are from egamma combined performance group.

To get the correct energy scale, the *EnergyRescaler* tool, provided in *egammaAnalysisUtils*, is used. This is based on data taken for well known processes where isolated electrons ar produced ($Z \to ee$, $W \to e\nu$, etc).

In Fig. 3.4 we can see the reconstruction efficiency in MC and in the 2011 full dataset, as function of the recnstructed vertices.

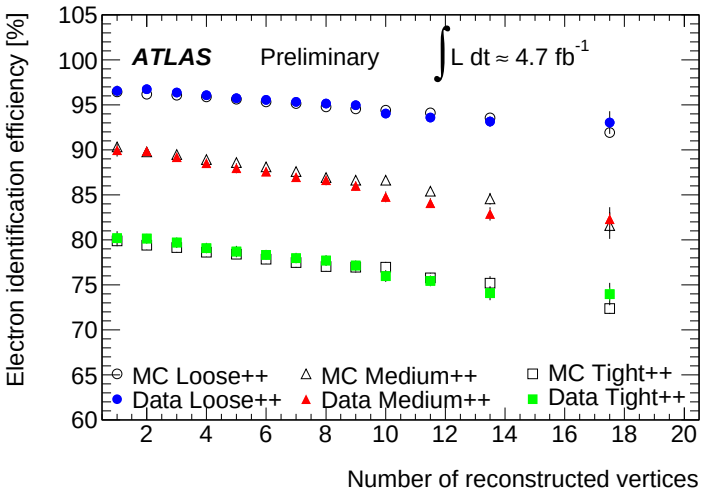

Figure 3.4: Efficiency on electron reconstruction versus pileup, for the three different electron definitions[52].

3.6.2 Muons

Muons leave their signatures in all of the detector subsystems including the inner detectors, the calorimeters and the muon spectrometer. Therefore, an optimal muon identification and measurement is obtained when information from each subsystem is fully incorporated into the reconstruction algorithm. Two prominent algorithms exists within ATHENA namely, *STACO* and *MuID*.

The general strategy of muon reconstruction is first to identify the muon track segments in the three stations of muon spectrometer, obtaining a so-called stand alone muon. The sub-algorithms that perform this task are MUONBOY for STACO and MOORE for MuID. This estrapolation have to take into account of the scattering and energy losses in the calorimeter: MUONBOY estimates the energy loss only using the information on the traversed material, while MOORE take into account in addition the measured energy of the calorimeter cells belonging to the muon candidates. These reconstruction sub-algorithms measure also the muons produced by light particles (π and K) that decay in the calorimeter. In order to identify the muons originating from the hard process the information just described have to be combined with tracking information from the inner detector, so defining what it is called a *combined muon* (see Fig. 3.5).

In this analysis, only muons reconstrucred from MuID algorithm are considered.

Matching is done by including additional parameters to account for the scattering within the calorimeter. Once matched, a global refit of ID/muon hits and calorimeter scatter is performed to obtain the optimum track parameters.

Another strategy of reconstruction rely on constructing muons starting from tracks coming from the Inner Detector. In MuID this algorithms are MuGirl and MuTagIMO. The first create a combined muon or a segment-tagged muon

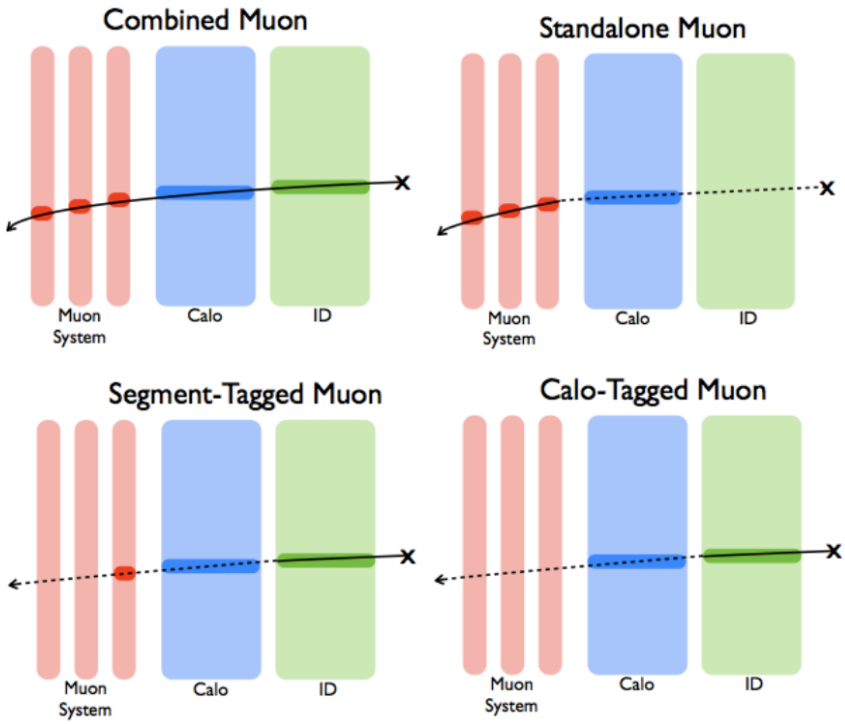

Figure 3.5: Schematic representation of muons reconstructions.

For a simpler quality classification of muon objects, a status word is used: *tight, medium and loose*, as we can see in Table 3.5.

Following the giudelines of Muon Combined Performance (MCP) group[55], and taking into account that all muons which comes directly from the top quark decay will pass all the detector, it will be natural to consider only combined muons, which are tight by definition. And this position will be used in the analysis.

Quality word	MuidCombined	MuidStandalone	MuGirl	MuTagIMO
TIGHT	yes	if $\|\|\eta\|\| > 2.5$	ext.track	-
MEDIUM	yes	yes	ext. track	-
LOOSE	yes	yes	yes	yes

Table 3.5: Muons quality definitions.

In addition to this, others quality criteria are used, as recommended by the MCP group:

- a pixel b-layer hit on the muon EXCEPT the extrapolated muon track passed an uninstrumented or dead area of the b-layer;
- number of pixel hits+number of crossed dead pixel sensors > 1;
- number of SCT hits+number of crossed dead SCT sensors > 5;
- number of pixel holes + number of SCT holes < 3;

Performance

In the muon reconstruction, the introduction of an isolation condition is particularly effective in separating the muons originating from the bosons decay from the ones coming from the decays of

hadrons in hadronic jets. Fig. 3.6(left), shows the number of reconstructed muons as a function of the transverse energy in a $\Delta R = 0.2$ cone (etcone20 or E_T^{20}) for two classes of reconstructed muons: a) muons coming from a Z-boson decay (red line histogram) and muons originating from an hadronic jet (green filled histogram). For the signal, the process $Z \to \mu\mu$ has been used, because of its very clear signature. In addition, a constraint on the invariant mass of the reconstructed di-muon system has been imposed: its difference from the very well known Z boson mass must be at maximum 15 GeV. From this plot, one can see that a cut at E_T^{20} <4 GeV is very effective in isolating prompt muons an rejecting most of the muons coming from hadronic jets. The data (black dots) confirm the goodness of the simulations.

Muons originated whithin jets can also have associated traks in the inner detector. For the same considerations of above, we will consider the sum of the transverse momentum of all the tracks whithin a radius of $\Delta R = 0.3$ around the muon, and this sum must be lower than 2.5 GeV (see Fig. 3.6(right)).

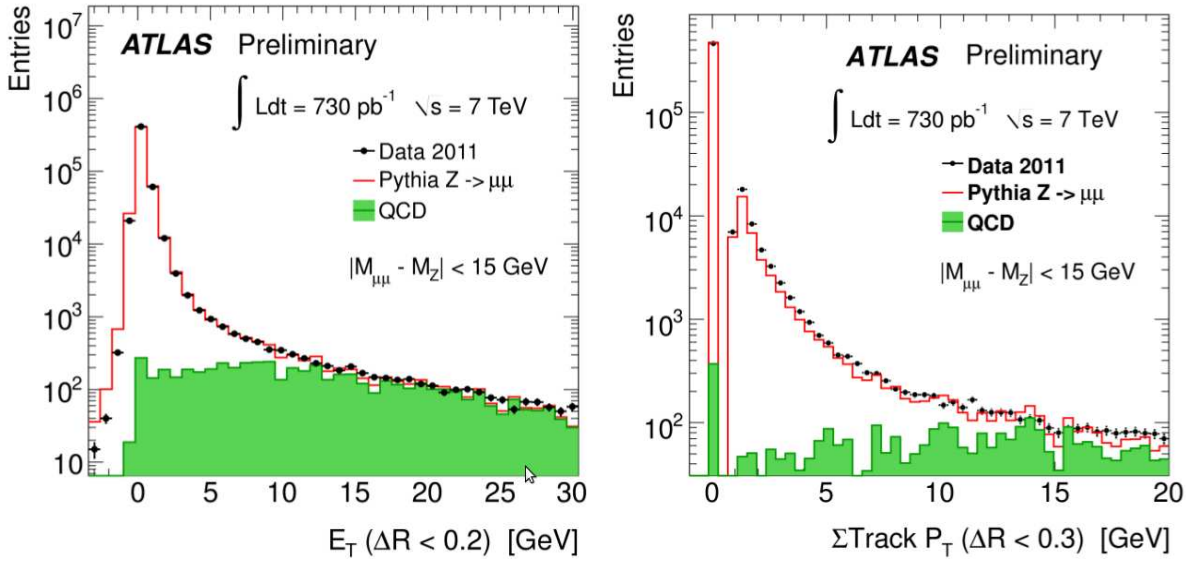

Figure 3.6: Left: The number of muons as a function of the transverse energy deposited within a cone of radius R=0.2 (etcone20) for two classes of reconstructed muons: a) muons coming from a Z-boson decay (red line histogram) and b) muons originating from an hadronic jet (green filed histogram). Right: same as left, but for the sum of the tracks in the Inner Detector.

This isolation cuts alone are no sufficient to exclude muons originated from the decay of heavy quarks, like the b quarks. One must introduce another cut. As we can see in Fig. 3.7, where we have plotted the distance from the muon to the nearest jet in events of top quark decay (red line) and b quark decay (red line), if we choose only muons far from jets (ΔR >0.4), our muons are more likely those needed in our selection.

As for the electron study, the fiducial region in η is restricted to the region $|\eta| < 2.5$, a range that is dictated by the acceptance of the inner detector and not of the muon chambers. Limiting the muon analysis to this η region is necessary also because we are interested in muons originating from the hard process and hence characterized by large transverse momenta. On a more technical side the muons we are selecting are those for which the information of the inner detector and muon spectrometer have been combined.

To study the performance of the muon reconstruction we need a well known physics event where the decay products are high energy isolated muons. The best envirоinment, as we already said, is the $Z \to \mu\mu$ events. In these events muons can be well separated by the background, by simply imposing the condition that the system of two muons of opposite charge should have the

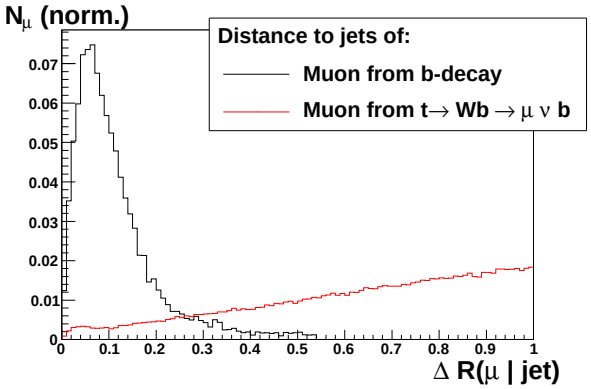

Figure 3.7: Muon-jets distance in muons coming from top decay (red line) and muons coming from b quark decay (black line).

invariant mass near the Z boson nominal mass.

In order to measure the reconstruction efficiency, the so-called *Tag & Probe* tecnique is used. In this technique, we search for one muon which fulfill all the selection requirements. When we found one, we look for an opposite charge muon, and the pair must have an invariant mass close to the one of the Z.

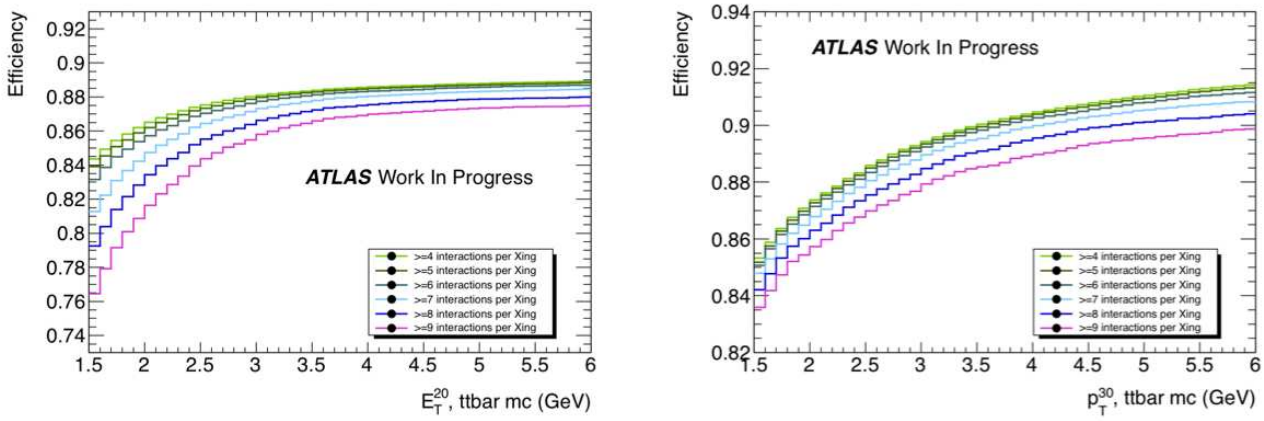

Figure 3.8: Muon efficiency of selections for $E_T^{0.2}$ and $p_T^{0.3}$ measured in $t\bar{t}$ MC. (a) Shows the efficiency for different $E_T^{0.2}$ selections with a selection of $p_T^{0.3}$ <2.5 GeV. (b) Shows the efficiency for different $p_T^{0.3}$ selections with a selection of $E_T^{0.2}$ <4.0 GeV[53].

At last, we require and additional isolation criteria: muons which are close to high-energy jets (according to the definition of Section 3.6.3), with |JVF|>0.75[1] within a cone of radius R=0.4, are removed. This helps in particular to remove muons from a b-quark in top decays. This is demonstrated in Fig. 3.7 which shows how, for muons coming from a W-boson decay, the distance is typically larger than ΔR =0.4, contrary to what happens for $b-$originated muons.

Muon Identification Scale Factors

The efficiency of the muon reconstruction is estimated by the MCP group and scale factors to correct the MC to match the data are provided in the *MuonEfficiencyCorrections package*. The efficiency of the additional isolation cuts also needs to be measured in the data. This is done

[1] JVF is the jet vertex fraction, a variable which exploits the fraction of tracks associated to the jet and coming from the primary vertex in order to suppress the effect of the in-time pile-up.

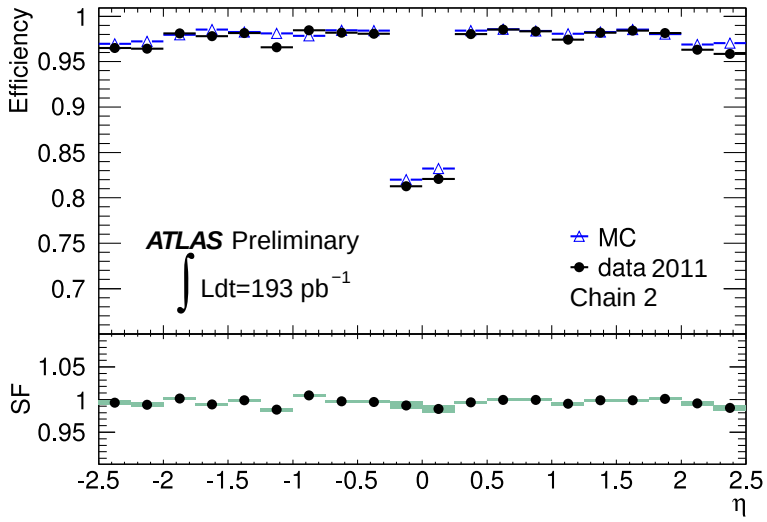

Figure 3.9: Muon reconstruction efficiency as a function of η.

using the tag-and-probe method in the Z data and MC events. The resulting scale factors are evaluated separately in the B-I, J-K and L-M data periods and are within 1% of unity. The scale factors are available in *TopMuonSFUtils*.

3.6.3 Hadronic Jets

While is relatively simple to reconstruct jets originated by particles well separated in angle, more difficult is to distinguish jets originated by partons emitted quasi-collinearly. In the worst case, these can be reconstruct as an unique jet, or some of the energy associated to one jet can be assigned to the other one.

Exist several algorithms for the reconstruction of jets, and the most relevants are implemented in ATHENA. This variety is needed because an "universal" algorithm does not exist, which is generally more efficient than the others, but the efficiency depends on the topology of the event that one want to study.

The design of a jet clustering algorithm is driven by several considerations, the following features are desirable and even necessary:

- **Infrared-safety:** in order to compare the experimental quantities with theoretical calculations the properties of the jets should not depend on the presence of arbitrary soft components;
- **collinear-safety:** the jet properties should not depend on any collinear radiation in the event;
- **collinear-factorizability:** the jet properties should not change replacing one component with a set of collinear components with the same total momentum;
- **Order independence**: The same hard scattering should be reconstructed independently at parton-, particle- or detector-level;
- **invariance** with respect to a generic boost in the longitudinal direction.

The main sub-detector for the reconstruction of the jets is the calorimeter. It is divided into cells, grouped in *clusters*, to suppress the noise.

Two methods are used at present to reconstruct jets: Calorimeter Tower (or "calo tower"), sums the cell energies in the projective towers in $\eta - \phi$ space of size $\Delta\eta \times \Delta\phi = 0.1 \times 0.1$.

Towers with negative energy (due to negative fluctuations from noise) are compensated by adding neighbouring towers with positive energy. The other method, Topological Cluster (or "topo cluster"), clusters cell deposits by selecting those with a significant signal. In particular, cells with a significance greater than 4 σ (σ being the standard deviation of fluctuation due to noise) are taken as seeds and the neighbouring cells with significance greater than 2 σ are clustered to form "energy blobs" with a three-dimensional topology.

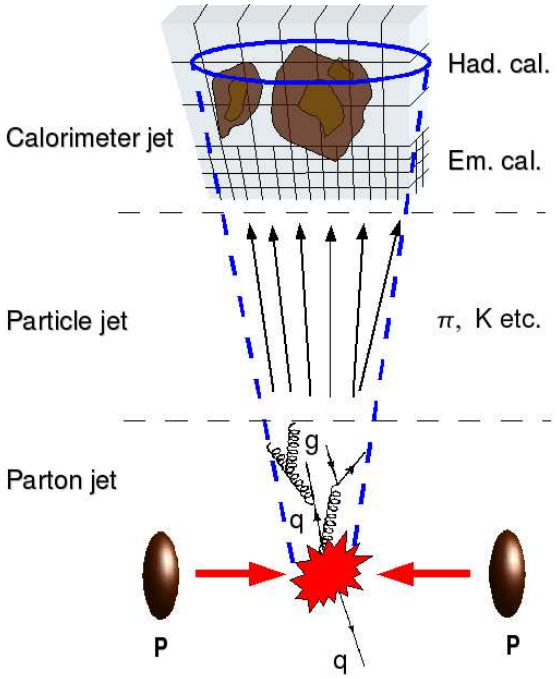

Figure 3.10: Schematic representation of the development and recostruction of an hadroic jet.

Cluster and towers are then associated to each other to find that who correspond to the same jet. The algorithms must account for the effects of the material behind the active medium (cables and support structures, other detectors, etc.) and for the different compositions of the calorimeter at different η regions. Moreover, in general the energy associated to a jet is not the same of that of the parent parton, because of the radiative and hadronization effects, and the influence of the underlying event.

The more simple algorithm of jet reconstruction is the *cone* algorithm. Basically, it groups toghether tracks and tower (or clusters) conteined within a cone in the $\eta - \phi$ space with a specific radius ΔR. This is a *seeded* algorithm: the jet reconstruction starts only if there is a cluster with an energy greater than a threshold. However, this algorthm is rarelu used.

The newer algorithms which are both collinear and infrared safe (IRC safe) are seedless too. The cone-like one is called SISCone[56] (Seedless Infrared Safe Cone).

A different jets reconstruction philosopy is used by the so-called sequential recombination jet algorithms. In this approach the objects (particles or pseudojets) are grouped in pairs to form new protojets. The idea is that protojets with nearly parallel momenta should be joined, so they will eventually form part of the same jet. The algorithm also determines when the joining should cease, based on a parameter R, analogous to the cone size parameter of the cone algorithms.

To group the proto-jets, one introduce distances d_{ij} between objects i and j:

$$d_{ij} = min(k_{ti}^{2p}, k_{tj}^{2p}) \frac{\Delta_{ij}^2}{R^2}, \tag{3.8}$$

where k_{ti} is the transverse momentum of particle i. In addition to the distance parameter R,

there is a parameter p to govern the relative power of the energy versus geometrical (Δ_{ij}) scales.

Varying this parameter we have different algorithms:

- $p = 1 \rightarrow k_t$ algorithm[57];
- $p = 0 \rightarrow$ Cambridge/Aachen algorithm[58];
- $p = 1 \rightarrow anti - k_t$ algorithm[59].

Theese three different configurations lead to very different algorithm characteristics. The Cambridge/Aachen algorithm, as an example, can take in account of the hierarchical substructure of the jet, and can be very useful in resolving boosted jets.

But the one of our interest, the anti-kt, is the more resilient to changhes from background immersion. As we can see in Fig. 3.11, where it is shown the transverse momentum difference between true jets (i.e. at generator level) and reconstructed ones (as seen by detector), the anti-kt has the minor spread.

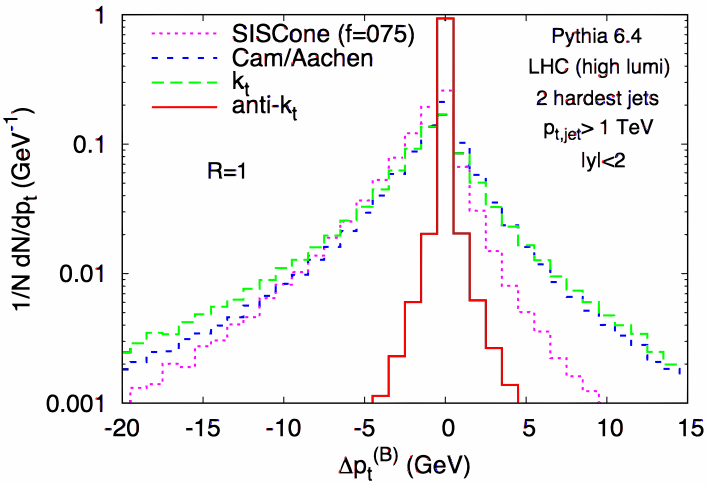

Figure 3.11: Jets algorithms resiliency: the anti-kt shows the minor contamination from background energy.

At this point, the energy of the jets must be calibrated for taking in account the pile-up and correction factors due to the detector (*JES*, Jet Energy Scale).

The substraction scheme for pile-up is applied at the EM scale. This correction is parametrized according to the number of primary vertices and the number of average interactions in a lumi-block, in bins of jet pseudorapidity[60].

Jets are then calibrated to the hadronic scale using correction factors coming from Monte Carlo simulations.

Bad jets, coming from beam-gas interaction, cosmic rays, hardware problems are removed.

Since electons are reconstructed as jets as well, the overlap between the two classes of objects is removed: only jets far ΔR>2 from electrons are accepted.

Jets considered in this analysis are required to have E_T >25 GeV and η<2.5. To select only jets coming from the hard scattering we impose a |JVF|<0.75.

Performance

The jet energy resolution (JER) measured with the di-jet balance and the bi-sector techniques in data and Monte Carlo agrees within uncertainty.

b-tagging

Jets originating from the hadronisation of b quarks can be tagged by exploiting the high mass and relatively long lifetime of B hadrons. This leads to decay tracks with large impact parameters with respect to the primary vertex, and a reconstructable secondary vertex. The average lifetime of the most commonly occurring B mesons such as B^+, B^0, B_S multiplied by the speed of light gives a length of the order 500 μm. With time dilation taken into account, a typical B meson produced in top decay would travel a distance of the order of 5 mm.

Several algorithms are built to tag the b-originated jets. In Fig. 3.12(Left) there is the rejection/efficiency correlation of the b-tagging algorithms of ATLAS. In this analysis a combination of three of them (JetFitter, IP3D, and SV1[61]) are combined. Their output, toghether with the kinematic, are evaluated by the so-called MV1-tagger, which is a neural network (TVMA) which determines a single discriminant variable, after selected the working point at 70% efficiency. The efficiency of the algorithm as function of the transverse momentum of the jet is in Fig. 3.12(Right)

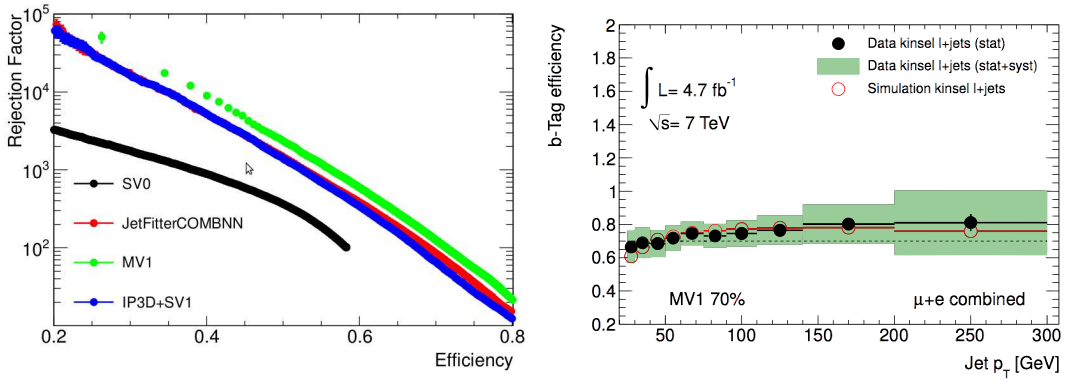

Figure 3.12: (Left) the rejection/efficiency correlation of the three different b tagging algorithms in ATLAST. (Right) The b-jet tagging efficiency estimated from data compared with the efficiency estimated from Monte Carlo simulations as function of the jet p_t[53].

While ideally the performance of the b-tagging algorithms depends only on the jet properties and is independent of any other specific event properties, this is unlikely to be true in reality. On the other hand, it is to be hoped that such dependencies are properly described in simulated data samples. Data/MC tagging and mistag efficiency scale factors relate efficiencies as determined in the various data samples to their counterparts in corresponding MC samples. The scale factors $k_{\epsilon_b}^{data/MC}$ and their uncertainties are used to achieve an optimal description of the data by Monte Carlo simulation by applying those p_T-dependent scale factors as event weight to them. Accordingly, they are the main result of the calibration and commonly defined as

$$k_{\epsilon_b}^{data/MC} = \frac{\epsilon_b^{data}}{\epsilon_b^{MC}} \tag{3.9}$$

where ϵ_b^{MC} is the fraction of b-flavoured jets which are tagged in simulated events, with the jet flavour defined by matching to generator level partons.

3.6.4 Missing Transverse Energy

As already observed a neutrino present in the final state, due to its very small weak interaction cross section, escapes detection. In this case, the only way to experimentally tag the presence of a neutrino is by measuring the Missing Transverse Energy (MET) determined by exploiting the unbalance in transverse momentum of the detected final state particles.

In the calculation of MET various contributions that are difficult to evaluate precisely has to be taken into account. Missing transverse energy from the muon system must be calculated separately and added to that from the calorimeter, as most of the muon energy would escape detection by the calorimeters. The raw calorimeter measurements cannot be used, since calibration must be applied and calibration depends on the kind of physics object that deposited the energy. Therefore, the final reconstructed MET is dependent on the algorithm used to reconstruct other objects in the event and it is not necessarily the case that the choice of algorithms used for MET calibration is the same as those used for the rest of the analysis. Nonetheless, in this analysis, "refined" MET calculated in the default reconstruction, *MET_RefFinal* was used. This consists of separate cell calibration based on physics objects including electrons, photons, and particle jets (based on topo cluster) as well as unused clusters and cells outside the cluster:

$$-E_{x,y}^{miss} = E_{x,y}^{RefElec} + E_{x,y}^{RefJet} + E_{x,y}^{RefMuon} + E_{x,y}^{CellOut} \tag{3.10}$$

The electron term uses electrons from the *ElectronAODCollection* satisfying the Tight++ definition with a $p_t > 10$ GeV where the electron energy scale used in the E_T^{miss} calculation includes all the electron correction factors except the out-of-cluster correction. Photons and τ objects are not included in the calculation. For the jets, there are two criteria: refined jets which are included into the E_T^{miss} at the EM+JES energy scale; and soft jets which are included at the EM scale. The refined jets are any jet in the *AntiKt4TopoEMJets* with a $p_T > 20$ GeV, while the jets between 7 GeV and 20 GeV are included as soft jets. The muon term in the E_T^{miss} is determined from the p_T of muons from the *MuidMuonCollection* for the full acceptance range of the muon spectrometers, $|\eta| < 2.7$. All combined muons within $|\eta| < 2.5$ are included in the E_T^{miss}. The muon term in the E_T^{miss} also contains isolated muons (MET_MU_TRACK) and non-isolated muons ($MET\_MU\_SPECTRO$). The MET_MU_TRACK requires the tracks to be isolated from all AntiKt4TopoEMJets (cone size=0.4) by ΔR=0.3, and includes the muon energy deposited in the calorimeter in the Cell Out term. For the $MET\_MU\_SPECTRO$ muons the energy deposited in the calorimeter is included in the jet term. Fig. 3.13(left) illustrates the E_T^{miss} composition in the e+jets and μ+jets channels.

For a detail explanation of the adopted algorithm in ATLAS we refer to[62].

To study the performance of the E_T^{miss} reconstruction one can isolate the $Z \to ll$ events, where no genuine $\not{E}_T$ is expected, apart from that coming from the semmileptonic decay of pileup events. In Fig. 3.13 there is the distribution of the $\not{E}_T$ of the full 2011 sample, compared with relative Monte Carlo samples. We can see that the Monte Carlo expectations are satisfied.

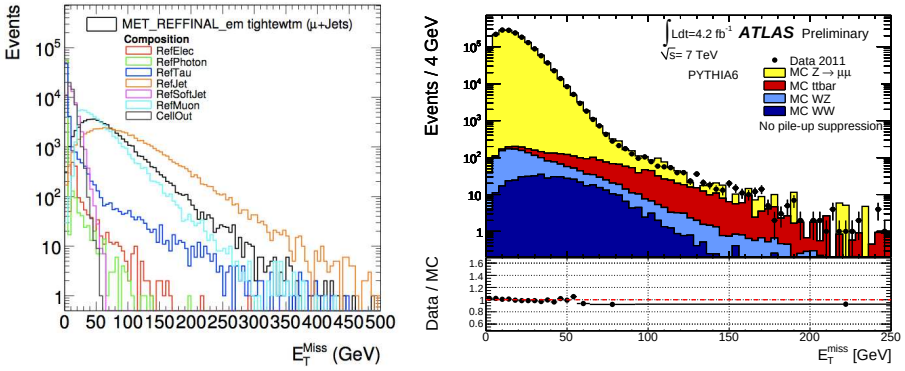

Figure 3.13: Composition of the E_T^{miss} in the muon channel (left) and comaprison data/montecarlo for $Z \to \mu\mu$.

3.7 Trigger

In this section, after having described the naming conventions of the ATLAS trigger slots we describe the electron and muon triggers and study their efficiencies.

3.7.1 Trigger slots naming conventions

Trigger items are described by a combination of letters and numbers. The trigger object is preceeded by a number representing the object multiplicity and followed by a number signifying the transverse momentum (p_T) of the trigger threshold. If an isolation requirement is applied, it is indicated by the letter 'i' after the p_T threshold. For example, the item name $2EM18I$ represents a trigger on two electromagnetic objects, with a threshold of 18 GeV each, including isolation requirements.

In the ATLAS trigger system there are three levels: the first level trigger (L1), very fast but not particularly accurate, the second level trigger (L2) and the final level trigger that is called Event Filter (EF). The L2 and EF trigger levels are often referred together as the High Level Trigger (HLT). The L2 and EF item naming conventions are the same as L1 except that lower-case letters are used. A trigger chain consists of the L1, L2, and EF trigger items.

3.7.2 Electron trigger

The L1 electron triggers operate on reduced granularity (0.1×0.1 in $\Delta\eta \times \Delta\phi$) calorimeter trigger towers which cover the range $|\eta| < 2.5$. A central cluster of four towers is formed in the electromagnetic and hadronic calorimeters, along with a ring of 12 towers around this central cluster. The ring is used to select candidates using isolation criteria (if needed) by cutting on the amount of energy deposited around the central cluster. At L2, electromagnetic clusters are formed, tracking is then performed for the first time, and, finally, the reconstructed cluster is matched to a track. In the final stage, the EF, tracking and cluster determination is performed with more accurate algorithms, further refining the trigger decision.

Because of different running conditions, we must use different triggers for different data taking periods. In our selection, we choose the "EF-e20-medium" trigger chain for periods from B to H, and "EF-e22-medium" for the I to M periods. Theese requires:

- an EM cluster at the L1, with E_T>14 GeV;
- a ID track match at L2;
- an EF electron with E_T>20 GeV (22 GeV in I-M data taking periods).

3.7.3 Muon trigger

The L1 muon trigger consists of fast electronics establishing coincidences between hits of different detector layers of the muon system inside programmed geometrical windows. The size of the window defines the transverse momentum interval corresponding to the deflection of the muon in the toroidal magnetic field. One of six programmable p_T thresholds is assigned to the candidate. The L2 processing consists of three reconstruction steps applied to full granularity data of the region defined by L1. First, the muon candidate is reconstructed in the muon spectrometer. Then inner detector tracks are reconstructed around the muon candidate. Both are combined to form the L2 muons upon which the trigger decision is based. Currently only the p_T of the muon candidate is checked. The muon reconstruction in the Event Filter is done using offline algorithms.

For the muon channel we choose the *EF-mu18* trigger chain. This requires the following prescriptions:

- a first trigger on L1-MU10;
- a combination at L2 with an Inner Detector track;
- at the EF the event must have a combined muon with the prescripted p_t.

3.8 Event selection

After having discussed the quality of the reconstruction of the various objects entering the analysis, the trigger requirements and the signal and background Monte Carlo samples, we can start our discussion of the adopted strategy to measure semileptonic $t\bar{t}$ events.

The events selected in the two channels must satisfy different conditions.

Muon channel event requirement

In the muon plus jets channel we require:

- one primary vertex with more than four tracks coming from it;
- one, and only one, good muon (following the prescriptions of Section 3.6.2);
- no good electrons in the event;
- the muon must match the trigger muon object;
- there must be no bad jet in the events.
- at least four jets following prescriptions of Section 3.6.3;
- missing transverse energy greater than 30 GeV;
- missing transverse energy plus the W boson transverse mass greater than 60 GeV;
- at least one jet tagged as b-jet.

We prefer to reject events with more than one good muon, and events with one good electron, to mantain ortoghonality with the dilepton channel analysis, where events are characterized by two good leptons (ee, $\mu\mu$, $e\mu$)

The bad jet flag is needed to rejet events where there can be contaminations from cosmics or beam gas interactions;

To calculate the leptonic W boson mass we use the kinematics of the muon and the missing transverse energy informations:

$$m_T^W = \sqrt{2p_T^l p_t^\nu (1 - cos(\phi^l - \phi^n u))} \tag{3.11}$$

In Fig. 3.14 we can see the distribution of the correlation between $\not\!\!E_T$ and m_T^W for generic QCD events and for $t\bar{t}$ events. As indicated by the black arrows, the cut at $\not\!\!E_t + m_T^W > 60$ GeV (already known as "triangular cut") is very useful to select mainly the events of semileptonic $t\bar{t}$.

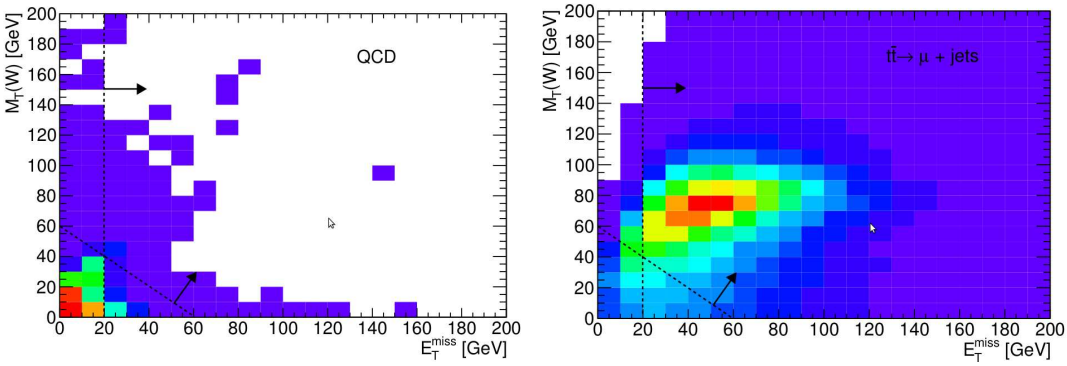

Figure 3.14: Correlation between $\not\!\!E_T$ and m_T^W in QCD events (left) and $t\bar{t}$ events (right). The cut at $E_t + m_T^W > 60$ GeV is also shown.

Electron channel event requirement

In the electron plus jets channel the requirements are similar to the previous one:

- one primary vertex with more than four tracks coming from it;
- one, and only one, good electron (following the prescriptions of Section 3.6.1);
- no good muons in the event;
- the electron must match the relative trigger object;
- there must be no bad jet in the events.
- at least four jets following prescriptions of Section 3.6.3;
- missing transverse energy greater than 30 GeV;
- W boson transverse mass greater than 30 GeV;
- at least one jet tagged as b-jet.

In this channel too we put a constraint in the tranverse mass of the W boson. As we can see in Fig. 3.15, a cut at 30 GeV it is effective in removing QCD background.

3.9 $t\bar{t}$ system reconstruction

In order to evaluate the kinematic variables of the top quarks, the full $t\bar{t}$ system needs to be reconstructed. For this porpouse, a kinematic fit is used that assesses the compatibility of the selected event with a typical top pair semi-leptonic decay, using a likelihood aproach.

This likelihood takes in account all the kinematic variables of the event: measured energies, pseudorapidities and azimuthal angles of the jets, the energy of the lepton and the missing transverse momentum.

If in our event more than four jets passes the selections, we take only the five with the greater p_T, and consider all the combinations of them.

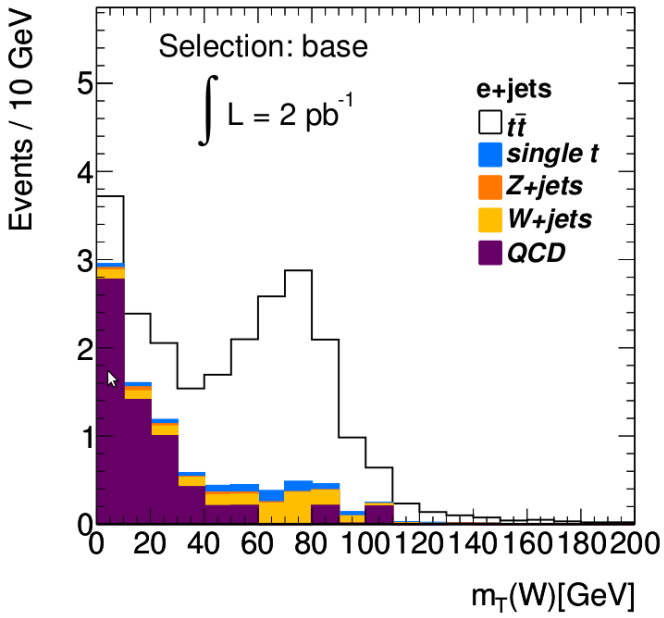

Figure 3.15: Distribution of m_T^W in the electron channel. We cut at 30 GeV.

Our likelihood is:

$$\begin{aligned} L \;=\; & \mathcal{B}(\tilde{E}_{p,1}, \tilde{E}_{p,2}|m_W, \Gamma_W) \cdot \mathcal{B}(\tilde{E}_{lep}, \tilde{E}_{\nu}|m_W, \Gamma_W) \\ & \cdot\mathcal{B}(\tilde{E}_{p,1}, \tilde{E}_{p,2}, \tilde{E}_{p,3}|m_t, \Gamma_t) \cdot \mathcal{B}(\tilde{E}_{lep}, \tilde{E}_{\nu}, \tilde{E}_{p,4}|m_y, \Gamma_t) \\ & \cdot\mathcal{W}(\hat{E}_x^{miss}|\tilde{p}_{x,\nu}) \cdot \mathcal{W}(\hat{E}_y^{miss}|\tilde{p}_{y,\nu}) \cdot (\hat{E}_{lep}|\tilde{E}_{lep}) \\ & \prod_{i=1}^{4} \mathcal{W}(\hat{E}_{jet,i}|\tilde{E}_{p,i}) \\ & \prod_{i=1}^{4} P(tagged|parton\ flavour) \end{aligned} \tag{3.12}$$

where:

- $\tilde{E}_{p,i}$ are the energies of partons associated to reconstructed jets' energy $\hat{E}_{jet,i}$;
- $\mathcal{W}$ are the transfer functions associating the reconstructed quantities, represented by $\hat{X}$, to quark and leptons produced at generator level ($\tilde{X}$). These transfer functions are derived from Monte Carlo simulations;
- $\mathcal{B}(\tilde{E}_{X,i}|m_Y, \Gamma_Y) = \frac{1}{((\sum \tilde{E}_{X,i})^2 - m_Y^2)^2 + m_Y^2\Gamma_Y^2}$, where m_Y and Γ_Y are the mass and the decay width of the particle Y as in PDG. These are the Breit-Wigner functions, evaluated using invariant masses of sums of appropriate parton and lepton four-vectors at the generator level;
- P(tagged|parton flavour) can be the b-tagging probability or the jet rejection efficiency, depending on the parton flavour, as obtained from Monte Carlo simulations.

The pole masses of the W boson and the top quark are fixed to m_W=80.4 GeV and m_t=172.5 GeV, while the width are Γ_W=2.1 GeV and Γ_t=1.5 GeV

This likelihood must be maximized with respect the energy of the partons, the energy of the charged lepton, and the component of the neutrino momentum.

In order to avoid badly reconstructed $t\bar{t}$ systems, a cut on the likelihood was applied: we reject all events where $log\mathcal{L}$<-52. In Fig. 3.16 we can see the likelihood distributions for the two channels: electron plus jets (upper side), and muon plus jets (down).

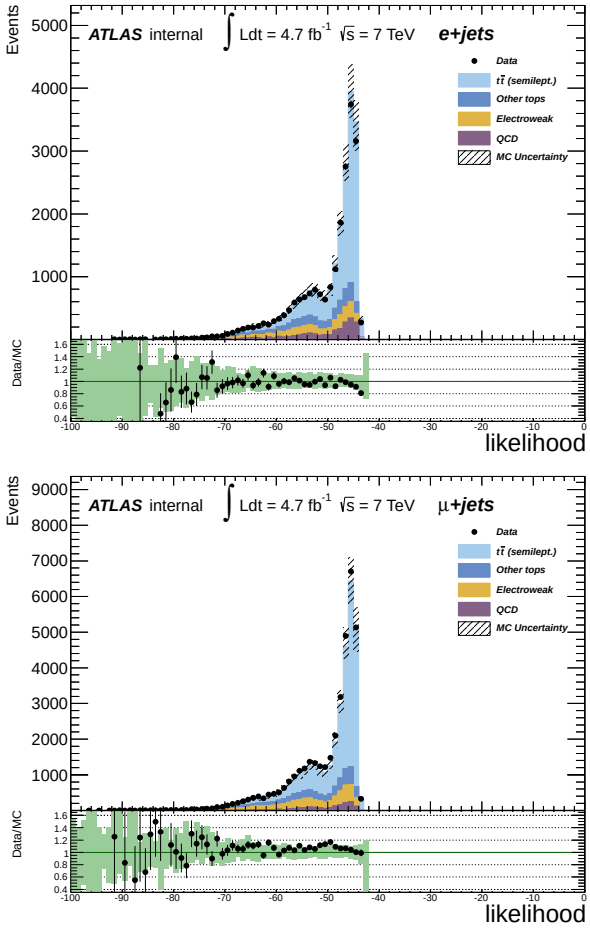

Figure 3.16: Distribution of (log $\mathcal{L}$) for electron channel (up) and muon channel (dowm).

3.10 Systematic uncertainties

Here we describe the major source of uncertainties which we need to take in account in our analisys.

We can classify the uncertainties into three main blocks:

- **signal modelling**, which are the systematics affecting the simulation of the hard-process, the parton shower and the PDF;
- **background modelling**, which are the systematics affecting our estimates made by the data-driven methods;
- **detector modelling**. In this block we group all the systematics due to our non-perfect understanding of the detecor.

3.10.1 Signal modelling

As we already said in the Chapter 2, there are systematics which affect our Monte Carlo prediction: the error on factorization and renormalization scales, which takes in account of the non calculated order of the perturbative series and the uncertainties on the non-perturbative parton distribution functions.

3.10.2 Detector modelling

Jet Energy Scale

The determination of the JES is a rather challenging task in the difficult environment of an hadron-hadron collider. While several methods are proposed such as using γ+jet events to propagate the electromagnetic scale to the hadronic scale, the jet energy scale depends on a variety of detector and physics effects. This includes non-linearities in the calorimeter response due, for example, to energy losses in dead material, hardware problems of the detector, and additional energy due to the underlying event and the pile-up. Energy lost outside the jet cone can also affect the measured jet energy. Effects due to the initial and final state radiation (ISR/FSR) modelling could also affect the jet energy scale but they are evaluated separately.

The uncertainty on the energy scale has been analyzed with the full 2011 dataset[53]. It takes into account several sources, like the effect of dead material, the know area where the calorimeters is affected by hardware problems, but also the effect of the different behaviour of jets with different energies.

All this lead the unertainty on JES to changhe with the transverse momentum of the jet, but also change from region to region of the calorimeter. In Fig. 3.17 there is an example of the p_T dependece of the JES for a fixed pseudorapidity value (η =0.5).

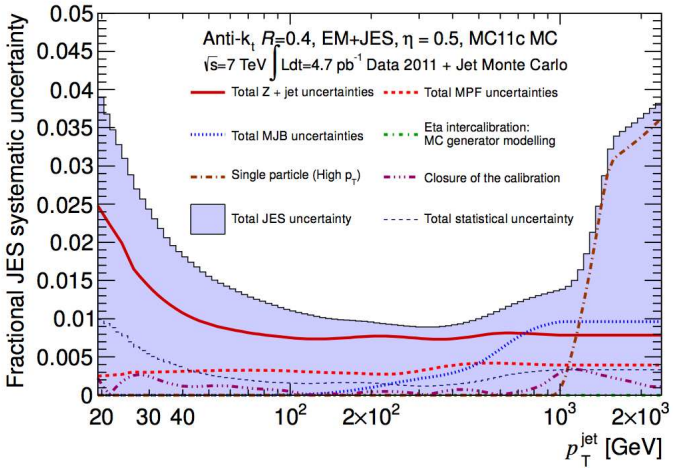

Figure 3.17: JES uncertainty for anti-k_t R=0.4 jets calibrated with the EM+JES scheme for the full 2011 dataset.

B-tag Scale factors

As already said in Section 3.6.3, the efficiency of the reconstruction algorithm varies with p_T (as we can see in Fig. 3.18) and η of the jet.

3.10.3 Backgound systematics

W+jets-background

Systematics related to the modelling of the W+jets normalization are of several sources. In general, the shape is taken from tree-level Alpgen simulation, with additional hard-parton processes included, matched to the partons generated by the parton shower using some cone radius, which is varied as one systematics source. After applying theory scale-factors (with their uncertainties) accounting for the NLO/LO total cross-section difference, data-driven scale factor is

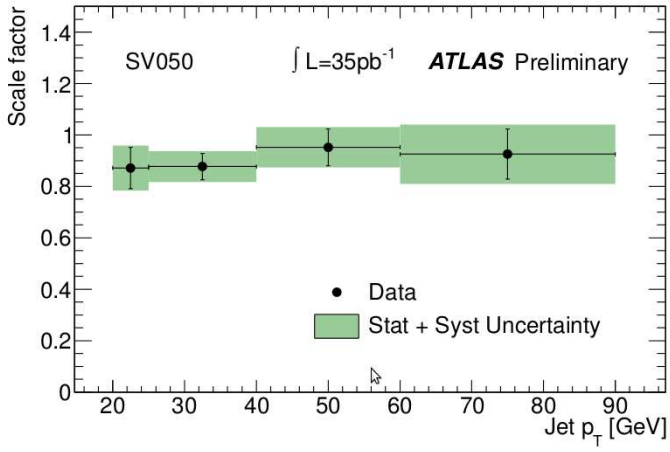

Figure 3.18: JES uncertainty for anti-k_t R=0.4 jets calibrated with the EM+JES scheme for the full 2011 dataset.

applied, based on the measurement of the charge asymmetry on the W+jet events. More details in Section 3.2.

QCD multijet background

The QCD multijet has been evaluated by loosening the lepton isolation and signal and fake efficiencies to pass the tight isolation criteria. This is discussed more in detail in Section 3.2. The two different methods To evaluate the uncertainty associated to the QCD multijet background, the normalization of this backgound component has been evalueted in varying by 20% and 50 %, for the muon and the electron respectly.

3.10.4 Luminosity uncertainty

The luminosity was measured from Van Der Meer scans. His uncertainty was estimated to be 3.7%. We add this uncertainty on all the differential cross sections.

3.11 Control Plots

In this section we show a number of control plots to demonstrate the validity of our selection of the events.

All the plots in this section, apart from the one on jet multiplicity, are obtained after applying all the cuts.

In the Jet multiplicity plot, shown in Fig. 3.19, we apply all the cuts except from the likelihood one. We want to show this plot, in because there is a general trend of our Monte Carlo to underestimate the events with an higher number of jets.

In principle, this discrepancy for larger multiplicity does not represent a problem, because these jets are excluded by our likelihood evaluation, as explained in Section 3.9.

The absence of data in the region with N_{jets} <4 is due to our cuts.

On the following plots we can identify the "electroweak" background as the sum of the backgrounds which include electroweak bosons: diboson production (WW, ZZ, WZ, see Section 3.5.2), W plus jets and Z plus jets. With the "other tops" label we mean the union between the single top background and the dileptonic channel of the $t\bar{t}$ production. With the light blue filled histograms we mean the production of the top pair which decay in the semileptonic channel, which is our case of interest.

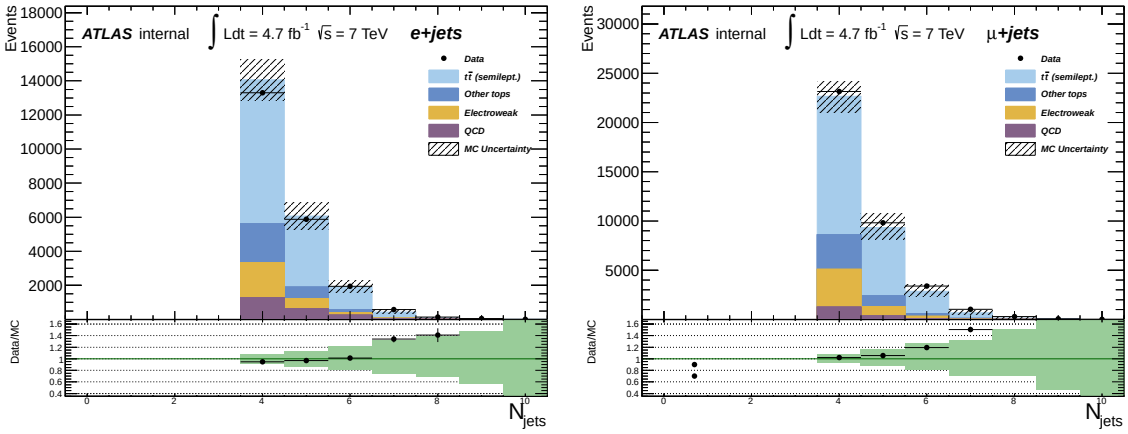

Figure 3.19: Jets multiplicity the electron channel (left) and muon channel (right).

The uncertainties of the Section 3.10 are shown as a shadowed area on top of the MC prediction.

In the Fig. 3.20 we can see the $p_T$spectrum of the charged lepton in the two channel. Apart from the first bin in the muon channel, which shows a small discrepancy to the predicted value, all the MC prediction in the various bins are in good agreement with the data within uncertainties.

However, we must observe that in the muon channel there is a general trend of our Monte Carlo to underestimate the data. The origin of this difference from electron to muon channel we have to leave for future studies.

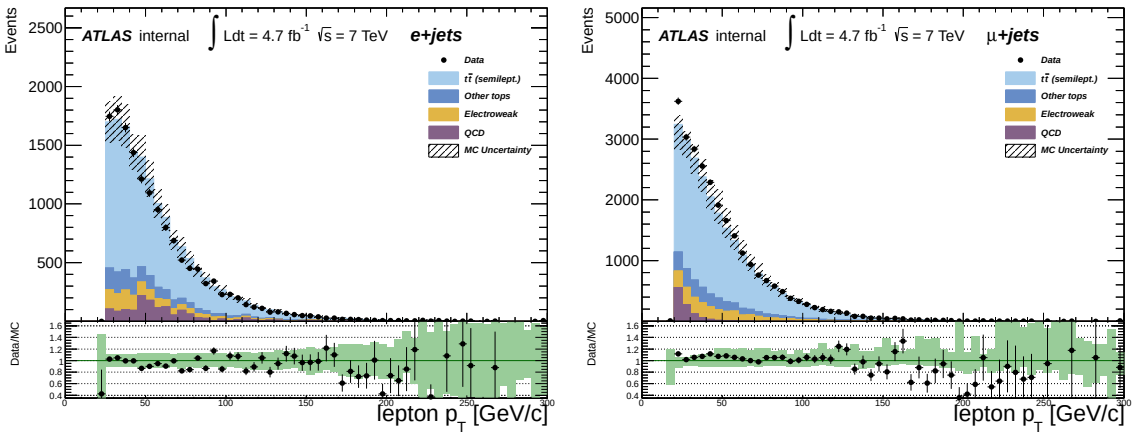

Figure 3.20: Transverse momentum of the charged lepton in the electron channel (left) and muon channel (right).

Also the measured charged lepton pseudorapidity spectrum, shown in Fig. 3.21, is well described by the Monte Carlo simulations, and in general is within the uncertainty we have evaluated.

A very important observable to evaluate is the transverse momentum associated to the neutrino, which escape our detection, as we already said. For this reason, it can be only reconstructed indirectly from the energy balance of all the subdetectors.

The distribution of the transverse energy, presented in Fig. 3.22, is well riproduced by the MC.

In the nexts figures (from Fig. 3.23 to Fig. 3.25) we will show the control plots of the distributions that we are going to use to measure the differential cross sections. The binning was chosen in order to minimize the bin to bin migrations and make the unfolding method more reliable.

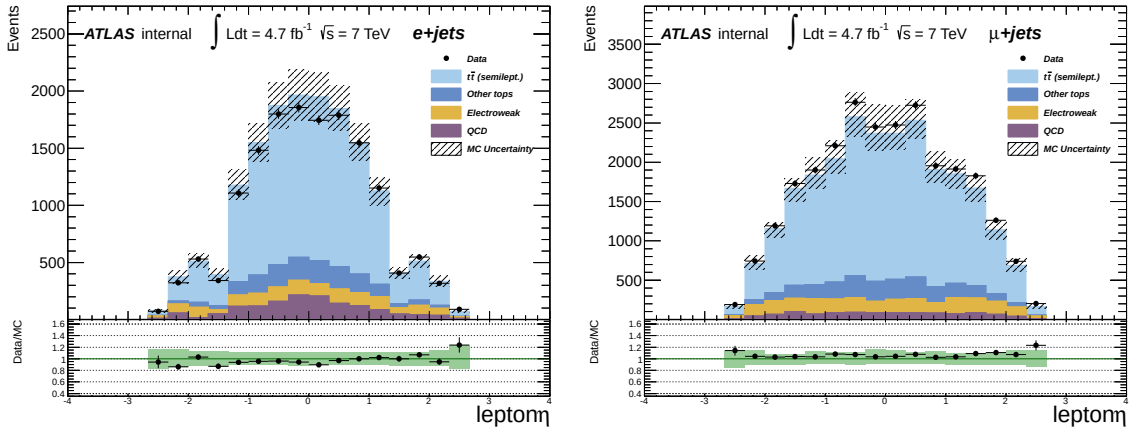

Figure 3.21: Pseudorapidity of the charged lepton in the electron channel (left) and muon channel (right).

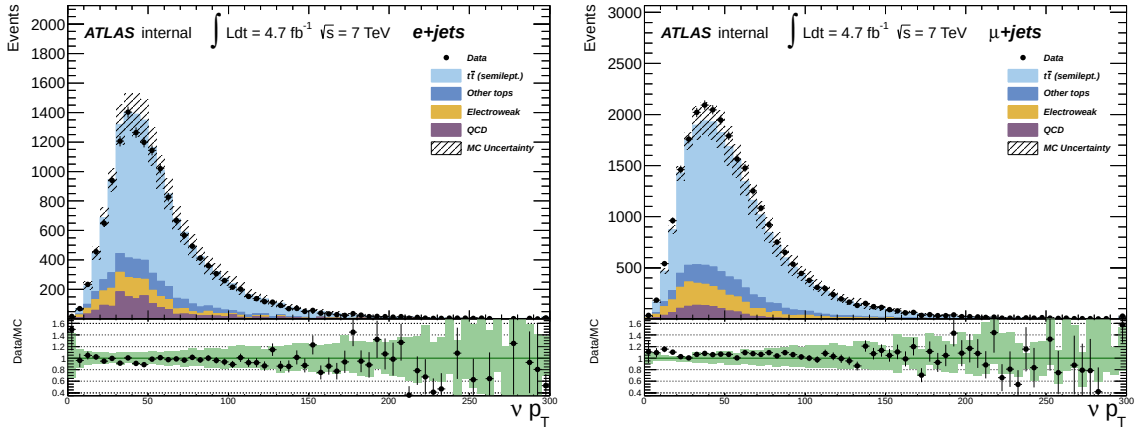

Figure 3.22: Transverse momentum associated to the neutrinos in the two channels.

For all the distributions the measurements are in good agreement with our MC predictions, at the level of the 10 % for both the channels. The different behaviour of the two channels is always visible.

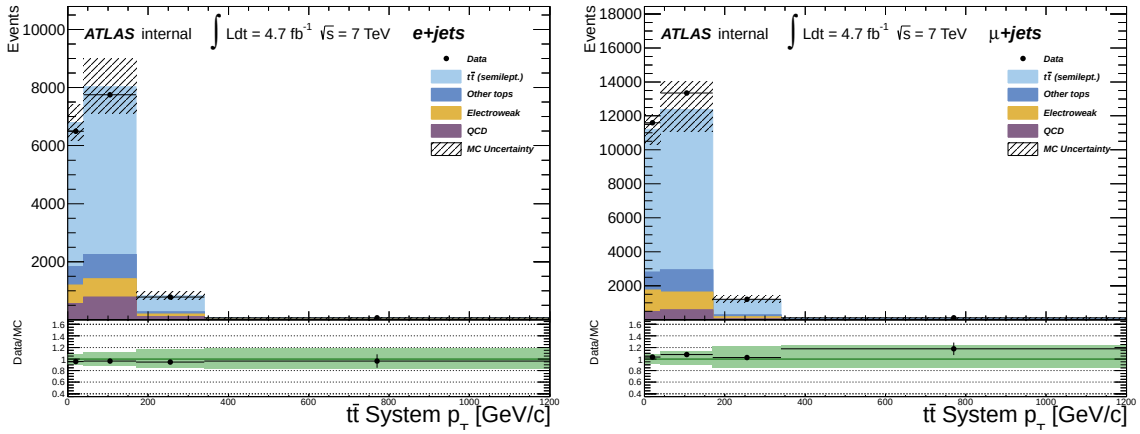

Figure 3.23: Transverse momentum of the $t\bar{t}$ pair.

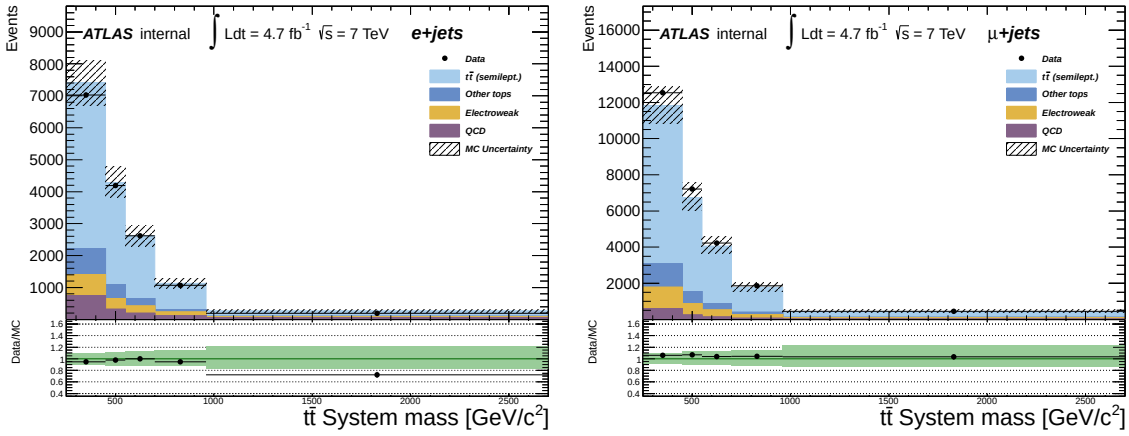

Figure 3.24: Invariant mass of the $t\bar{t}$ pair.

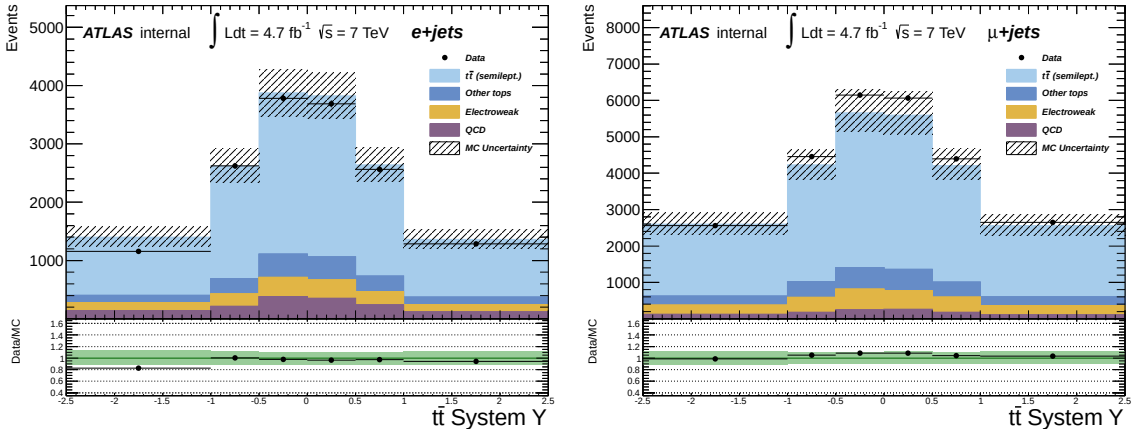

Figure 3.25: Rapidity of the $t\bar{t}$ pair.

3.12 Measurement of the total and differential $t\bar{t}$ cross section

In this final section we present our measurement of the $t\bar{t}$ total and the single differential cross sections $d\sigma/dp_T^{t\bar{t}}$, $d\sigma/dm^{t\bar{t}}$, and $d\sigma/dY^{t\bar{t}}$ for the electron and muon channels.

3.12.1 Total cross section

The total cross sections for the electron and muon channels is measured using the formula:

$$\sigma = \frac{N_{data} - N_{bkg}}{\epsilon \int Ldt}, \tag{3.13}$$

where N_{data} is the number of data events passing our final selections, N_{bkg} is the number of MC background events, ϵ is a factor that account for the acceptance and the efficiency of ATLAS detector, and $\int Ldt$ is the integrated luminosity of the full 2011 dataset.

The results for the electron channel is:

$$155.30 \pm 23.6pb \tag{3.14}$$

while for the muon channel is:

$$174.73 \pm 22.11pb, \tag{3.15}$$

to be compared with the NNLO prediction computed with the HATHOR fixed order program of:

$$\sigma_{tot}^{NNLO*}(m_t = 173.3GeV) = 163.1^{+12.9}_{-14.2}[scales] \pm 4.9[PDF]pb[75] \tag{3.16}$$

the theoretical prediction is in very good agreement with the total cross section for the electron channel. The result for the muon channel although comparable within the uncertainty, is larger than the electron channel result, as already observed.

3.12.2 Single differential $t\bar{t}$ cross sections

In order to measure the differential cross sections, one must observe that any measurements of physical observables is typically distorted or transformed from detector resolution and the limited geometric acceptance of the detector.

One approach is to generate events from a given theoretical prediction and process them through a detailed Monte Carlo process to model these effects in order to compare with experimental data. A general approach which allows direct comparison between theoretical calculations and experimental data is to unfold the experimental results accounting for resolution and acceptance affects.

In our analysis we have measured the differential cross section using two unfolding methods: a simple *bin-by-bin* cross section extraction method, and the Singular Value Decomposition (SVD) method for a better treatment of the migrations.

Bin by Bin method

The simplest method is to form the ratio of full simulation to the generator level distributions and to extract correction factors bin by bin.

The cross section for each bin i is given by the formula:

$$\sigma_i = \frac{N_{Data} - \Sigma_j N_{bkg,i,j}}{\epsilon_i * \int Ldt}, \tag{3.17}$$

where

$$\epsilon_i = \frac{MC_i^{ATLAS}}{MC_i^{truth}} \tag{3.18}$$

is the ratio between the events which have been digitized by Geant4 and which have passed all the selection of our analysis, and the truth events in the selected bin.

So, in this factor we include the kinematical acceptance of our selections and the detector efficiency.

In Fig. 3.26, Fig. 3.28, Fig. 3.27 these factors with the uncertainties are shown as a function of the transfer momentum, the rapidity and the invariant mass of the $t\bar{t}$ system.

On the top of the plots it is also shown the total efficiency of our selections.

As we can see in these plots, the efficiency of the electron plus jets channel is smaller than the muon one. This is due to our tighter selection on the electron sample, which we have performed in order to reduce background due to the pileup events.

In Fig. 3.29, Fig. 3.30 and Fig. 3.31 and in the Table 3.6, Table 3.7, Table 3.8 the single differential cross sections ($d\sigma/dp_T$) are shown. The measurements are compared with theory predictions calculated at the next-to-leading order with MCFM. The uncertainties on the theory predictions is only due to the factorization and renormalization scales.

The measured differential cross sections are in agreement with the theoretical predictions. It is to be remarked that the uncertainty of the theoretical predictions are much larger than the experimental uncertainties. Theoretical predictions at the next-to-next-to leading order for the

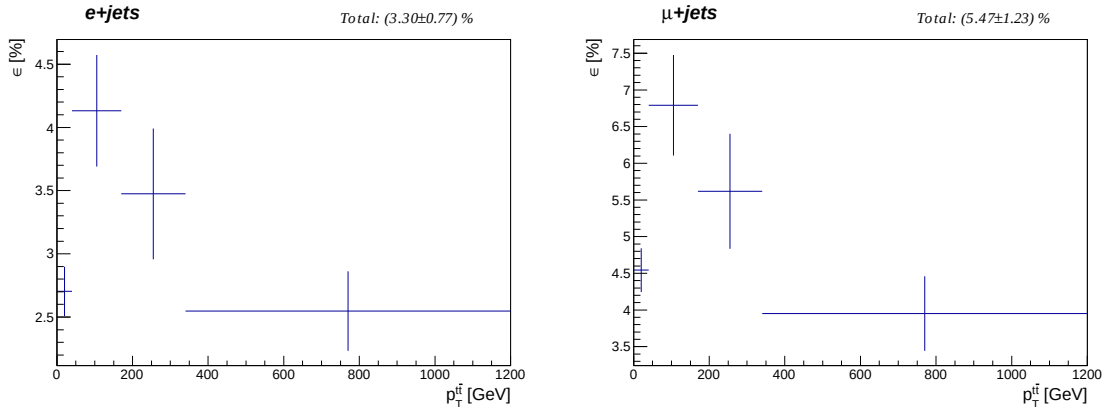

Figure 3.26: Transverse momentum spectrum of the acceptance in the electron and muon channels.

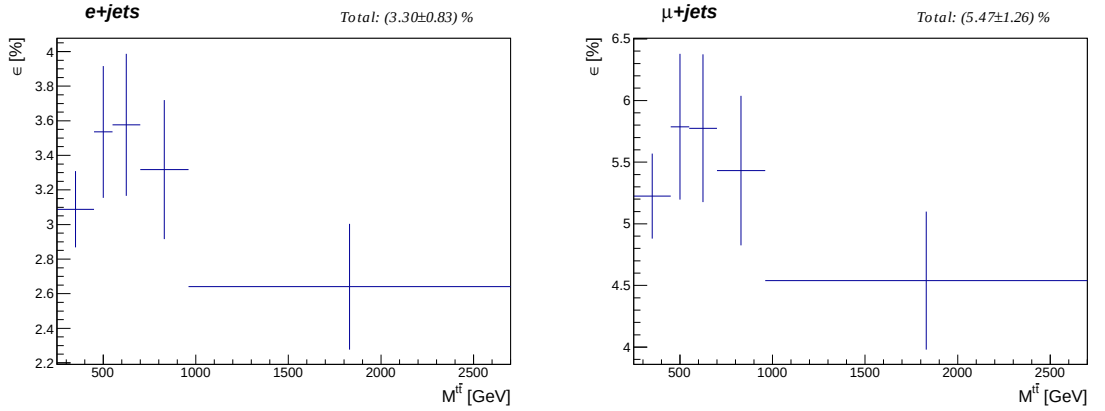

Figure 3.27: Mass spectrum of the acceptance in the electron and muon channels.

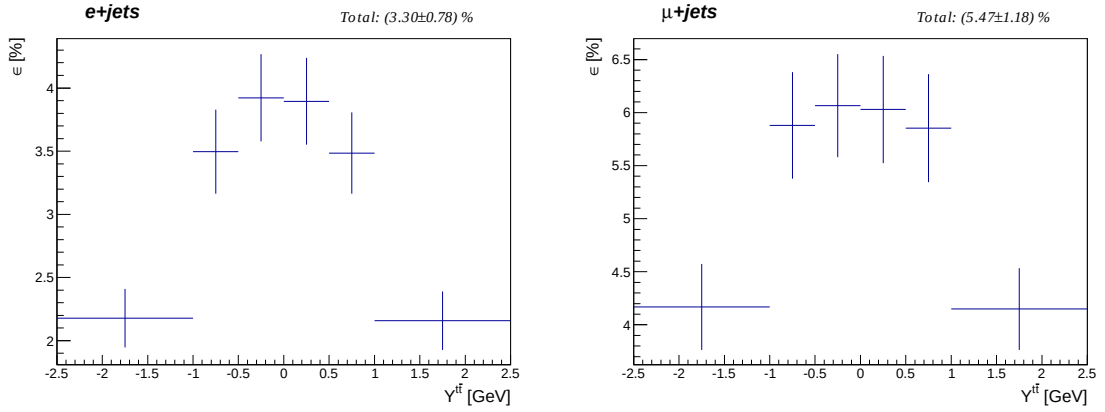

Figure 3.28: Rapidity spectrum of the acceptance in the electron and muon channels.

differential cross sections whould be extremely useful to perform a more stringent test to the QCD theoretical predictions.

One must specify that not all the known systematics are been taken in account, and so this is only an optimistic prediction.

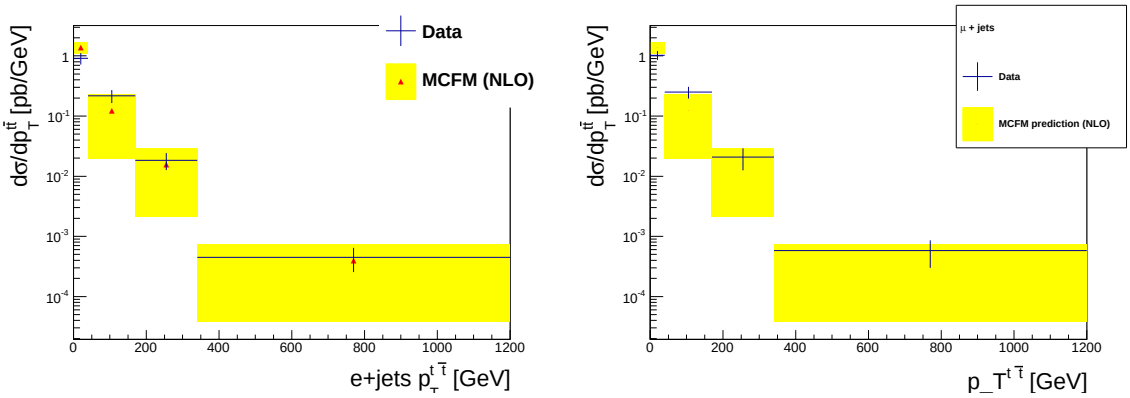

Figure 3.29: $p_T^{t\bar{t}}$ differential cross section with the Bin by Bin correction.

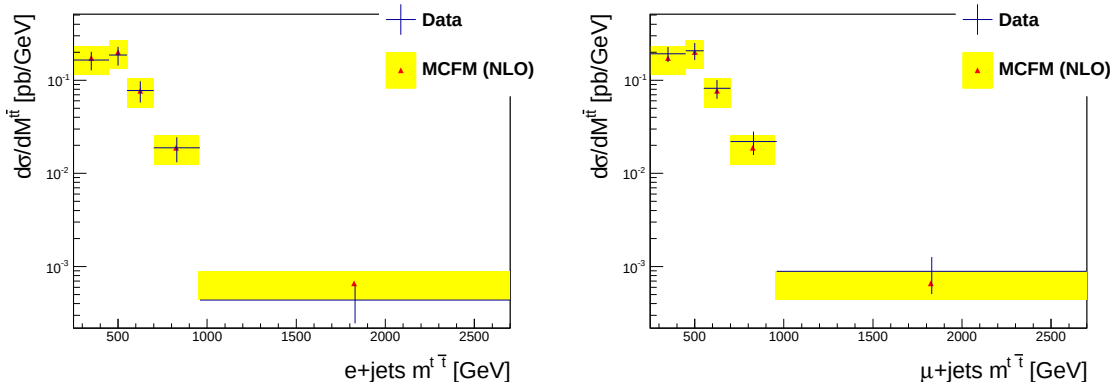

Figure 3.30: Mass spectrum of the acceptance in the two channels.

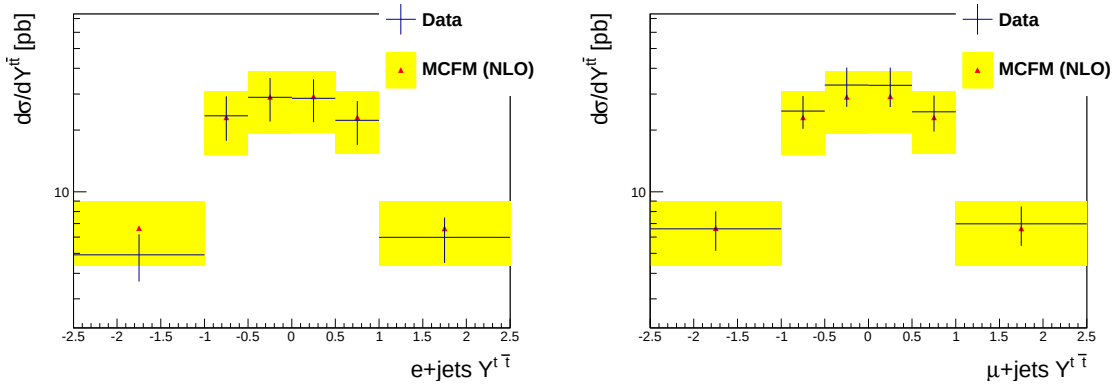

Figure 3.31: Rapidity spectrum of the acceptance in the two channels.

Nr bin	width	$\sigma_{central}^{e+jets}$	$\Delta\sigma^{e+jets}$	$\sigma_{central}^{\mu+jets}$	$\Delta\sigma^{\mu+jets}$	σ_{th}	$\Delta\sigma_{th}^{\mu+jets}$
1	40	9.17 $*10^{-1}$	1.97 $*10^{-1}$	1.03	1.74 $*10^{-1}$	1.38	2.99 $*10^{-1}$
2	130	2.18 $*10^{-1}$	5.31 $*10^{-2}$	2.50 $*10^{-1}$	5.56 $*10^{-2}$	1.22 $*10^{-1}$	1.03 $*10^{-1}$
3	170	1.84 $*10^{-2}$	5.79 $*10^{-3}$	2.07 $*10^{-2}$	8.26 $*10^{-3}$	1.57 $*10^{-2}$	1.35 $*10^{-2}$
4	860	4.49 $*10^{-4}$	1.95 $*10^{-4}$	5.79 $*10^{-4}$	2.80 $*10^{-4}$	3.95 $*10^{-4}$	3.56 $*10^{-4}$

Table 3.6: Cross sections values for the $t\bar{t}$ transverse momentum in the two channels.

Nr bin	width	$\sigma_{central}^{e+jets}$	$\Delta\sigma^{e+jets}$	$\sigma_{central}^{\mu+jets}$	$\Delta\sigma^{\mu+jets}$	σ_{th}	$\Delta\sigma_{th}^{\mu+jets}$
1	450	$1.65 *10^{-1}$	$3.71 *10^{-2}$	$1.92 *10^{-1}$	$3.49 *10^{-2}$	$1.73 *10^{-1}$	$5.78 *10^{-2}$
2	100	$1.86 *10^{-1}$	$4.25 *10^{-1}$	$2.08 *10^{-1}$	$4.33 *10^{-2}$	$2.01 *10^{-1}$	$7.71 *10^{-2}$
3	150	$7.77 *10^{-2}$	$1.99 *10^{-1}$	$8.20 *10^{-2}$	$1.87 *10^{-2}$	$7.71 *10^{-2}$	$2.72 *10^{-2}$
4	160	$1.88 *10^{-2}$	$5.62 *10^{-3}$	$2.19 *10^{-2}$	$6.22 *10^{-3}$	$1.88 *10^{-2}$	$6.62 *10^{-3}$
5	1740	$4.38 *10^{-4}$	$1.92 *10^{-4}$	$8.86 *10^{-4}$	$3.79 *10^{-4}$	$6.62 *10^{-4}$	$2.26 *10^{-4}$

Table 3.7: Cross sections values for the $t\bar{t}$ mass in the two channels.

Nr bin	width	$\sigma_{central}^{e+jets}$	$\Delta\sigma^{e+jets}$	$\sigma_{central}^{\mu+jets}$	$\Delta\sigma^{\mu+jets}$	σ_{th}	$\Delta\sigma_{th}^{\mu+jets}$
1	1.5	4.91	1.27	6.58	1.44	6.64	2.29
2	0.5	23.46	5.73	24.8	4.49	23.08	7.85
3	0.5	28.93	6.90	33.2	7.18	29.09	9.75
4	0.5	28.58	6.77	33.1	7.22	29.19	9.64
5	0.5	22.30	5.42	24.6	4.89	23.05	7.78
6	1.5	5.98	1.49	6.97	1.53	6.64	2.30

Table 3.8: Cross sections values for the $t\bar{t}$ rapidity in the two channels.

3.12.3 SVD unfolding method

The goal of this unfolding method is to use the so-called "migration matrix" of the spectra we want to unfold, to estimate the amount of data which migrate from neighboring bins, and then use this matrix in order to correct the data.

To obtain this matrix one simply relate event by event the true spectrum, i.e. the spectrum of the MC events without the Geant4 interaction/digitization, with the final one.

We can then write:

$$Ax = b \tag{3.19}$$

where $\hat{A}$ is the migration matrix, x is the vector which contains the real data, and b is the vector containing the observed data. The vectors' elements are the bins of our spectra.

In Fig. 3.32 there is an example of the migration matrices we used for the unfolding of the rapidity distributions. In an ideal case all the elements outside the diagonal should be zero (diagonal matrix), but in a real case some event can undergo a migration.

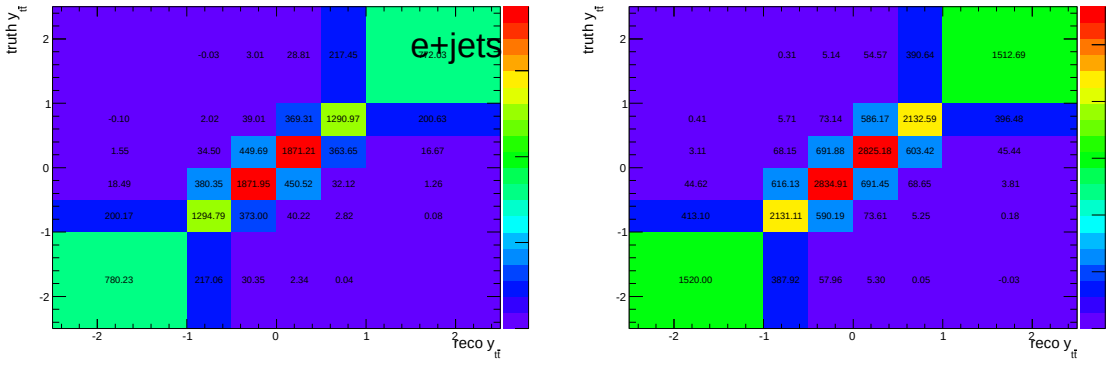

Figure 3.32: Migration matrices for the electron and muon channel for the rapidity spectrum.

If in principle one must only find the inverse of the $\hat{A}$ matrix, and apply this to the observed data, this is in pratical not convenient, expecially if we have large migrations in bins, because this will lead to unstable solutions against small variations in the initial system.

A method more stable is the SVD. The core of this method consists in transformation of the migration matrix into a new matrix which can be easily inverted.

The Singular Value Decomposition of the matrix A consist in rewriting the matrix in the form:

$$A = USV^T, \tag{3.20}$$

where U and V are orthogonal matrices, while S is a diagonal matrix with non-negative diagonal elements. These elements are called *singular values* of the matrix A.

With SVD, the linear system $Ax = b$ can be easily diagonalized by introducing rotated the vectors z and d:

$$USV^T = b \quad \rightarrow \quad z = V^T x, \; d = U^T b, \tag{3.21}$$

$$s_i z_i = d_i \quad \rightarrow \quad z_i = \frac{d_i}{s_i} \quad \rightarrow \quad x = Vz \; . \tag{3.22}$$

However, the determination of z_i can go wrong, mainly due to errors in b. For more detail on how to regolarize this solutions, see [74].

To obtain the inverted matrix , A^{-1}, now we can simply exploit the fact that the inverse of an orthogonal matrix is simply its transpose:

$$A^{-1} = VS^{-1}U^T. \tag{3.23}$$

Once we calculated this matrix, we apply it on the data, to retrive the unfolded spectra to insert in Eq. (3.17).

In Fig. 3.33, Fig. 3.34 and Fig. 3.35 and in the Table 3.9, Table 3.10, Table 3.11 the single differential cross sections ($d\sigma/dp_T$) are shown.

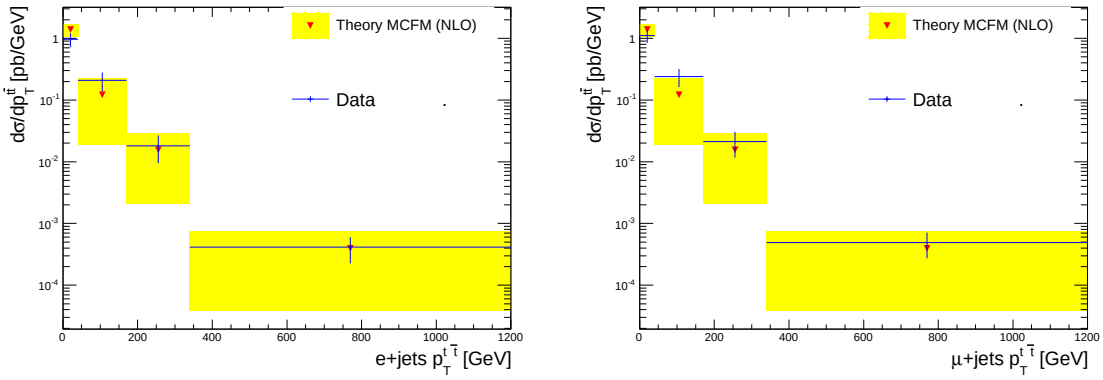

Figure 3.33: $d\sigma/dp_T^{t\bar{t}}$ differential cross section with the SVD unfolding.

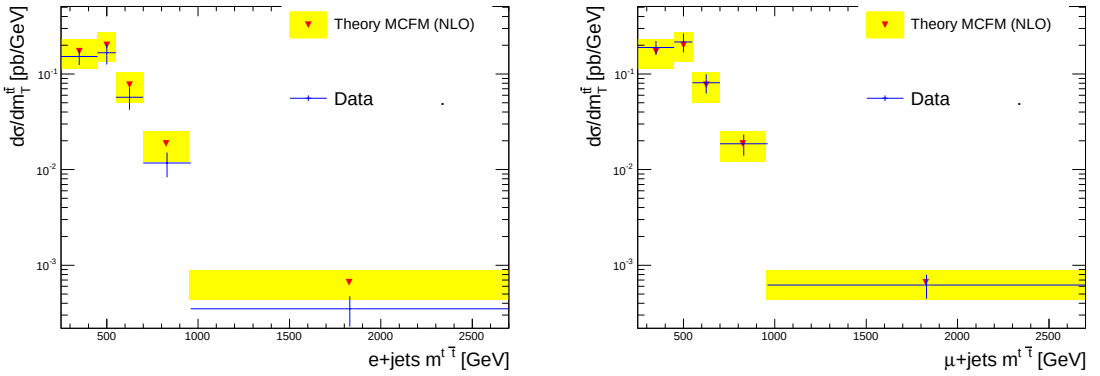

Figure 3.34: $d\sigma/dm^{t\bar{t}}$ differential cross section with the SVD unfolding.

Nr bin	width	$\sigma_{central}^{e+jets}$	$\Delta\sigma^{e+jets}$	$\sigma_{central}^{\mu+jets}$	$\Delta\sigma^{\mu+jets}$	σ_{th}	$\Delta\sigma_{th}^{\mu+jets}$
1	40	9.67 *10^{-1}	1.24 *10^{-1}	1.11	1.32 *10^{-1}	1.38	2.99 *10^{-1}
2	130	2.08 *10^{-1}	3.57 *10^{-2}	2.39 *10^{-1}	3.89 *10^{-2}	1.22 *10^{-1}	1.03 *10^{-1}
3	170	1.82 *10^{-2}	4.38 *10^{-3}	2.12 *10^{-2}	4.74 *10^{-3}	1.57 *10^{-2}	1.35 *10^{-2}
4	860	4.14 *10^{-4}	9.44 *10^{-5}	4.90 *10^{-4}	1.10 *10^{-4}	3.95 *10^{-4}	3.56 *10^{-4}

Table 3.9: Cross sections values for the $t\bar{t}$ transverse momentum in the two channels with SVD unfolding.

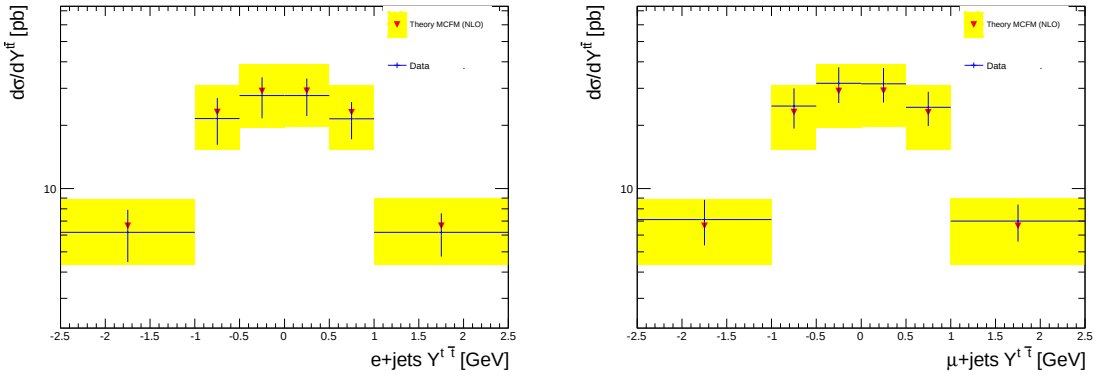

Figure 3.35: $d\sigma/dY^{t\bar{t}}$ differential cross section with the SVD unfolding.

Nr bin	width	$\sigma^{e+jets}_{central}$	$\Delta\sigma^{e+jets}$	$\sigma^{\mu+jets}_{central}$	$\Delta\sigma^{\mu+jets}$	σ_{th}	$\Delta\sigma^{\mu+jets}_{th}$
1	450	1.53 $*10^{-1}$	2.19 $*10^{-2}$	1.90 $*10^{-1}$	2.45 $*10^{-2}$	1.73 $*10^{-1}$	5.78 $*10^{-2}$
2	100	1.67 $*10^{-1}$	3.10 $*10^{-2}$	2.17 $*10^{-1}$	3.71 $*10^{-2}$	2.01 $*10^{-1}$	7.71 $*10^{-2}$
3	150	5.73 $*10^{-2}$	1.13 $*10^{-2}$	8.12 $*10^{-2}$	1.41 $*10^{-2}$	7.71 $*10^{-2}$	2.72 $*10^{-2}$
4	160	1.17 $*10^{-2}$	2.57 $*10^{-3}$	1.87 $*10^{-2}$	3.54 $*10^{-3}$	1.88 $*10^{-2}$	6.62 $*10^{-3}$
5	1740	3.50 $*10^{-4}$	9.14 $*10^{-5}$	6.20 $*10^{-4}$	1.33$*10^{-4}$	6.62 $*10^{-4}$	2.26 $*10^{-4}$

Table 3.10: Cross sections values for the $t\bar{t}$ mass in the two channels with SVD unfolding.

Nr bin	width	$\sigma^{e+jets}_{central}$	$\Delta\sigma^{e+jets}$	$\sigma^{\mu+jets}_{central}$	$\Delta\sigma^{\mu+jets}$	σ_{th}	$\Delta\sigma^{\mu+jets}_{th}$
1	1.5	6.19	1.30	7.11	1.31	6.64	2.29
2	0.5	21.51	4.07	24.64	4.05	23.08	7.85
3	0.5	27.69	4.63	31.61	4.66	29.09	9.75
4	0.5	27.70	4.27	31.50	4.49	29.19	9.64
5	0.5	21.47	3.30	24.32	3.44	23.05	7.78
6	1.5	6.18	1.09	6.99	1.06	6.64	2.30

Table 3.11: Cross sections values for the $t\bar{t}$ rapidity in the two channels with SVD unfolding.

Conclusions

In the Fall of 2009, the Large Hadron Collider started to be operational, providing the ATLAS and CMS experiments with the first data samples at the center of mass energy of 7 TeV. Using the p-p collisions provided by the machine in the year 2011, and thanks to the large cross section for $t\bar{t}$ pair production, a large amount of top-antitop pairs has been produced amounting to an integrated luminosity of 4.7 fb^{-1}.

The production of $t\bar{t}$ pair in p-p collisions is an extremely important process to be studied. On the theoretical side the measurements of the cross sections for the process $pp \to t\bar{t}$ allow very stringent tests of the predictions of perturbative QCD to be performed as well as to study the properties of the top quark with great precision. On the experimental side, the study of this particular process is an important testing ground of the performance and calibration of the ATLAS detector; being necessary, for this analysis, to identify and reconstruct isolated leptons, hadronic jets and missing transverse energy, that are the most important experimental objects to be found in the majority of the LHC analyses.

In this thesis using the most up-to-date simulation of the ATLAS detector response, and signal and background Monte Carlo samples, we have studied the possibility to reconstruct $t\bar{t}$ events decaying in the semileptonic channel. In the third chapter we have shown that an effective event selection strategy can be implemented to determine a clean sample of $t\bar{t}$ events then used for the measurements of the total $t\bar{t}$ cross section and the single differential cross sections for $t\bar{t}$ production as a function of the transvers momentum, mass and rapidity of the $t\bar{t}$ system ($d\sigma/dp_T^{t\bar{t}}$, $d\sigma/dm^{t\bar{t}}$, $d\sigma/dY^{t\bar{t}}$). These measurements are all in very good agreement with the latest theoretical predictions.

Bibliography

[1] L. Evans and P. Bryant, *LHC Machine* JINST 3 S08001, 2008

K. Aamodt et al, *The ALICE experiment at the CERN LHC* JINST 3 S08002, 2008

G. Aad et al, *The ATLAS Experiment at the CERN Large Hadron Collider* JINST 3 S08003, 2008

S. Chatrchyan et al., *The CMS experiment at the CERN LHC* JINST 3 S08004, 2008

A. Augusto et al, *The LHCb Detector at the LHC* JINST 3 S08005, 2008

G. Anelli et al. *The TOTEM Experiment at the CERN Large Hadron Collider* JINST 3 S08007, 2008

[2] G. Aad et al, *The ATLAS Experiment at the CERN Large Hadron Collider, chapter 2* JINST 3 S08003, 2008

[3] G. Aad et al, *The ATLAS Experiment at the CERN Large Hadron Collider, chapter 4* JINST 3 S08003, 2008

[4] G. Aad et al, *The ATLAS Experiment at the CERN Large Hadron Collider, chapter 6* JINST 3 S08003, 2008

[5] G. Aad et al, *The ATLAS Experiment at the CERN Large Hadron Collider, chapter 8* JINST 3 S08003, 2008

[6] ATLAS Collaboration. Atlas computing technical design report. Technical Design Report CERN/LHCC/05-22, CERN, 2005.

[7] M. Aderholz et al. Monarc phase 2 report. Technical Design Report CERN/LCB/00-01, CERN, 2000.

[8] The ATLAS Collaboration, *Reconstruction and Calibration of Missing Transverse Energy and Performance in Z and W events in ATLAS Proton-Proton Collisions at* $\sqrt{(s)} = 7$ *TeV*, ATLAS-CONF-2012-101

[9] P. M. Nadolsky et al., Phys. Rev. D 78, 074005 (2008).

[10] D. J. Gross and F. Wilczek, Asymptotically free gauge theories Phys. Rev., D 8 3633 (1973)

H. D. Politzer, Asymptotic freedom: An approach to strong interactions Phys. Rev. Lett., 14 129 (1974)

[11] P.W. Higgs, Phys. Lett. 12, 132 (1964)

[12] S. L. Glashow, Partial symmetries of weak interactions Nucl. Phys. 22 (1961)

A. Salam and J. C. Ward, Electromagnetic and weak interactions Phys. Lett., 13 (1964)

S. Weinberg, A model of leptons Phys. Rev. Lett., 19 1264 (1967)

[13] N. Cabibbo, Phys. Rev. Lett. 10. 531 (1963)

[14] M. Kobayashi, T. Maskawa, Prog. Theor. Phys. 49, 652 (1973)

[15] F. Abe et al. [CDF Collaboration], Phys. Rev. Lett. 74 (1995) 2626

S. Abachi et al. [D0 Collaboration], Phys. Rev. Lett. 74 (1995) 2632

[16] M. C. Smith and S. S. Willenbrock, Phys. Rev. Lett. 79 (1997) 3825

[17] K. Melnikov and T. v. Ritbergen, Phys. Lett. B 482 (2000) 99

[18] C. Amsler et al. (Particle Data Group), Phys. Lett. **B667**, 1 (2008)

[19] J. Alcaraz et al. [LEP Collaborations], "Precision Electroweak Measurements and Constraints on the Standard Model", arXiv:0712.0929

[20] I. I. Y. Bigi, Y. L. Dokshitzer, V. A. Khoze, J. H. Kühn and P. M. Zerwas, *Phys. Lett. B* **181** 157 (1986).

[21] D. Chakraborty, J. Konigsberg and D. L. Rainwater, *Ann. Rev. Nucl. Part. Sci.* **53** 301 (2003).

[22] J. H. Kuhn, Nucl. Phys. B 237 (1984) 77.

[23] J. C. Collins, D. E. Soper, and G. Sterman, Factorization of Hard Processes in QCD, Adv. Ser. Direct. High Energy Phys. 5 (1988) 1âĂŞ91, [hep-ph/0409313].

[24] S. Bethke, *Experimental Tests of Asymptotic Freedom*, arXiv:hep-ex/0606035

[25] V.N. Gribov and L.N. Lipatov, Sov. J. Nucl. Phys. 15 (1972) 438, 675; G. Altarelli and G. Parisi, Nucl. Phys. B126 (1977) 298; Yu.L. Dokshitzer, Sov. Phys. JETP 46 (1977) 641.

[26] V. S. Fadin, E. A. Kuraev, and L. N. Lipatov, Phys. Lett. B 60, 50 (1975);

E. A. Kuraev, L. N. Lipatov and V. S. Fadin, Sov. Phys. JETP 44, 443 (1976) [Zh. Eksp. Teor. Fiz. 71, 840 (1976)];

E. A. Kuraev, L. N. Lipatov and V. S. Fadin, Sov. Phys. JETP 45, 199 (1977) [Zh. Eksp. Teor. Fiz. 72, 377 (1977)];

I. I. Balitsky and L. N. Lipatov, Sov. J. Nucl. Phys. 28, 822 (1978) [Yad. Fiz. 28, 1597 (1978)].

[27] A.D. Martin , W.J. Stirling , R.S. Thorne and G. Watt *Parton distributions for the LHC* [hep-ph/0901.0002v1]

[28] J. Pumplin, A. Belyaev, J. Huston, D. Stump and W. K. Tung, JHEP 0602, 032 (2006) [arXiv:hep-ph/0512167].

[29] I. Y. Pomeranchuk, *Sov Phys. JETP* **7**, 499 (1958).

[30] A. Lister, "Top Quark Pair Production Cross Section and Forward-Backward Asymmetry at the Tevatron", hep-ex 0810.3350v2

[31] S. Moch, P. Uwer, arXiv:0804.1476v2 [hep-ph]

[32] W. M. Yao et al. [Particle Data Group], J. Phys. G 33 (2006) 1.

[33] M. Jezabek and J. H. Kuhn, Nucl. Phys. B 314 (1989) 1.

[34] A. Denner and T. Sack, Nucl. Phys. B 358 (1991) 46.

[35] G. Eilam, R. R.Mendel, R.Migneron and A. Soni, Phys. Rev. Lett. 66 (1991) 3105.

[36] M. Jezabek and J. H. Kuhn, Phys. Rev. D 48 (1993) 1910 [Erratum-ibid. D 49 (1994) 4970]

[37] A. Czarnecki and K. Melnikov, Nucl. Phys. B 544 (1999) 520

[38] K. G. Chetyrkin, R. Harlander, T. Seidensticker and M. Steinhauser, Phys. Rev. D 60 (1999)

[39] A. Quadt, Eur. Phys. J. C 48 (2006) 88.

[40] The ATLAS Collaboration, JHEP 6 (2012), 88.

[41] S. Frixione, B.R. Webber, *Matching NLO QCD computation and parton shower simulations*, JHEP **06** (2002) 029 [hep-ph/0204244]

[42] G. Corcella et al., *HERWIG 6: an event generator for hadron emission with interfering gluons (including supersymmetric processes)*, JHEP 01 (2001) 010 [hep-ph/0011363]

[43] N. Kidonakis and R. Vogt, arXiv:0805.3844 [hep-ph].

[44] G. Agostinelli et al. *Geant4 - a simulation toolkit*. Nuclear Instruments and Methods in Physics Research, A(506): 250-303, 2003.

[45] The ATLAS Collaboration, *The ATLAS Simulation Infrastructure*. Eur. Phys. J. C 70 823.874.

[46] *Twiki page: Atlas production Group*, Online https://twiki.cern.ch/twiki/bin/viewauth/AtlasProtected/A

[47] The ATLAS Collaboration, *New ATLAS event generator tunes to 2010 data*, ATLAS-PHYS-PUB-2011-008, 2011.

[48] M. L. Mangano, M. Moretti, F. Piccinini and M. Treccani, JHEP 0701 (2007).

[49] The ATLAS Collaboration, *Heavy Flavor Overlap Removal*, ATL-COM-PHYS-2010-695, 2010.

[50] H. Lai, *New parton distributions for collider physics*, Phys. Rew. D 82 (2010)

[51] E. Turlay, ATL-PHYS-PROC-2009-018

[52] ATL-COM-PHYS-2011-1636

[53] B. A. et al., *Object selection and calibration, background estimations and MC samples for the Autumn 2012 Top Quark analyses with 2011 data*, ATL-COM-PHYS-2012-1197

[54] B. Acharya et al. *Object selection and calibration, background estimations and mc samples for the winter 2012 top quark analyses with 2011 data* ATL-COM-PHYS-2012-224.

[55] Atlas Muon Combined Performance, *Guidelines of 2011 data in release 17*, Online: https://twiki.cern.ch/twiki/bin/viewauth/AtlasProtected/MCPAnalysisGuidelinesRel17MC11a

[56] G. P. Salam and G. Soyez, JHEP05(2007) 086.

[57] S. D. Ellis and D. E. Soper. *Successive combination jet algorithm for hadron collisions*. Phys. Rev., D48:3160-3166, 1993.

[58] Y. L. Dokshitzer, G. D. Leder, S. Moretti and B. R. Webber, JHEP 9708, 001 (1997) [hep-ph/9707323].

[59] M. Cacciari, G. P. Salam, G. Soyez, JHEP 0804:063, 2008.

[60] C. Sandoval, J. Backus Mayes, P. Manning and G. Zevi della Porta. Jets with pileup in 2011 twiki page. ATLAS Twiki.

[61] The ATLAS collaboration, ATLAS-CONF-2011-102

[62] ATLAS Collaboration, *Jets and Missing Transverse Energy*, Expected Performance of the ATLAS Experiment ("CSC Book"), 2008, pp.261

[63] A. Bangert, *Measurement of the Top Quark Pair Production Cross Section*, November 2008 talk at University of California at Santa Cruz.

[64] L. Fiorini and J. Nadal, IFAE meetinng, 29 June 2009

[65] I. Borjanovic et al, Eur. Phys. J C39S2 (2005) 63-90.

[66] M.L. Mangano, M. Moretti, F. Piccinini, R. Pittau, A. Polosa, *ALPGEN, a generator for hard multiparton processes in hadronic collisions*, JHEP 0307:001,2003, hep-ph/0206293.

[67] The ATLAS coll., top working group note, 3 June 2009

[68] M. Bachtis, *Muon performance of the ATLAS detector using t-quark decays*, XXV Workshop on Recent Developments in High Energy Physics & Cosmology, 2007.

[69] M. Awramik, M. Czakon, A. Freitas, and G. Weiglein, "Precise prediction for the W-boson mass in the standard model", *Phys. Rew. D* **69** (2004)

[70] [The LEP working group for Higgs boson searches], Phys. Lett. B **565** (2003) 61 [arXiv:hep-ex/0306033].

[71] LEP Electroweak Working Group, `http://lepewwg.web.cern.ch/LEPEWWG/`; Tevatron Electroweak Working group, `http://tevewwg.fnal.gov/`.

[72] Tevatron New Phenomena and Higgs Working Group, combining CDF and D0 upper limits, `http://tevnphwg.fnal.gov/results/SM_Higgs_Summer_08/`.

[73] H. Flaecher, M. Goebel, J. Haller, A. Hoecker, K. Moenig and J. Stelzer, arXiv:0811.0009 [hep-ph].

[74] A. Hocker and V. Kartvelishvili, *SVD Approach to Data Unfolding*, hep-ph/9509307v2

[75] M. Cacciari, M. Czakon, M. Mangano, A. Mitov, P. Nason, *Top-pair production at hadron colliders with next-to-next-to-leading logarithmic soft-gluon resummation*, hep-ph 1111.5869, Mar 2012